# SINGLE PARTICLE TRACKING OF PLASMA MEMBRANE PROTEINS

**by**

**Elin Edwald**

A dissertation submitted in partial fulfillment
of the requirements for the degree of
Doctor of Philosophy
(Chemical Biology)
in the University of Michigan
2014

Doctoral Committee:

Assistant Professor Sarah L. Veatch, Chair
Professor Charles L. Brooks III
Professor Henry I. Mosberg
Associate Professor Roger K. Sunahara
Professor John J. G. Tesmer

fyrir afa og skúla

**Acknowledgements**

First of all, I would like to acknowledge my advisor. She took on the challenge of having me in her lab half way through the Ph.D. and exercised great patience as I navigated the learning curve associated with coding in Matlab and other firsts. It is a great honor to be the first to graduate from her lab. She has been a strong role model as a scientist and person. I hope to someday be in a position to emulate her solution-focus and the way she informs her mentorship with her experience. Thank you, Sarah.

Secondly, I would like to thank my lab members who have maintained a friendly and constructive environment to work in. Many of them have also contributed directly to this project. Jing Wu did bleb experiments presented here and some of the cloning. Matt Stone contributed cloning work and has coded software used by the lab, which provided a valuable comparison to the results presented in this work. Brian DeVree has been a priceless officemate and provided valuable discussion and editing. Krish Raghunathan has been generous with his opinions also, and helped with editing. Other members of the lab such as Erin Gray, Elly Gray, Jason Karslake, Josh Karslake, Eric Sink, and Jiang Zhao have contributed to the enthusiastic and hard-working atmosphere in the lab, as well as executing projects in the lab that have been complementary to the this work. Thank you.

Third, I would like to thank collaborators outside the lab who have directly contributed to the project. Most notably, Akira Ono and his student Jonathan Grover, who provided many of the protein constructs presented in this work. Thank you.

Fourth, I would like to thank collaborators who have supported various projects I have undertaken during my time at University of Michigan, which unfortunately have not been accounted for in this document. In particular, I'd like to thank Arun Anantharam and Ron Holz for their support and help testing for curvature-induction of activated GPCRs in cellular footprints. Also, thanks to Benita Sjögren for her participation in testing for functional consequences of lipid perturbations on GPCRs. Henry Mosberg and members of his lab: Jessica Anand for her fluorescently labeled ligands and stably transfected cells, as well as Irina Pogozheva and Andrei Lomize who generously offered to do calculations. Joe Schauerte generously helped execute FCS experiments. Joe, Kathleen Wisser, Ari Gafni, and Duncan Steel also provided invaluable support during this process. Thank you.

I would like to thank my thesis committee for their input through the years and for keeping me on through relatively frequent meetings, project changes, and a lab change. Particularly, I would like to the thank Roger Sunahara for his continued mentorship and for planting the seeds of many interesting questions in GPCR research. I also owe thanks to the puppeteer John Tesmer, who has been a friend and invaluable source of advice at key points throughout my time at Michigan.

Thank you also to the program for providing me the opportunity to try my hand at science in an interdisciplinary program. Thank you to director Anna Mapp for her support, especially during the lab switch.

I am the product of a great number of people who have taken the time to teach me and offer me the opportunity to do research in their labs. Among them: Rostam Afshinnekoo, Sveinn Guðmundsson, Kristbjörn Orri Guðmundsson, Guðmundur Hrafn Guðmundsson, Jón Ólafsson, Magnús Már Kristjánsson, Shigeru Hisajima, Toshiyuki Tanaka, and Yoko Nagumo. Thank you.

Last but not least I would like to thank my family for their support. Thanks especially to Robb who is unquestionably my better half, and without whom I would have missed half my time at Michigan.

## Table of Contents


**Dedication** ii

**Acknowledgements** iii

**List of Figures** ix

**List of Tables** xi

**List of Abbreviations** xii

**Abstract** xiv

**Chapter 1 Introduction** 1

Overview 1
The function of transmembrane proteins is dependent on membrane 2
Palmitoylation is vital for protein function 4
Membrane heterogeneity 9
Experimental tools to measure diffusion of proteins in cell membranes 21
Scope and hypotheses of the work 30
Works Cited 32

**Chapter 2 Materials and Methods** 42

Reagents and key equipment 42
Selection and design of membrane probes 44
Cell Culture 46
Transfection 47
Generation of GPMVs 47
Imaging Buffer 49

Temperature regulation and temperature experiments 50
Imaging of mEos constructs 51
Particle localization 53
Particle Tracking 56
Analysis of diffusion constants using Brownian simulations 60
Bootstrapping 62
Models for Diffusion vs. radius 63
Estimating anchor size 64
Works Cited 65

**Chapter 3 Diffusion of minimal protein anchors in the membranes of live cells 68**

Introduction 68
Results and Discussion 70
Conclusion 99
Works Cited 101

**Chapter 4 Hypoxic buffer conditions result in fast and homogenous diffusion 107**

Introduction 107
Results and Discussion 112
Conclusions 134
Work Cited 137

**Chapter 5 The effect of palmitoylation on lateral diffusion 141**

Introduction 141
Results and Discussion 144
Conclusion 157
Works Cited 158

**Chapter 6 Future directions and conclusions 161**

Summary of conclusions 161
Strengths of SPT 163
Future directions in investigating phase behavior in cells 167
Future directions for SPT 169
Future directions in hypoxia 170
Summary of significance 172
Works Cited 173

## List of Figures

Figure 1-1 Schematic of contemporary descriptions of membrane heterogeneity. 15
Figure 1-2 Hypothesized schematic of the phase diagram of plasma membrane. 19
Figure 2-1. Choosing a maximum step cutoff. 59
Figure 3-1 Characterizing diffusion of model membrane proteins in live cells. 72
Figure 3-2 Cells remain viable after 30min incubation in hypoxic imaging buffer. 74
Figure 3-3 Effect of glutathione and oxygen scavenging on diffusion coefficients and heterogeneity. 75
Figure 3-4 Simulations of Brownian diffusers identify diffusion heterogeneity. 78
Figure 3-5 Diffusion coefficients obtained from cumulative distribution functions of B-TM mEos 3.2 and A-TM mEos 3.2. 82
Figure 3-6 Diffusion of mobile population is unconfined. 83
Figure 3-7 Rate of diffusion of mEos 3.2 proteins decreases with increasing anchor size. 84
Figure 3-8 Diffusion constant of immobile fraction is accounted for by localization error. 86
Figure 3-9 Some immobile particles are glass deposited. 88
Figure 3-10 – Deleting the dileucine motif has no effect on lateral diffusion. 89
Figure 3-11 Protein diffusion is slowed with mEos2. 93
Figure 3-12 (A) $D_{SM}$ histograms from a single cell expressing B-TM mEos 3.2 recorded at four temperatures. 97
Figure 4-1 Phototoxicity manifested as blebbing. 114
Figure 4-2 Representative long trajectories of transmembrane proteins B-TM, A-TM, and $\beta_2$AR in HEPES - buffered imaging solution and hypoxic imaging buffer. 116
Figure 4-3 Histograms of single molecule ‘diffusion’ constants of localized particles inside and outside the footprint of a single cell expressing GG mEos3.2. 118

Figure 4-4 Single molecule diffusion coefficients from cells expressing B-TM. 119
Figure 4-5 Diffusion is slower and heterogeneous under hypoxic conditions. 121
Figure 4-6 Diffusion values of the faster of the two mobile populations versus estimated size of embedded membrane anchor lateral diffusion in HEPES buffer. 125
Figure 4-7 Single trajectory α histogram for B-TM in hypoxic or HEPES-buffered imaging solution. 126
Figure 4-8 The lateral diffusion of fusion proteins is confined for all constructs tested under normoxic conditions. 129
Figure 4-9 Apparent activation energy is lower for lateral diffusion of B-TM in normoxic buffer than either GPMVs or hypoxic conditions. 132
Figure 4-10 Transition temperature of giant plasma membrane vesicles extracted from HeLa cells change after exposing the cells to hypoxic imaging buffer for 30 minutes. 133
Figure 5-1 Point mutation of palmitoylation sites results in minimal change in lateral diffusion. 146
Figure 5-2 Point mutation of palmitoylation sites results in increased confinement of $\beta_2$AR. 147
Figure 5-3 - Point mutation of palmitoylation sites results in minimal change in lateral diffusion for B-TM. 149
Figure 5-4 Lateral diffusion of B-TM and B-TMpalm responds differently to temperature decrease. 152
Figure 5-5 Diffusion of $\beta_2$AR in the membranes of HeLa and CHO cells suggest that membrane properties might be quite different. 155
Figure 6-1 Schematic of contemporary descriptions of membrane heterogeneity reprinted from introduction. 164

## List of Tables

Table 2-1 List of reagents, key equipment and their sources. ..... 43
Table 2-2 – Amino acid sequences of model membrane protein constructs. ..... 45
Table 3-1 - Single molecule diffusion coefficients $D_{SM}$ ($\mu m^2$/sec) for the individual tracks shown in Figure 3-1 B..... 76
Table 3-2 Mean α values from experiment and simulated Brownian data..... 92
Table 4-1 Diffusion values comparing overall diffusion constants from hypoxic conditions determined for Chapter 3, and the diffusion constants of the fast and slow populations detected in HEPES buffer. ..... 122
Table 4-2 Population α values of lateral diffusion under hypoxic and HEPES-buffered conditions. ..... 130
Table 4-3 Fraction of trajectories that belong to less confined α peak ..... 131

## List of Abbreviations

*(F)PALM. - Fluorescent Photoactivated Localization Microscopy*

*A-TM. - Linker of Activated T-Cell single helix, palmitate null mutant*

*ATP. - adenosine triphosphate*

*BSA. - bovine serine albumin*

*B-TM. - truncated hemagglutinin protein, dimeric helix, palmitate null mutant*

*DMEM. - Dulbecco's modified essential media*

$D_{MP}$*. - mobile population diffusion*

$D_{SM}$*. - single molecule diffusion*

$E_a$*. - activation energy*

*FA. - free area model*

*FCS. - fluorescence correlation spectroscopy, - fluorescence correlation spectroscopy*

*FRAP. - fluorescence recovery after photobleaching*

*GG. - geranylgeranyl anchor*

*GPCR. - G protein-coupled receptor*

*GPI. - glycophosphatidylinositol anchor*

*GPMVs. - giant plasma membrane vesicles*

*GRK. - G protein-coupled receptor kinase*

*HEPES. - 4-(2-hydroxyethyl)-1-piperazineethanesulfonic acid*

$k_BT$*. - energy At room temperature 25 °C equivalent to 2.479 kJ·mol*$^{-1}$

$L_d$*. - liquid disordered phase*

*LED. - light emitting diode*

$L_o$*. - liquid ordered phase*

*mEos2. - oligomerizing photoconvertible fluorescent protein*

*mEos3.2. - monomeric photoactivatable fluorescent protein*

*MSD. - mean squared displacement*

*PBS. - phosphate buffered saline*

*PM. - palmitoyl-myristoyl anchor*

*RPMI. - Roswell park memorial institute, a medium*

*RTK. - Receptor Tyrosine Kinases*

*SD. - Saffman Delbrück equation*

*SPT. - Single Particle Tracking*

*SPT-PALM. - Single Particle Tracking – Photoactivated Localization Microscopy*

*STED-FCS. - stimulated emission depletion-fluorescence correlation spectroscopy*

*STORM. - stochastic optical reconstruction microscopy*

*TIRF. - total internal reflection fluorescence*

$\alpha$. *- exponent of anomalous diffusion*

$\alpha_{SM}$. *- single molecule exponent of anomalous diffusion*

$\beta_2$*AR. - beta two adrenergic recptor, a GPCR*

$\lambda$. *- hydrodynamic length*

**Abstract**

Palmitoylation is important to the function and trafficking of many proteins. As the only reversible posttranslational lipid modification, it is thought to facilitate signaling by dynamically targeting proteins to the necessary membrane fractions. This has been shown for membrane-associated proteins, but the role of palmitoylation for transmembrane proteins is less clear. It has been proposed that palmitoylation targets transmembrane proteins to membrane subdomains often termed 'lipid rafts'. In this work, we test the hypothesis that palmitoylation affects the diffusion dynamics of transmembrane proteins and propose that this could be a means to modulate protein function. Using single fluorescent particle tracking, this work quantifies diffusion and confinement parameters of a large panel of fluorescent fusion membrane proteins ranging in size, mode of membrane anchoring, and putative phase-association. These include palmitoylated and non-palmitoylated versions of three transmembrane proteins (truncated linker of activated T-cell, truncated hemagglutinin, and $\beta_2$ adrenergic receptor) as well as three proteins anchored with lipid moieties (glycophosphatidylinositol (GPI), palmitoyl and myristoyl, or geranylgeranyl). We present a method of analysis that uses Brownian simulations to aid in identifying heterogeneity. Among our findings is that lateral diffusion in a photoprotective hypoxic imaging buffer is Brownian and vastly simplified in comparison to non-hypoxic imaging buffer, suggesting possible cytoskeletal remodeling under hypoxic conditions. In both hypoxic or normoxic imaging conditions, lateral diffusion is strongly size-dependent for smaller probes, consistent with findings in model membranes. Thus our results indicate that diffusion of small probes is particularly sensitive to dimerization when it occurs in either a biological context or due to labeling techniques. Differences in lateral diffusion were not significant at 37°C when comparing otherwise identical transmembrane proteins with and without palmitoylation sites, though the proteins differentiate themselves at lower temperatures. This suggests that

palmitoylation does not modulate transmembrane protein function by altering lateral diffusion under physiological conditions.

# Chapter 1

# Introduction

## Overview

Posttranslational modifications are covalent chemical modifications to proteins. Functional moieties added to proteins include methyl group, acetyl group, sugar chains, ubiquitin, phosphate, nitric oxide, and lipids (Wang et al., 2013). These chemical moieties endow the proteins with additional functionalities. In the case of lipids, they modulate how proteins interact with the membrane. Soluble proteins can be anchored to the membrane using one or multiple lipid modifications including geranylgeranylation, farnesylation, myristyolation, palmitoylation and the glycolipid modification glycophosphatidylinositol (Jiang et al., 1995; Resh, 1999). Once lipidated, the proteins remain modified until proteolysis or degradation. The exception is palmitoylation, which is a reversible and enzymatically regulated modification that occurs on over a hundred proteins. This work quantifies the effect of palmitoylation on the lateral diffusion of transmembrane proteins.

Palmitoylation is demonstrated to be vital to normal function of transmembrane proteins (Baekkeskov and Kanaani, 2009; Charollais and Van Der Goot, 2009; Resh,

2006). Unlike soluble cytosolic proteins, transmembrane proteins do not require lipid modification for association to the membrane. Nonetheless, inhibiting palmitoylation can impair signaling. In this work we test the hypothesis that palmitoylation affects the diffusion dynamics of transmembrane proteins and propose that this could be a means to modulate protein function. It is my goal in this thesis to present the development of methodology to record and analyze lateral diffusion of membrane proteins in live cells and application of that methodology to measuring the lateral diffusion of palmitoylated and non-palmitoylated variants of three transmembrane proteins. In the process I have also characterized the effect of hypoxic and normoxic buffer conditions on lateral diffusion of multiple membrane proteins, determined that small probes have a strong size-dependence of lateral diffusion, and calculated apparent activation energies of lateral diffusion using our approach under the different conditions.

## The function of transmembrane proteins is dependent on membrane

Long before understanding of the exact nature of the plasma membrane, it was clear that cells respond to specific chemicals. For example, application of nicotine to denervated muscle causes contractions (Langley, 1905) as does adrenaline on heart tissue (Lodish et al., 2000). When the lipid bilayer structure of plasma membranes was first understood, it was thought that chemicals acted directly on the lipids. The subsequent discovery of various membrane proteins has shifted understanding of cell signaling decidedly to a protein-centric view. For example, the effect of adrenaline on heart muscle is mediated by the β adrenergic receptors of the G protein-coupled receptor (GPCR) family (Lodish et al., 2000). GPCRs are a large family of seven transmembrane receptors

that recognize a large number of diverse signals. Their extracellular face responds to light, hormones, and drugs, while their intracellular face interacts with G proteins, G Protein-Coupled Receptor Kinases (GRKs), β-arrestins, and other intracellular signaling partners that act on the transmitted signal.

However, GPCRs and the myriad other membrane proteins do not work alone and depend on the plasma membrane to function. To study GPCR function in isolation, the proteins must first be extracted from the membrane using harsh detergents that solubilize their lipid environment. Subsequently, their stability and activity suffers, and their function is only restored when reconstituted in a lipid bilayer (Strulovici et al., 1984; Calinski et al., 2011; Whorton et al., 2007; Kuszak et al., 2009; Whorton et al., 2008). Furthermore, the membrane imposes on its membrane-anchored proteins a particular orientation, two-dimensional diffusion (Saffman and Delbrück, 1975; Axelrod, 1983) and reaction kinetics (Emeis and Fehder, 1970) which have shaped the way their function has evolved. Finally, membrane proteins respond to specific lipids (Suh and Hille, 2005) and exhibit full activity only in particular lipid compositions (Gaibelet et al., 2008; Kuszak et al., 2009). GPCRs for example are often particularly sensitive to cholesterol and stabilizing them for crystallization requires cholesterol in the crystallizing conditions (Cherezov et al., 2007; Rasmussen et al., 2011; Jaakola et al., 2008; Caffrey, 2009). Crystallographic evidence suggests that cholesterol has specific binding sites in the transmembrane domain of $\beta_2$AR (Hanson et al., 2008). Furthermore, cholesterol is required for high-affinity ligand binding by the μ-opioid receptor (Gaibelet et al., 2008) and both chronic and acute inhibition of adenylyl cyclase are attenuated by cholesterol depletion (Levitt et al., 2009). The sensitivity of opioid signaling to cholesterol has also

been interpreted as an effect of microviscosity rather than specific binding or phase behavior (Lazar and Medzihradsky, 1992, 1993; Levitt, 2010). Therefore, membrane proteins are perhaps better described as protein-lipid collectives (Lingwood and Simons, 2010). These are compelling reasons to study how membrane proteins interact with their native membrane environment, and to determine how lipids and proteins work together to facilitate membrane function.

## Palmitoylation is vital for protein function

Palmitoylation is a posttranslational modification that modulates how proteins interact with its membrane environment (Baekkeskov and Kanaani, 2009; Milligan et al., 1995; Smotrys and Linder, 2004). For example, palmitoylation affects the function of nearly every aspect of signaling through GPCRs, including G proteins, regulators of G protein signaling (RGS) and many of the receptors themselves. This makes GPCR signaling an interesting target to appreciate the role of palmitate in modulating the relationship between membrane and proteins.

Palmitoylation is required for correct trafficking, membrane association, and function of proteins (Charollais and Van Der Goot, 2009; Resh, 2006) though how palmitoylation does this is not always clear. Soluble proteins such as the small GTPases H-Ras and N-Ras can cycle off and on membranes until they are palmitoylated, at which point they become plasma membrane bound (Baekkeskov and Kanaani, 2009). Depalmitoylation reverses their plasma membrane association and the proteins are trafficked elsewhere. In this case, the role of palmitoylation is fairly clear and deletion of the requisite cysteine residues results in dysfunction of the Ras proteins correlated with mislocalization. This type of trafficking is an order of magnitude faster than vesicular

transport (Baekkeskov and Kanaani, 2009) and may be important to facilitating the time-scale of signaling. Many transmembrane proteins are also palmitoylated (Charollais and Van Der Goot, 2009; Chini and Parenti, 2009). It is less clear what the role of palmitoylation is in integral membrane proteins, as these do not require palmitoylation to remain stably associated with the membrane, nor do they engage in vesicle-independent trafficking. However, in transmembrane proteins also, palmitoylation is important to proper signaling (Charollais and Van Der Goot, 2009; Chini and Parenti, 2009). As a dynamically regulated posttranslational modification, palmitoylation has the potential to modify protein function on a time-scale that is relevant to signaling. Indeed the palmitoylation state of proteins has been shown to change in response to stimulus (Chini and Parenti, 2009; Loisel et al., 1999; Mouillac et al., 1992).

Multiple roles for palmitoyl modification have been proposed that could account for their importance to function of transmembrane proteins. First palmitate, in conjunction with cholesterol, has been proposed to stabilize GPCR dimers (Zheng et al., 2012), which in turn is thought to change receptor signaling. Furthermore, palmitoylation may alter interaction with signaling partners (Charollais and Van Der Goot, 2009). Finally, palmitoylation is proposed to induce association with plasma membrane subdomains persistently known as “lipid rafts” (Charollais and Van Der Goot, 2009; Levental et al., 2010a; Milligan et al., 1995) ‘Rafts’ are thought to organize membrane components (Lingwood and Simons, 2010). This last proposal is based on the observation that palmitoylation confers detergent resistance on transmembrane proteins in a classic assay of ‘lipid rafts’ and palmitoylated proteins associate with the ‘raft’ phase of plasma membrane vesicles (Delint-Ramirez et al., 2011; Levental et al., 2010a; Melkonian et al.,

1999). Further descriptions about the nature of this putative membrane organization are found below.

If palmitoylation stabilizes transmembrane protein dimers, lateral diffusion should slow. However, the extent of slowing may depend on the size of the protein. In the context of two-dimensional lateral diffusion in lipid bilayers, the size-dependence of diffusion will be dominated by the size of the membrane-embedded anchor rather than the size of the extramembranous portion, because of the higher viscosity of the lipid bilayer (Clausen and Lagerholm, 2011). Studies in model membranes indicate that in the relationship between size and rates of diffusion, two regimes exist for objects the size of proteins. On a scale corresponding to lipid species (up to 0.8-1$nm^2$), rates of diffusion exhibit a strong dependence on the size of diffuser in model membranes (Vaz et al., 1982; Almeida et al., 1992; Lee et al., 2003; Liu et al., 1997). This regime, described by the free area model of diffusion, is governed by the probability of void areas opening up for the diffusing entity to move into. In a larger size regime, corresponding to multiple-transmembrane-domain proteins, the governing limitation becomes viscous drag. Diffusion of such species can be described by a continuous hydrodynamic model of the membrane first proposed by Saffman and Delbrück (Saffman and Delbrück, 1975) who predicted a weak dependence on the size of diffusers proportional to ln(1/Radius). Therefore, if palmitoylation tends to cause dimerization, small proteins will be slowed more than larger proteins. In this study protein anchors of different sizes are investigated to span the different size scales relevant to membrane proteins. Therefore, we encounter the following questions in this study. Do findings about high size dependence of small diffusers in model membrane proteins hold in intact plasma membranes? Regardless, are

the differences in rates of lateral diffusion between monomers and dimers sufficient to detect by lateral diffusion methods?

One corollary to the size dependence of diffusion is that even in the absence of dimerization, palmitoylation may slow down lateral diffusion due to increased effective size. The size of the protein and degree of palmitoylation would be expected to determine the extent of this effect where a mono-palmitoylated seven transmembrane domain protein would be minimally affected by the presence of palmitate, whereas a tri-palmitoylated single transmembrane protein will be more affected. Again, this study measures the diffusion of proteins of different sizes and degree of palmitoylation.

Palmitate-induced changes in interaction with signaling partners (Charollais and Van Der Goot, 2009) also potentially changes or even arrests lateral diffusion, though this is protein specific. This includes positive regulation of protein interaction such as with mannose-6-binding protein and its interaction with retromer for trafficking (McCormick et al., 2008). Negative regulation also occurs such as with the impaired interaction of palmitoylated AMPA receptor with cytoskeleton binding protein (Hayashi et al., 2005) or function of engineered Epidermal Growth Factor Receptor (EGFR) (Macdonald-Obermann and Pike, 2009). Again, because we are interested in whether palmitoylation causes a general effect on lateral diffusion, we investigate the effect on biologically inert minimal model proteins in addition to $\beta_2$AR, our GPCR representative.

Finally, the effect of palmitate on lateral diffusion could be mediated through altered interaction with lipid rafts, which is referred to as phase-mediated membrane heterogeneity in this work. This heterogeneity is composed of two liquid lipid phases termed liquid disordered ($L_d$) and liquid ordered phase ($L_o$). The latter corresponds to the

'raft' phase. A large body of literature has implicated membrane heterogeneity in a variety of functions including compartmentalization, and large rearrangement events in the membrane such as adhesion, immune signaling, endocytosis, surface delivery of proteins and virus budding. Several lines of evidence have supported the role of palmitoylation in targeting proteins to the $L_o$ phase (Levental et al., 2010a). However, the exact structure and physical basis of membrane heterogeneity in the resting cell is not understood. In 2006, the field consensus was that "Membrane rafts are small (10–200 nm), heterogeneous, highly dynamic, sterol- and sphingolipid-enriched domains that compartmentalize cellular processes. Small rafts can sometimes be stabilized to form larger platforms through protein-protein and protein-lipid interactions." Several more specific descriptions of membrane-heterogeneity have been proposed, as described below. Belonging to different phases, palmitoylated proteins are expected to have altered lateral diffusion profiles compared to their non-palmitoylated counterparts. However, the lack of consensus about the nature of membrane heterogeneity (as detailed below) makes it difficult to predict exactly how lateral diffusion ought to be affected.

As with other membrane proteins, lipid rafts are proposed to explain certain mysteries concerning the GPCRs. Compartmentalization (or organizing components through phase-association) has been proposed to influence the interaction of G proteins and GPCRs, helping to explain greater selectivity *in cellulo* than *in vitro* (Neubig, 1994). Furthermore, differential membrane domain associations are thought to explain signaling differences between related receptors like $\beta_2$AR and $\beta_1$AR (Xiang et al., 2002). Gα and many receptors including μ-opioid and $\beta_2$AR are palmitoylated, and have been shown to increase their turnover or palmitoylation upon activation, prompting

the hypothesis that these proteins are dynamically targetted to lipid domains depending on activation state (Loisel et al., 1999; Mouillac et al., 1992; Resh, 1999). For these reasons $\beta_2$AR was included in the study as a GPCR representative but is compared to non-biological model proteins to investigate the general qualities imparted by palmitate on lipid-modified proteins.

## Membrane heterogeneity

A proposed role of palmitoylation is targeting of proteins to the $L_o$ phase. However, the structure and exact nature of membrane heterogeneity is controversial, due to a lack of consensus in the literature. This literature is reviewed below and will contribute to how the experimental results will be interpreted in subsequent chapters. It is also important to clarify that in the context of experimental evidence for membrane heterogeneity, distinguishing between lipid-mediated and non-phase (protein-) mediated heterogeneity can be a challenge. There is no debate over whether heterogeneity exists *in cellulo*. Many examples of clustered or confined lipids and proteins, immobile particles of proteins, and heterogeneous diffusion (Edidin, 1993; Kusumi et al., 2011) are reported in the literature. The challenge is delineating the role of lipid phases in this heterogeneity. Below I describe some tools that have been used classically to specifically query the role of lipid and develop the 'lipid raft' concept, the newer approaches used, and the models that these studies have espoused.

### Classical techniques point to membrane heterogeneity

A discussion of model membrane organization necessarily goes back to the fluid mosaic model proposed by Singer and Nicolson (Singer and Nicolson, 1972). They

described the gross and generalizable structure of the plasma membrane saying "the mosaic appears to be a fluid or dynamic one, and for many purposes, is best thought of as a two dimensional oriented viscous solution" (Singer and Nicolson, 1972). Notably, they explicitly do not rule out the presence of small domains. This description holds largely true today, but with adjustments to account for observed phase-behavior in simple bilayers, the effect of cholesterol *in cellulo,* and the results of detergent solubilization on plasma membranes.

Biophysical studies of lipids first suggested phase heterogeneity. The plasma membrane is composed of hundreds of species of lipids belonging to three groups: glycerophospholipids, sphingomyelins and sterols (Munro, 2003). Glycerophospholipids themselves are sufficient to form lipid bilayers. Adding a saturated lipid such as the sphingomyelins results in a gel phase that is thought not to appear in cells (Munro, 2003). Adding sterols such as cholesterol to this mix suppresses the gel phase (Yeagle, 1985) and instead generates the potential to form two liquid phases: liquid ordered ($L_o$) and liquid disordered ($L_d$) (Edidin, 2003; Heimburg, 2007; Simons and Vaz, 2004). $L_o$ is enriched in sphingolipids and cholesterol (Lingwood and Simons, 2010). Under certain conditions, $L_o$ is thicker, more ordered, and tends to be less permeable to small ions and glucose than $L_d$ (Bretscher and Munro, 1993). This is the phase corresponding to 'lipid rafts' (Schroeder et al., 1994). Below a composition-dependent transition temperature, these lipids phase separate into two distinct and macroscopic phases. It was the phase transition upon cholesterol titration that first suggested that biological membranes, which are high in cholesterol (up to 50%), might also exhibit phase separation (Sankaram and Thompson, 1990).

Detergent solubilization of biological membranes further fueled the idea that membrane lipids were heterogeneously distributed (Yu et al., 1973). Cells are treated with non-ionic detergent at 4 °C and the resulting solution applied to a density gradient to separate the soluble and insoluble fractions. The insoluble fraction is enriched in cholesterol and sphingomyelin (Brown and London, 1997) and signaling proteins were found to be associated with one of the two phases (Kenworthy et al., 2004; Schroeder et al., 1994; Scolari et al., 2009). Classic experiments in which detergent solubilization of proteins changed upon activation are particularly compelling support for the role of phase-mediated organization in function, for example H-Ras (Prior et al., 2001). This assay has been informative, particularly for establishing common post-translational modifications of proteins that result in $L_o$ or $L_d$ association such as glycophosphatidylinositol (GPI)($L_o$), palmitoylation ($L_o$), and prenylation ($L_d$). However, a number of caveats shed doubt on whether detergent solubilization accurately reflects membrane structure *in cellulo*. First, detergent solubilization is performed at 4°C, where phase behavior is not the same as at 37°C, which is above the transition temperature of biological membranes (Veatch et al., 2008). Second, detergents intercalate into the membrane during solubilization, which also alters the transition temperature (Heerklotz, 2002). Third, during the destructive solubilization process, selective solubilization of the inner leaflet, rather than distinct lateral domains may occur (Munro, 2003). Sphingomyelin is located almost exclusively in the outer leaflet of the plasma membrane (Munro, 2003). Cells that have been treated with detergent and imaged microscopically, show gaping holes in their membranes that are distinctly larger than the putative size of lipid domains (Brown and London, 1997; Brown and Rose, 1992; Kenworthy et al.,

2004; Patra et al., 1999; Suzuki et al., 2012; Yu et al., 1973). In recent years, the detergent resistant membrane assay has been largely abandoned in favor of more direct and subtle methods.

Cholesterol depletion is one of the canonical tests for 'lipid raft' involvement in biological processes, and is subtler than detergent extraction. Partitioning of proteins into detergent resistant fractions is found to change with cholesterol treatment (Kenworthy et al., 2004). By depleting cholesterol, the fraction of $L_o$ is reduced (Levental et al., 2009; Veatch et al., 2007). This method involves either inhibitors of cholesterol production, and/or cholesterol-depleted media, addition of cholesterol oxidase, or direct extraction of cholesterol from membranes with methyl-β-cyclodextran. (Edidin, 2003; Mueller et al., 2011; Simons and Vaz, 2004) Cells can be depleted of cholesterol temporarily without compromising viability, and normal function may be restored by replacing cholesterol once more (Munro, 2003; Levitt et al., 2009). However, fraction $L_o$ is not the only effect of cholesterol depletion. Permeability of the membrane increases (Bretscher and Munro, 1993), and if depleted too severely, drastic morphological changes take place, cytoskeleton integrity is compromised, and eventually the cell dies (Edidin, 2003). Furthermore, a handful of proteins have specific interactions with cholesterol including amyloid peptides, GPCRs, ion channels, and virus assembly proteins (Anderson and Jacobson, 2002; Cherezov et al., 2007). Therefore, cholesterol depletion is useful in identifying processes that are cholesterol dependent, but does not unequivocally show the dependence of those processes on phase-mediated heterogeneity.

**Evidence for functional consequences of membrane heterogeneity**

Some of the earliest evidence for proposed function of 'lipid rafts' came from Simons *et al*. in 1988 (Simons and Van Meer, 1988). They observed that the quantity but not types of lipids on the apical and basolateral sides of a polar intestinal epithelial cell were different and proposed that previously observed lipid domains might be involved in their lipid sorting mechanism (Simons and Van Meer, 1988).

Subsequently, evidence has accumulated suggesting a role of lipid domains in a variety of processes. T-cell signaling is one of the earlier examples of a lipid-assisted process (Simons and Gerl, 2010). One way to induce T-cell stimulation is the clustering of proteins that are GPI-anchored (Robinson, 1991; Simons and Gerl, 2010; Stefanova et al., 1991). These are associated with the raft phase, like many of the components involved in T-cell signaling, but do not transverse the membrane, suggesting that stimulation of intracellular signaling components may be lipid-domain facilitated (Simons and Gerl, 2010). Consistent with this, cholesterol depletion inhibited T-cell signaling (Simons and Gerl, 2010). Furthermore, caveola, through which clathrin-independent endocytosis is mediated, are caveolin- and cavin-stabilized 'flask-shaped invaginations in the membrane,' dependent on enrichment of sphingolipids and cholesterol for function (Parton and Simons, 2007).

'Rafts' are also involved in pathogenesis, such as in HIV virus budding (Waheed and Freed, 2009), which is cholesterol and sphingomyelin dependent. The coat protein gag becomes detergent-resistant during budding, and the virus envelope is enriched in raft-like components and depleted of non-raft host proteins. Internalization of bacterial toxins like Shiga toxin, or the simian virus 40 (SV40) is also though to occur by lipid-

facilitated processes (Simons and Gerl, 2010). They bind glycosphingolipids in the membrane. Shiga toxin forms non-ATP dependent tubules probably through a curvature-mediated and cholesterol-dependent process.

This subset of cellular processes where lipid phases have been shown to participate are characterized by large rearrangements and deformations to the lipid membrane. 'Rafts' appear to be important in facilitating such deformations (Honerkamp-Smith et al., 2009). How lipid phases manifest in the membranes of resting cells, however, is controversial, and many descriptions have been proposed (Klotzsch and Schutz, 2013).

**Descriptions of membrane heterogeneity**

Tremendous ambiguity exists in the literature over models or descriptions of membrane heterogeneity. For a time, caveola became synonymous with lipid rafts, which further confused the issue. Caveola, though enriched in sphingomyelin and cholesterol, are also protein-stabilized and long-lived structures, not the transient and elusive structures we associate with 'rafts' today (Pike, 2006). Kenworthy *et al.* described models of heterogeneity as falling under four possible categories: Immobile lipid domains, mobile lipid domains (in which proteins diffuse within domains and also with the diffusing domain), dynamic partitioning (of proteins into and out of a domain), or no rafts (Kenworthy et al., 2004). The first of these have been refuted (Kenworthy et al., 2004; Lommerse et al., 2006) but a mobile 'raft' structure is supported by others (Anderson and Jacobson, 2002; Pralle et al., 2000).

Several groups have observed data consistent with small-scale clusters of lipid-protein complexes ranging from two to a handful of raft probes (see Figure 1-1 A). For example 'raft'-anchored probes were found to show weak co-diffusion (Triffo et al., 2012). GPI-anchored proteins are observed in transient, cholesterol-dependent dimers (Suzuki et al., 2012) or groups of up to four proteins (Chaudhuri et al., 2011) that the authors suggest were directed to cluster by a dynamic actin network that is cholesterol dependent. Laser trap experiments have indicated stable long term (> 1 min) 'raft' structures on the scale of 26 nm (Pralle et al., 2000).

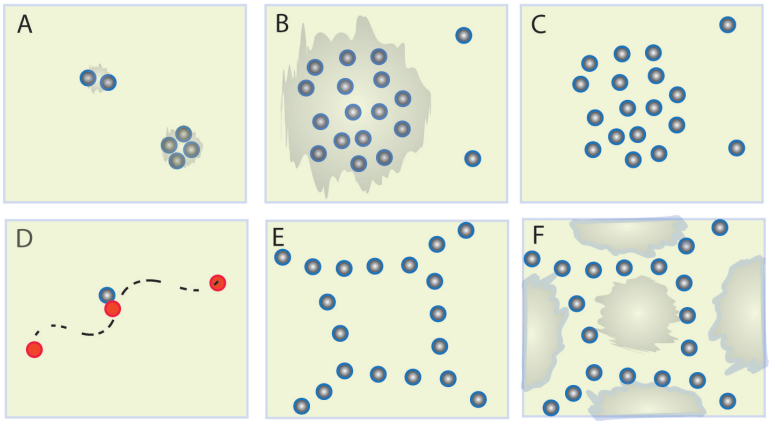


Figure 1-1 Schematic of contemporary descriptions of membrane heterogeneity. The circles are proteins, grey represents lipid phases (E.g. $L_o$), and green is the lipid bilayer. Not drawn to scale. (A) Stable or transient nanoclusters of 2-4 proteins whose associations are cholesterol dependent. (B) Protein cluster with an affinity for a lipid phase such as in co-patching studies or T-Cell and B-Cell signaling. This type of structure may vary greatly in size. (C) Clusters of proteins that allow hindered diffusion through them. Alternatively, dense but homogenously distributed immobile proteins can also cause anomalous subdiffusion. (D) Transient trapping in which specific and sometimes cholesterol dependent interactions with proteins occur. Eggeling et al. describe these as 10-20 ms in length and in regions less than 20 nm in size. (E) Associated with the Kusumi group, cytoskeletal corrals are obstacles that result in proposed 'hop-diffusion'. (F) 'Critical model' in which pinning proteins (blue) couple cortical actin to one of two liquid phases in the membrane, resulting in stabilized critical fluctuations possibly organized into entrained channels and puddles and mirroring the cytoskeleton. Depictions of outright phase separation, as observed in Meder et al. and hypothesized cytoskeletal aster structures from the Mayor group have been omitted from this schematic.

Observations from co-patching or cross-linking studies (Janes et al., 1999; Lingwood and Simons, 2010; Pike, 2006; Prior et al., 2003; Pyenta et al., 2003; Shelby et al., 2013) show that raft-like domains can be made to coalesce, suggesting the ability of

domains to engage in dynamic re-organization (see Figure 1-1 B). This model is distinguished from one where only protein is heterogeneously distributed in the membrane (E.g. Figure 1-1 C) because other 'raft probes' tend to co-localize and diffuse within these larger structures (Pinaud et al., 2009; Pyenta et al., 2003).

Eggeling *et al.* have developed new tools to push the size limit over which diffusion is observed. For example, stimulated emission depletion-fluorescence correlation spectroscopy (STED-FCS) uses a donut-shaped depletion signal to suppress the fluorescence emission of the labeled molecules, effectively reducing to sub-diffraction size a confocal spot to as small as 30 nm diameter (Eggeling et al., 2009). In their study, GPI-linked proteins and sphingo-linked lipids were found to diffuse with transient trapping for 10-20 ms, in areas smaller than 20 nm. Trapping was cholesterol-dependent. Their results indicate that transient trapping is due to interaction with cholesterol-protein complexes, but are inconsistent with stable lipid domains diffusing through the field of detection. Subsequent STED-FCS studies have examined the role of multiple lipid species in cells and confirmed cholesterol-dependent transient trapping of sphingolipid species. (Mueller et al., 2011). In the same vein, transient trapping of multiple fluorescent molecules were compared directly to the degree of phase preference in phase-separated giant plasma membrane vesicles (GPMVs) (Sezgin et al., 2012). These were not correlated across all compounds tested, suggesting that specific interactions rather than general effects of phase-association are sometimes responsible for transient trapping (see Figure 1-1 D).

**Cytoskeletal corrals**

The Kusumi group proposes a description of membrane organization that centers on the cytoskeleton (see Figure 1-1 E). With a combination of high intensity illumination, photostable particles, and fast imaging the Kusumi group uniquely observe lateral diffusion imaging phenomena over a range of time scales from 25 us to seconds (Kusumi et al., 2005). One of their central conclusions from the last two decades is that lateral diffusion is hindered by the presence of cytoskeletal 'corrals' that confine diffusing molecules. The characteristic diffusion pattern they describe is one of 'hop-diffusion,' whereby diffusion occurs in three time regimes. On a microsecond time scale diffusion is Brownian and as fast as in unhindered model membranes. At longer time scales diffusion is confined, as the molecule encounters cytoskeletal obstacles. At several millisecond time intervals the diffusion appears Brownian, but slower than the sub-corral diffusion. These two rates of apparent Brownian diffusion have been termed $D_{micro}$ and $D_{macro}$. While their frame rate is unrivaled, data consistent with $D_{micro}$ and $D_{macro}$ have been reported by other groups (Daumas et al., 2003; Meilhac et al., 2006).

This model is protein-centric in that it requires no involvement of lipids to explain the heterogeneous lateral diffusion of proteins. However, as new experiments challenged its simplicity, the description has been modified to encompass new observations into a more holistic view. For example, when the diffusion of exclusively extracellular leaflet (GPI-anchored) proteins were observed to undergo 'hop-diffusion' without the ability to interact with cytoskeleton, Kusumi therefore proposed the 'Picket-Fence' model. Even transient retention of transmembrane proteins at the cytoskeletal corrals are enough to cause diffusion obstacles on the outside of the bilayer, according to the authors. A recent

review from the Kusumi group, accommodates lipids by saying that the 'Picket Fences' exclude cholesterol due to poor packing and are likely to correlate with $L_d$ phase (Kusumi et al., 2011).

Overall, this view of the membrane is described as three tiers of spatial organization (Kusumi et al., 2011). The first is cytoskeletal corrals, whose size depends on cell type but range from 40-300 nm. The second tier is oligomerization or dimerization of proteins, which are sometimes lipid-dependent (Suzuki et al., 2012). These are 3-10 nm in size. The final tier, according to Kusumi, is lipid heterogeneity which is minimally three lipids and maximally the size of lipid shells. These are variable between studies and ill-defined but approximately 2-20 nm in size.

**A critical addition to cytoskeletal corrals**

An observation that GPMVs exhibit critical fluctuations (Veatch et al., 2008) has fueled the hypothesis that criticality may be the physical basis for phase-mediated membrane heterogeneity (Machta et al., 2011). A three-lipid mixture (unsaturated lipid, saturated lipid, and cholesterol) is sufficient to produce a critical membrane, but only in carefully chosen ratios and temperatures. Phase-diagrams have been precisely mapped for many synthetic membrane compositions (Honerkamp-Smith et al., 2008; Konyakhina et al., 2013; Veatch et al., 2007). Importantly, critical systems display universality. In other words, critical behavior is similar across all systems, and simulating critical behavior can be done with comparatively simple two dimensional lattice Ising simulations (Machta et al., 2011). Because biological membranes also exhibit critical fluctuations, they can be modeled in this way, producing quantifiable predictions of fluctuations despite the

complicated composition of biological membranes. A schematic of the 'critical' proposed model of biological membranes is depicted in Figure 1-2 and is reproduced with permission from Gray *et al*. (Gray et al., 2013)

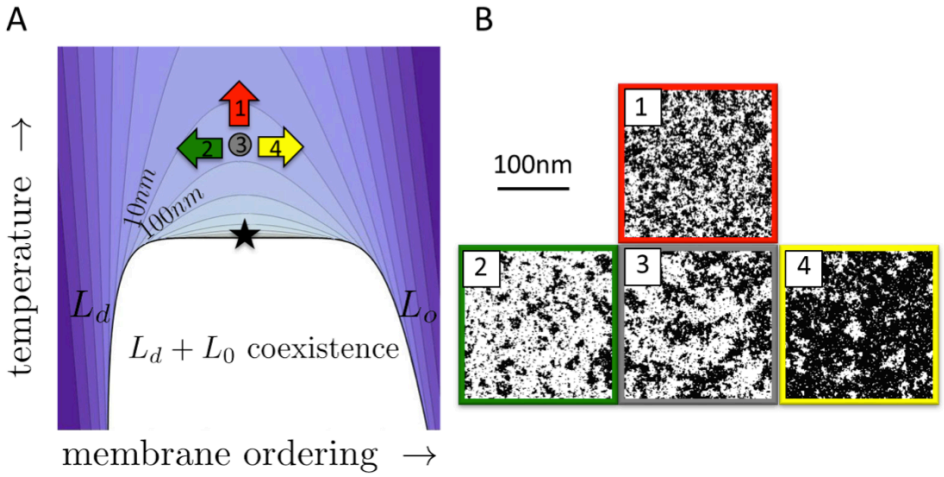


Figure 1-2 Hypothesized schematic of the phase diagram of plasma membrane. This figure is reprinted from Gray et al. (Gray et al., 2013) with permission from Elsevier. (A) A schematic of the phase diagram of the $L_o$ and $L_d$ phases in the cell. The grey dot (3) represents physiological conditions of roughly half $L_o$ and half $L_d$ at 37°C. The red arrow (1) represents the effect of anesthetics on critical compositions. They lower transition temperature, effectively increasing the distance from the critical point on the temperature axis. The green arrow (2) and yellow arrow (4) represent decrease and increase in cholesterol content respectively, and demonstrate the effect of cholesterol addition and depletion. (B) Snapshots from a two-dimensional Ising model simulation demonstrate the effect of each of the perturbations on the size of critical fluctuations and the fraction of $L_o$ black) and $L_d$ (white) at constant temperature. Whereas cholesterol manipulations change the fraction of $L_o$ and $L_d$, anesthetics affect the size of fluctuations but not this ratio.

Enthalpy and entropy of forming (or disassembling) extended domains are closely balanced around the critical point. This means that in the two-phase coexistence region closest to the critical point, thermal fluctuations on the order of $k_BT$ are sufficient to make domains elongated and their boundaries jagged in a dynamic manner. In the one phase region close to the critical point small inputs of energy are sufficient to coalesce domains into larger structures. Based on the sizes of critical domains in GPMVs, cells are predicted to reside 5% (in Kelvin) above the critical point, with fluctuations on the order of 20 nm. The critical model of membrane heterogeneity proposes that these fluctuations

are stabilized by sparse connections to cortical actin, making otherwise momentary structures stable over time. If the cytoskeletal meshwork forms connections to one phase, $L_d$ for example, this is predicted to form entrenched channels of $L_d$ along cytoskeleton with pools of $L_o$ in the 'corrals'.

The criticality model extends the corral description of lateral membrane organization in a few ways (see Figure 1-1 F). Importantly, it represents a very similar view of membrane structure, but incorporates the role of criticality in this organization. First, it provides an alternative physical basis for lipids to form cytoskeleton-stabilized lipid heterogeneity. Kusumi describes this organization in a way that is reminiscent of lipid shells (Anderson and Jacobson, 2002). This would require a large number of proteins to specifically associate with $L_d$ phase, in order to form the sort of lipid-protein-complex diffusion obstacles that Kusumi describes. The criticality model requires only a few points of such interactions in order to stabilize channels and domains in the membrane, and predicts that the size of such channels are strongly dependent on the proximity to criticality, but weakly to the number of cytoskeletal pinning sites. Second, the criticality model offers an explanation for the hundreds of lipid species meticulously maintained in a specific composition by the cell. It suggests that the diversity of lipids may be important to carefully maintaining the cell close to a critical point, due to the potential for several redundant critical points (Honerkamp-Smith et al., 2009). Finally, the criticality model provides a broad reason *why* lateral heterogeneity exists; namely, that large lipid rearrangements associated with biological events can occur with small input of energy. With the recent development of new and much needed tools to test the

role of criticality in membrane heterogeneity (Gray et al., 2013), this model is likely to be challenged or validated in the upcoming years.

## Experimental tools to measure diffusion of proteins in cell membranes

### Choosing single particle tracking to measure lateral diffusion

Lateral diffusion on the plasma membrane can be assessed in a variety of ways. The most established techniques for measuring diffusion of fluorescent particles are fluorescence correlation spectroscopy (FCS), fluorescence recovery after photobleaching (FRAP), and single particle tracking (SPT). FCS measures the correlation over time of fluorescent particles diffusing through a small area (e.g. 50-200 nm diameter areas) and reports on their average diffusion constant of diffusing particles. FRAP typically focuses on a larger area and measures the time it takes for the fluorescence of a photobleached area and reports the average diffusion constant as well as the fraction of recovery as a measure of particle mobility. SPT in contrast, tracks the diffusion of individual molecules and therefore can report on diffusion constants for individual diffusers. We chose SPT for our experiments because it is high-resolution and because it accounts well for populations of diffusers, as might be anticipated in a heterogeneous membrane environment. We chose to use mEos photoconvertible fluorescent proteins 3.2 and 2 as the label for our probes. Some relevant considerations of this method are described below and are briefly contrasted with the two related diffusion techniques.

Immobile particles are a common feature in lateral diffusion studies (Daumas et al., 2003; Kenworthy et al., 2004; Lommerse et al., 2006). By FRAP these appear as incomplete recovery and FCS does not account for them. SPT, on the other hand,

identifies immobile trajectories, as well as dynamic information about the duration of their immobility (given sufficiently long tracks), and their spatial distribution. FRAP and FCS can be difficult to interpret in the complex environment of the cell, when the data are often best fit by more than one diffusing populations (Clausen and Lagerholm, 2011). SPT can resolve multiple populations, particularly with the use of methodology introduced in the current study.

SPT is data intensive and requires careful analysis. First, each individual particle must be localized. For fluorescent particles, the emitted light's point spread function forms an Airy pattern, which can be approximated by a two-dimensional Gaussian function. After each particle in each frame of a recording is fit in this manner, connections are made between localizations in one frame and the preceding frame to form trajectories. This step varies in computational complexity depending on the tracking algorithm (Jaqaman et al., 2008; Saxton, 2009). Typically, the mean squared displacement from each trajectory is then determined individually, and all trajectories that are sufficiently long can be fit to determine diffusion parameters and further analyzed. In contrast, ensemble measurements like FCS and FRAP represent an entire sample in a single decay or recovery curve.

**Detecting membrane heterogeneity by SPT**

Membrane heterogeneity in our system is detected in one of two ways. The first is to examine more than one rate of diffusion suggesting a heterogeneous environment. The second is to measure the confinement of individual trajectories by extracting α the exponent of anomalous subdiffusion as described in Materials and Methods. Anomalous subdiffusion can result from a variety of obstacles and has been applied to the

investigation of phase behavior in cells. Model membrane systems enable characterization of the upper limit of the confinement potential of two-phase systems. The most distinct case is a gel-liquid composition, because diffusion in gel is orders of magnitude slower than in liquids, and can be approximated as impermeable to the diffuser (Skaug et al., 2011). Depending on the fraction of each phase, one phase will be the continuous phase and the other the discontinuous. At the percolation threshold neither phase is continuous (Heimburg, 2007). If the liquid phase is discontinuous, lateral diffusion is highly confined, whereas if the liquid is continuous the diffuser moves more freely through the bilayer. In either case anomalous diffusion can result in model membranes (Saxton, 1994; Skaug et al., 2011). If both phases are liquid, the same percolation concepts apply, but the contrast between the phases will be less drastic due to partial permeability of the diffuser even into the non-preferred phase.

Many potential models could be applied to lateral diffusion data to quantify anomalous subdiffusion (Metzler and Klafter, 2004). Many of these are complex, but for analysis on a single trajectory basis, over thousands of potential trajectories for a single cell, a simple model is required. Furthermore, some models employed in the field cannot be applied to short trajectories, such as those in the current study. (Lushnikov et al., 2012; Mascalchi et al., 2012; Sheets et al., 1995; Simson et al., 1995). A simple model, MSD = $4Dt^{\alpha}$, is a popular choice (Saxton, 2012; Skaug et al., 2011), and we find that it serves well as a simple and fast way to gauge confinement of individual trajectories. In this model, diffusion is Brownian when $\alpha = 1$, and values less than 1 indicate anomalous subdiffusion.

**Choosing fluorescent photoconvertible protein mEos as labels**

Choice of the appropriate label is an important experimental consideration for SPT. Particles are visualized by either fluorescence using organic fluorophores, fluorescent proteins, quantum dots, fluorescent beads, or by light scattering using functionalized gold particles. These labels can be attached to the membrane by conjugation to exogenous molecules (such as antibodies or toxins) with high affinity for endogenous membrane components. Alternatively, they can be attached by introducing fluorescent or biotinylated lipids to the membrane to which labeled streptavidin can then be attached. Tetracysteine, biotin ligase acceptor peptide (BLAP), acyl carrier protein (ACP), and SNAP tags are all genetically encoded modules that also enable labeling by organic fluorophores or conjugated dyes (Clausen and Lagerholm, 2011, 2013). Finally, fluorescent proteins can be expressed by the cell itself by transient or stable transfection and targeted to the plasma membrane by cellular machinery.

Each label has its strengths and weaknesses. First, their size can be prohibitive. Gold particles are 40-50 nm in diameter, and quantum dots are around 2-30 nm (Clausen and Lagerholm, 2011; Sigma-Aldrich, 2014). Labels this size can experience steric hindrance when encountering the topology of the membrane (e.g. synapses) or when labeling molecules that would otherwise self-associate. The assumption is made that because the membrane is highly viscous compared to the cytosol or extracellular medium, that labels do not significantly slow down diffusion of labeled membrane components. However, the colloidal gold particles have a three-dimensional rate of diffusion approaching that of lipid molecules (Clausen and Lagerholm, 2011) and are likely to substantially affect the recorded diffusion. Furthermore, multivalent attachment

to the membrane can affect diffusion results or cluster components that in turn can cause lipid domain clustering. Quantum dots, gold, and antibodies are susceptible to this limitation. Any exogenously added label is also likely to introduce a deposited immobilized fraction, one which is void of physiological relevance but may be confused with molecules that are immobilized due to interactions under study. We chose to focus on anchors labeled with fluorescent proteins. Each fluorescent protomer is approximately 3 nanometers in diameter and are conjugated to the membrane component ensuring a 1:1 labeling stoichiometry.

The advent of photoconvertible proteins such as mEos2 and 3.2 has enabled single molecule imaging independent of expression levels/labeling density in cells. Tuning activation and excitation laser intensity controls the number of fluorescent proteins visible at a given time, resulting in a constant low density of single molecules and thousands of trajectories from a given cell.

Eos is a photoconvertible fluorescent protein from the stony coral *Lobophyllia hemprichii.* It was first characterized by Wiedenmann et al. as a green (516 nm) to red (581 nm) photoconvertible protein (Wiedenmann et al., 2004). The Eos chromophore is composed of a histidine-tyrosine-glycine tripeptide, like other green-to-red photoconvertible proteins such as Kaede, DendFP, mcavFP, and rfloRFP (Nienhaus et al., 2005). Green-to-red conversion takes place through an ultraviolet light-induced backbone cleavage mechanism (Nienhaus et al., 2005). As a tetramer, the size of Eos limited its applications, and mutations were introduced to monomerize the protein (mEos). Unable to fold above 30°C, the monomeric mEos protein has limited use in mammalian cells (McKinney et al., 2009), and further mutations were introduced to stabilize the protein

for a new version: mEos2 (McKinney et al., 2009). However, the added stability came at the cost of its monomeric character, as mEos2 forms monomers, dimers, trimers, and tetramers at higher concentrations in solution (Zhang et al., 2012). Further mutations were introduced at the oligomeric interfaces to make mEos 3.1 and 3.2 that are "truly monomeric" (Zhang et al., 2012).

While mEos2 is one of the brightest photoconvertible proteins known (Patterson, 2011), mEos 3.1 and 3.2 improve further on this photon budget and therefore localization precision. PALM applications have found mEos proteins to be localizable to a limit of 10 nm (Patterson, 2011). This makes the protein an ideal label for single particle tracking. That the majority of proteins are in the green form prior to photoconversion may also be useful for multiple applications, including complementary bulk assays (FRAP, FCS) or choosing cells to image. However, photobleaching of the green form takes place much faster than the red form (McKinney et al., 2009).

Fluorescent proteins have low quantum yield and photobleach quickly in comparison to the quantum dots, gold dots, or organic fluorophore, which represents their main disadvantage. The spatiotemporal resolution of SPT is in large part determined by these parameters. The experimental frame rates are limited by the quantum yield, and the track length is limited by photostability and density. Consequently trajectories from SPT of fluorescent proteins tend to be shorter than quantum dots or gold, and are recorded at relatively slow frame rates. In our experiments the frame rate did not exceed 50 frames per second (20 ms frames), though recordings as fast as 5 ms per frame have been performed with EGFP (Giepmans et al., 2006). In contrast, using gold particles, frames as short as 25 μs have been achieved (Fujiwara et al., 2002). Gold particles do not

photobleach and can have trajectories hundreds of displacements long, whereas fluorescent proteins typically have much shorter trajectories (Wieser and Schutz, 2008).

The inherent randomness of Brownian diffusion, combined with few points per trajectory, results in poorly defined diffusion parameters for individual tracks (Qian et al., 1991; Saxton, 1997). The resulting distributions of individual diffusion parameters are broad. The analysis of membrane heterogeneity requires distinguishing between heterogeneity arising from limitations of trajectory length versus experimental heterogeneity that reflects different environments or states (populations) of the diffuser. In this work, we present a method to make that distinction. We use simple Brownian simulations to predict the distribution widths from experimental track lengths, as well as determine diffusion coefficients (see Chapter 2).

**Choosing anchors for minimal model membrane proteins**

In this work, we track the diffusion of minimal model membrane proteins to probe the structure of the plasma membrane. These are composed of a fluorescent protein and membrane-interaction motifs. Most of the model membrane probes in this work are lipid modified. While we are particularly interested in the effect of palmitoylation on lateral diffusion, the probes we use for comparison and to characterize our experimental system involve other posttranslational lipid modifications. Post-translational modification happens on short amino acid sequences recognized by enzymes that catalyze the covalent addition of acyl chains onto the peptide chain. The following is an overview of lipid modifications relevant to our model membrane proteins.

Protein N-myristoylation is accomplished through N-myristoyl transferase which acts on the consensus sequence MGXXXS/T (Resh, 1999). N-myristoylation is

insufficient for targeting proteins to the membrane due to a low affinity interaction of $10^{-4}$ M $K_d$, and requires the addition of a poly-basic sequence, a protein-protein interaction, or an additional acylation such as palmitoylation, to effect stable membrane association (Peitzsch and McLaughlin, 1993). Despite its saturated structure, myristoylation also is insufficient to target proteins to the $L_o$ phase, though there are exceptions (Levental et al., 2010b). The myristoyl group protrudes from a myristoylated protein structure and 10 of 14 of its carbon are embedded within the lipid bilayer when membrane-associated (Murray et al., 1998). Examples also exist of myristoyl groups embedded within the protein structure, and may represent soluble forms of proteins that at other times associate with the membrane (Resh, 1999). N-myristoylated proteins appeared to take advantage of the low affinity of this acylation through reversible membrane association called myristoyl switching. Switching can be activated through ligands, electrostatics (e.g. phosphorylation), or proteolysis (Resh, 1999).

In contrast to N-myristoyl transferases, palmitoyl acyl transferases are less well characterized (Resh, 2006), and some are known to be membrane-bound (Dunphy et al., 1996). Additionally, because palmitoylation takes place at cysteines, which are fairly reactive nucleophiles, slower non-enzymatic palmitoyl reactions have been observed *in vitro.* Whether non-enzymatic reactions account for much protein-palmitoylation *in vivo* is less clear (Resh, 1999). Enzymatic removal of palmitate from cysteine residues are catalyzed by thioesterases (Martin et al., 2011). 'Palmitoylation' is sometimes called S-acylation to account for promiscuous lipidation with other acyl chains including: oleate, stearate, and arachidonate (Smotrys and Linder, 2004).

Geranylgeranylation is a C-terminal cysteine modification and one of two isoprenoid modifications (Epstein et al., 1991). Similar to N-myristoylation, it targets proteins to the membrane. The consensus sequences for geranylgeranylation are CAAL, CC or CXC, and the lipid moiety is attached by geranylgeranyl transferases from geranylgeranyl diphosphate (Jiang et al., 1995). Prenylated proteins tend not to be targeted to raft phase (Simons and Toomre, 2000).

In contrast with the lipid modifications discussed above, glycophosphatidylinositol or GPI modifications stably anchor proteins to the outer leaflet of the plasma membrane (Ferguson, 1999). They are a structurally diverse group of lipid modification with a common overall structure: the C-terminus of the protein is attached via a phosphoethanolamine linker to a glycan core, which in turn is attached to a phospholipid moiety embedded in the membrane. The glycan core is composed of phosphoinositol, glucoseamine and mannose residues with a host of other potential phophoethanolamine and sugar modifications (Paulick and Bertozzi, 2008). The modifications are essential to viability in mammals, suggesting an important role in signaling (Kawagoe et al., 1996). Indeed, clustering of GPI-anchored proteins, even by artificial means invokes a signaling response (Paulick and Bertozzi, 2008). Up to 250 different proteins are modified in this fashion, and the only demonstrable common function of the GPI linker appears to be attachment to the bilayer (Paulick and Bertozzi, 2008).

## Scope and hypotheses of the work

The overall aim of this work is to determine the effect of palmitoylation on the lateral diffusion of transmembrane proteins. As discussed in this introduction, palmitoylation is required for correct signaling by many proteins, and modulates their membrane targeting and vesicle-independent trafficking. Palmitoylation is also required for the correct signaling of many embedded transmembrane proteins even though they do not dissociate from the membrane or engage in vesicle-independent trafficking. In some cases, the palmitoylation state of transmembrane proteins changes with activation. It is less clear what the role of palmitoylation is for these proteins. Therefore, a motivating question of this work is: what is the role of palmitoylation in effecting signaling of embedded transmembrane proteins? Specifically we ask: does palmitoylation mediate its effect on signaling proteins by modulating their rates of lateral diffusion?

Palmitoylation is expected to alter the rates of lateral diffusion of membrane proteins for a variety of potential reasons. First, the size of the membrane-embedded portion of the protein may change due to palmitoylation or palmitoyl-stabilized dimerization, and therefore the rate of diffusion may change (depending on size as discussed in Chapters 3 and 4). Second, palmitoylation may affect the proteins' ability to interact with endogenous signaling partners. Finally, palmitoylation has been shown to alter the phase-preference of proteins in classical assays of phase-association such DRMs and phase-separated vesicles, and may be subject to the hypothesized lateral organization of the plasma membrane.

The contribution of each of these factors on the lateral diffusion of transmembrane proteins is investigated in the following chapters.

In Chapter 2 all methods applicable to this work are included.

In Chapter 3 the goal is to establish a method to quantify lateral diffusion and identify heterogeneity and confinement compared to Brownian diffusion. Lateral diffusion of 6 membrane protein constructs is analyzed. All but one of these are minimal model proteins whose biologically active components are removed, and therefore are not expected to interact with endogenous signaling partners. These experiments were performed in a photoprotective buffer.

In Chapter 4 the goal is to analyze the lateral diffusion of the same panel of model membrane probes as in Chapter 3, but in a HEPES imaging buffer. We modify the method in Chapter 3 to accommodate the more complicated lateral diffusion of these probes in HEPES buffer.

Together chapters 3 and 4 characterize our method and experimental system. We delineate what the effect of buffer, temperature, and size (including dimerization) is on lateral diffusion in our experimental system. By comparing proteins with different phase-associations, we also determine whether characteristic diffusion patterns result from opposing phase-associations.

Finally, in Chapter 5, the goal is to compare the diffusion of palmitoylatable and non-palmitoylatable protein constructs using the method characterized in Chapters 3 and 4.

## Works Cited


Almeida, P.F., Vaz, W.L., and Thompson, T.E. (1992). Lateral diffusion in the liquid phases of dimyristoylphosphatidylcholine/cholesterol lipid bilayers: a free volume analysis. Biochemistry (Mosc.) *31*, 6739–6747.

Anderson, R.G.W., and Jacobson, K. (2002). A Role for Lipid Shells in Targeting Proteins to Caveolae, Rafts, and Other Lipid Domains. Science *296*, 1821–1825.

Axelrod, D. (1983). Lateral motion of membrane proteins and biological function. J Membr Biol *75*, 1–10.

Baekkeskov, S., and Kanaani, J. (2009). Palmitoylation cycles and regulation of protein function (Review). Mol Membr Biol *26*, 42–54.

Bretscher, M.S., and Munro, S. (1993). Cholesterol and the Golgi apparatus. Science *261*, 1280–1281.

Brown, D.A., and London, E. (1997). Structure of detergent-resistant membrane domains: does phase separation occur in biological membranes? Biochem. Biophys. Res. Commun. *240*, 1–7.

Brown, D.A., and Rose, J.K. (1992). Sorting of GPI-anchored proteins to glycolipid-enriched membrane subdomains during transport to the apical cell surface. Cell *68*, 533–544.

Caffrey, M. (2009). Crystallizing Membrane Proteins for Structure Determination: Use of Lipidic Mesophases. Annu. Rev. Biophys. *38*, 29–51.

Calinski, D., Edwald, E., and Sunahara, R.K. (2011). Use of Model Membranes to Study GPCR Signalling Units: Insights into Monomers and Oligomers. In G Protein-Coupled Receptors: From Structure to Function, Jesus Giraldo, and J.-P. Pin, eds. (Royal Society of Chemistry Publishing), pp. 179–196.

Charollais, J., and Van Der Goot, F.G. (2009). Palmitoylation of membrane proteins (Review). Mol Membr Biol *26*, 55–66.

Chaudhuri, A., Bhattacharya, B., Gowrishankar, K., Mayor, S., and Rao, M. (2011). Spatiotemporal regulation of chemical reactions by active cytoskeletal remodeling. Proc. Natl. Acad. Sci. *108*, 14825–14830.

Cherezov, V., Rosenbaum, D.M., Hanson, M.A., Rasmussen, S.G.F., Thian, F.S., Kobilka, T.S., Choi, H.-J., Kuhn, P., Weis, W.I., Kobilka, B.K., et al. (2007). High-Resolution Crystal Structure of an Engineered Human β2-Adrenergic G Protein–Coupled Receptor. Science *318*, 1258–1265.

Chini, B., and Parenti, M. (2009). G-protein-coupled receptors, cholesterol and palmitoylation: facts about fats. J Mol Endocrinol *42*, 371–379.

Clausen, M.P., and Lagerholm, B.C. (2011). The probe rules in single particle tracking. Curr Protein Pept Sci *12*, 699–713.

Clausen, M.P., and Lagerholm, B.C. (2013). Visualization of plasma membrane compartmentalization by high-speed quantum dot tracking. Nano Lett *13*, 2332–2337.

Daumas, F., Destainville, N., Millot, C., Lopez, A., Dean, D., and Salome, L. (2003). Confined diffusion without fences of a g-protein-coupled receptor as revealed by single particle tracking. Biophys J *84*, 356–366.

Delint-Ramirez, I., Willoughby, D., Hammond, G.V.R., Ayling, L.J., and Cooper, D.M.F. (2011). Palmitoylation Targets AKAP79 Protein to Lipid Rafts and Promotes Its Regulation of Calcium-sensitive Adenylyl Cyclase Type 8. J. Biol. Chem. *286*, 32962–32975.

Dunphy, J.T., Greentree, W.K., Manahan, C.L., and Linder, M.E. (1996). G-protein palmitoyltransferase activity is enriched in plasma membranes. J. Biol. Chem. *271*, 7154–7159.

Edidin, M. (1993). Patches and fences: probing for plasma membrane domains. J. Cell Sci. *1993*, 165–169.

Edidin, M. (2003). THE STATE OF LIPID RAFTS: From Model Membranes to Cells. Annu. Rev. Biophys. Biomol. Struct. *32*, 257–283.

Eggeling, C., Ringemann, C., Medda, R., Schwarzmann, G., Sandhoff, K., Polyakova, S., Belov, V.N., Hein, B., von Middendorff, C., Schonle, A., et al. (2009). Direct observation of the nanoscale dynamics of membrane lipids in a living cell. Nature *457*, 1159–1162.

Emeis, C.A., and Fehder, P.L. (1970). Microscopic Mechanism for Diffusion and Rates of Diffusion-Controlled Reaction in Simple Liquid Solvents. J. Am. Chem. Soc. *92*, 2246–+.

Epstein, W.W., Lever, D., Leining, L.M., Bruenger, E., and Rilling, H.C. (1991). Quantitation of prenylcysteines by a selective cleavage reaction. Proc. Natl. Acad. Sci. *88*, 9668–9670.

Ferguson, M.A. (1999). The structure, biosynthesis and functions of glycosylphosphatidylinositol anchors, and the contributions of trypanosome research. J. Cell Sci. *112*, 2799–2809.

Fujiwara, T., Ritchie, K., Murakoshi, H., Jacobson, K., and Kusumi, A. (2002). Phospholipids undergo hop diffusion in compartmentalized cell membrane. J. Cell Biol. *157*, 1071–1082.

Gaibelet, G., Millot, C., Lebrun, C., Ravault, S., Sauliere, A., Andre, A., Lagane, B., and Lopez, A. (2008). Cholesterol content drives distinct pharmacological behaviours of u-opioid receptor in different microdomains of the CHO plasma membrane. Mol. Membr. Biol. *25*, 423–435.

Giepmans, B.N., Adams, S.R., Ellisman, M.H., and Tsien, R.Y. (2006). The fluorescent toolbox for assessing protein location and function. Science *312*, 217–224.

Gray, E., Karslake, J., Machta, B.B., and Veatch, S.L. (2013). Liquid general anesthetics lower critical temperatures in plasma membrane vesicles. Biophys. J. *105*, 2751–2759.

Hanson, M.A., Cherezov, V., Griffith, M.T., Roth, C.B., Jaakola, V.-P., Chien, E.Y.T., Velasquez, J., Kuhn, P., and Stevens, R.C. (2008). A Specific Cholesterol Binding Site Is Established by the 2.8 Å Structure of the Human β2-Adrenergic Receptor. Structure *16*, 897–905.

Hayashi, T., Rumbaugh, G., and Huganir, R.L. (2005). Differential regulation of AMPA receptor subunit trafficking by palmitoylation of two distinct sites. Neuron *47*, 709–723.

Heerklotz, H. (2002). Triton promotes domain formation in lipid raft mixtures. Biophys. J. *83*, 2693–2701.

Heimburg, T. (2007). Thermal biophysics of membranes (Weinheim : Chichester: Wiley-VCH ; John Wiley [distributor]).

Honerkamp-Smith, A.R., Cicuta, P., Collins, M.D., Veatch, S.L., den Nijs, M., Schick, M., and Keller, S.L. (2008). Line tensions, correlation lengths, and critical exponents in lipid membranes near critical points. Biophys J *95*, 236–246.

Honerkamp-Smith, A.R., Veatch, S.L., and Keller, S.L. (2009). An introduction to critical points for biophysicists; observations of compositional heterogeneity in lipid membranes. Biochim Biophys Acta *1788*, 53–63.

Jaakola, V.-P., Griffith, M.T., Hanson, M.A., Cherezov, V., Chien, E.Y., Lane, J.R., IJzerman, A.P., and Stevens, R.C. (2008). The 2.6 angstrom crystal structure of a human A2A adenosine receptor bound to an antagonist. Science *322*, 1211–1217.

Janes, P.W., Ley, S.C., and Magee, A.I. (1999). Aggregation of lipid rafts accompanies signaling via the T cell antigen receptor. J. Cell Biol. *147*, 447–461.

Jaqaman, K., Loerke, D., Mettlen, M., Kuwata, H., Grinstein, S., Schmid, S.L., and Danuser, G. (2008). Robust single-particle tracking in live-cell time-lapse sequences. Nat Methods *5*, 695–702.

Jiang, Y., Proteau, P., Poulter, D., and Ferro-Novick, S. (1995). BTS1 Encodes a Geranylgeranyl Diphosphate Synthase in Saccharomyces cerevisiae. J. Biol. Chem. *270*, 21793–21799.

Kawagoe, K., Kitamura, D., Okabe, M., Taniuchi, I., Ikawa, M., Watanabe, T., Kinoshita, T., and Takeda, J. (1996). Glycosylphosphatidylinositol-anchor-deficient mice: implications for clonal dominance of mutant cells in paroxysmal nocturnal hemoglobinuria. Blood *87*, 3600–3606.

Kenworthy, A.K., Nichols, B.J., Remmert, C.L., Hendrix, G.M., Kumar, M., Zimmerberg, J., and Lippincott-Schwartz, J. (2004). Dynamics of putative raft-associated proteins at the cell surface. J Cell Biol *165*, 735–746.

Klotzsch, E., and Schutz, G.J. (2013). A critical survey of methods to detect plasma membrane rafts. Philos Trans R Soc Lond B Biol Sci *368*, 20120033.

Konyakhina, T.M., Wu, J., Mastroianni, J.D., Heberle, F.A., and Feigenson, G.W. (2013). Phase Diagram of a 4-Component Lipid Mixture: DSPC/DOPC/POPC/chol. Biochim. Biophys. Acta BBA-Biomembr.

Kusumi, A., Nakada, C., Ritchie, K., Murase, K., Suzuki, K., Murakoshi, H., Kasai, R.S., Kondo, J., and Fujiwara, T. (2005). Paradigm shift of the plasma membrane concept from the two-dimensional continuum fluid to the partitioned fluid: high-speed single-molecule tracking of membrane molecules. Annu Rev Biophys Biomol Struct *34*, 351–378.

Kusumi, A., Suzuki, K.G., Kasai, R.S., Ritchie, K., and Fujiwara, T.K. (2011). Hierarchical mesoscale domain organization of the plasma membrane. Trends Biochem Sci *36*, 604–615.

Kuszak, A.J., Pitchiaya, S., Anand, J.P., Mosberg, H.I., Walter, N.G., and Sunahara, R.K. (2009). Purification and Functional Reconstitution of Monomeric μ-Opioid Receptors. J. Biol. Chem. *284*, 26732–26741.

Langley, J.N. (1905). On the reaction of cells and of nerve- endings to certain poisons, chiefly as regards the reaction of striated muscle to nicotine and to curari. J Physiol *33*, 374–413.

Lazar, D.F., and Medzihradsky, F. (1992). Altered microviscosity at brain membrane surface induces distinct and reversible inhibition of opioid receptor binding. J. Neurochem. *59*, 1233–1240.

Lazar, D.F., and Medzihradsky, F. (1993). Altered Transition Between Agonist-and Antagonist-Favoring States of μ-Opioid Receptor in Brain Membranes with Modified Microviscosity. J. Neurochem. *61*, 1135–1140.

Lee, C.C., Revington, M., Dunn, S.D., and Petersen, N.O. (2003). The lateral diffusion of selectively aggregated peptides in giant unilamellar vesicles. Biophys J *84*, 1756–1764.

Levental, I., Byfield, F., Chowdhury, P., Gai, F., Baumgart, T., and Janmey, P. (2009). Cholesterol-dependent phase separation in cell-derived giant plasma-membrane vesicles. Biochem J *424*, 163–167.

Levental, I., Lingwood, D., Grzybek, M., Coskun, U., and Simons, K. (2010a). Palmitoylation regulates raft affinity for the majority of integral raft proteins. Proc Natl Acad Sci U A *107*, 22050–22054.

Levental, I., Grzybek, M., and Simons, K. (2010b). Greasing their way: lipid modifications determine protein association with membrane rafts. Biochemistry (Mosc.) *49*, 6305–6316.

Levitt, E.S. (2010). Factors influencing opioid receptor signaling to adenylyl cyclase. University of Michigan.

Levitt, E.S., Clark, M.J., Jenkins, P.M., Martens, J.R., and Traynor, J.R. (2009). Differential effect of membrane cholesterol removal on mu- and delta-opioid receptors: a parallel comparison of acute and chronic signaling to adenylyl cyclase. J Biol Chem *284*, 22108–22122.

Lingwood, D., and Simons, K. (2010). Lipid rafts as a membrane-organizing principle. Science *327*, 46–50.

Liu, C., Paprica, A., and Petersen, N.O. (1997). Effects of size of macrocyclic polyamides on their rate of diffusion in model membranes. Biophys J *73*, 2580–2587.

Lodish, H., Berk, A., and Zipursky, S. (2000). G Protein –Coupled Receptors and Their Effectors. In Molecular Cell Biology. 4th Edition., (New York: W. H. Freeman), p. Section 20.3.

Loisel, T.P., Ansanay, H., Adam, L., Marullo, S., Seifert, R., Lagace, M., and Bouvier, M. (1999). Activation of the beta(2)-adrenergic receptor-Galpha(s) complex leads to rapid depalmitoylation and inhibition of repalmitoylation of both the receptor and Galpha(s). J Biol Chem *274*, 31014–31019.

Lommerse, P.H., Vastenhoud, K., Pirinen, N.J., Magee, A.I., Spaink, H.P., and Schmidt, T. (2006). Single-molecule diffusion reveals similar mobility for the Lck, H-ras, and K-ras membrane anchors. Biophys J *91*, 1090–1097.

Lushnikov, P.M., Sulc, P., and Turitsyn, K.S. (2012). Non-Gaussianity in single-particle tracking: Use of kurtosis to learn the characteristics of a cage-type potential. Phys. Rev. E *85*.

Macdonald-Obermann, J.L., and Pike, L.J. (2009). Palmitoylation of the EGF Receptor Impairs Signal Transduction and Abolishes High-Affinity Ligand Binding†. Biochemistry (Mosc.) *48*, 2505–2513.

Machta, B.B., Papanikolaou, S., Sethna, J.P., and Veatch, S.L. (2011). Minimal model of plasma membrane heterogeneity requires coupling cortical actin to criticality. Biophys J *100*, 1668–1677.

Martin, B.R., Wang, C., Adibekian, A., Tully, S.E., and Cravatt, B.F. (2011). Global profiling of dynamic protein palmitoylation. Nat Methods.

Mascalchi, P., Lamort, A.S., Salome, L., and Dumas, F. (2012). Single Particle Tracking reveals two distinct environments for CD4 receptors at the surface of living T lymphocytes. Biochem Biophys Res Commun *417*, 409–413.

McCormick, P.J., Dumaresq-Doiron, K., Pluviose, A.-S., Pichette, V., Tosato, G., and Lefrancois, S. (2008). Palmitoylation controls recycling in lysosomal sorting and trafficking. Traffic *9*, 1984–1997.

McKinney, S.A., Murphy, C.S., Hazelwood, K.L., Davidson, M.W., and Looger, L.L. (2009). A bright and photostable photoconvertible fluorescent protein. Nat Methods *6*, 131–133.

Meilhac, N., Le Guyader, L., Salome, L., and Destainville, N. (2006). Detection of confinement and jumps in single-molecule membrane trajectories. Phys Rev E Stat Nonlin Soft Matter Phys *73*, 011915.

Melkonian, K.A., Ostermeyer, A.G., Chen, J.Z., Roth, M.G., and Brown, D.A. (1999). Role of Lipid Modifications in Targeting Proteins to Detergent-resistant Membrane Rafts. J. Biol. Chem. *274*, 3910–3917.

Metzler, R., and Klafter, J. (2004). The restaurant at the end of the random walk: recent developments in the description of anomalous transport by fractional dynamics. J. Phys. -Math. Gen. *37*, R161–R208.

Milligan, G., Parenti, M., and Magee, A.I. (1995). The dynamic role of palmitoylation in signal transduction. Trends Biochem Sci *20*, 181–187.

Mouillac, B., Caron, M., Bonin, H., Dennis, M., and Bouvier, M. (1992). Agonist-modulated palmitoylation of beta 2-adrenergic receptor in Sf9 cells. J Biol Chem *267*, 21733–21737.

Mueller, V., Ringemann, C., Honigmann, A., Schwarzmann, G., Medda, R., Leutenegger, M., Polyakova, S., Belov, V.N., Hell, S.W., and Eggeling, C. (2011). STED Nanoscopy Reveals Molecular Details of Cholesterol- and Cytoskeleton-Modulated Lipid Interactions in Living Cells. Biophys J *101*, 1651–1660.

Munro, S. (2003). Lipid rafts: elusive or illusive? Cell *115*, 377–388.

Murray, D., Hermida-Matsumoto, L., Buser, C.A., Tsang, J., Sigal, C.T., Ben-Tal, N., Honig, B., Resh, M.D., and McLaughlin, S. (1998). Electrostatics and the membrane association of Src: theory and experiment. Biochemistry (Mosc.) *37*, 2145–2159.

Neubig, R.R. (1994). Membrane organization in G-protein mechanisms. FASEB J *8*, 939–946.

Nienhaus, K., Nienhaus, G.U., Wiedenmann, J., and Nar, H. (2005). Structural basis for photo-induced protein cleavage and green-to-red conversion of fluorescent protein EosFP. Proc. Natl. Acad. Sci. U. S. A. *102*, 9156–9159.

Parton, R.G., and Simons, K. (2007). The multiple faces of caveolae. Nat. Rev. Mol. Cell Biol. *8*, 185–194.

Patra, S.K., Alonso, A., Arrondo, J.L., and Goñi, F.M. (1999). Liposomes containing sphingomyelin and cholesterol: detergent solubilisation and infrared spectroscopic studies. J. Liposome Res. *9*, 247–260.

Patterson, G.H. (2011). Highlights of the optical highlighter fluorescent proteins. J. Microsc. *243*, 1–7.

Paulick, M.G., and Bertozzi, C.R. (2008). The Glycosylphosphatidylinositol Anchor: A Complex Membrane-Anchoring Structure for Proteins. Biochemistry (Mosc.) *47*, 6991–7000.

Peitzsch, R.M., and McLaughlin, S. (1993). Binding of acylated peptides and fatty acids to phospholipid vesicles: pertinence to myristoylated proteins. Biochemistry (Mosc.) *32*, 10436–10443.

Pike, L.J. (2006). Rafts defined: a report on the Keystone Symposium on Lipid Rafts and Cell Function. J Lipid Res *47*, 1597–1598.

Pinaud, F., Michalet, X., Iyer, G., Margeat, E., Moore, H.P., and Weiss, S. (2009). Dynamic partitioning of a glycosyl-phosphatidylinositol-anchored protein in glycosphingolipid-rich microdomains imaged by single-quantum dot tracking. Traffic *10*, 691–712.

Pralle, A., Keller, P., Florin, E.-L., Simons, K., and Hörber, J.K.H. (2000). Sphingolipid–Cholesterol Rafts Diffuse as Small Entities in the Plasma Membrane of Mammalian Cells. J. Cell Biol. *148*, 997–1008.

Prior, I.A., Harding, A., Yan, J., Sluimer, J., Parton, R.G., and Hancock, J.F. (2001). GTP-dependent segregation of H-ras from lipid rafts is required for biological activity. Nat. Cell Biol. *3*, 368–375.

Prior, I.A., Muncke, C., Parton, R.G., and Hancock, J.F. (2003). Direct visualization of Ras proteins in spatially distinct cell surface microdomains. J. Cell Biol. *160*, 165–170.

Pyenta, P.S., Schwille, P., Webb, W.W., Holowka, D., and Baird, B. (2003). Lateral diffusion of membrane lipid-anchored probes before and after aggregation of cell surface IgE-receptors. J. Phys. Chem. A *107*, 8310–8318.

Qian, H., Sheetz, M.P., and Elson, E.L. (1991). Single particle tracking. Analysis of diffusion and flow in two-dimensional systems. Biophys J *60*, 910–921.

Rasmussen, S.G., DeVree, B.T., Zou, Y., Kruse, A.C., Chung, K.Y., Kobilka, T.S., Thian, F.S., Chae, P.S., Pardon, E., Calinski, D., et al. (2011). Crystal structure of the beta2 adrenergic receptor-Gs protein complex. Nature *477*, 549–555.

Resh, M.D. (1999). Fatty acylation of proteins: new insights into membrane targeting of myristoylated and palmitoylated proteins. Biochim. Biophys. Acta BBA - Mol. Cell Res. *1451*, 1–16.

Resh, M.D. (2006). Palmitoylation of ligands, receptors, and intracellular signaling molecules. Sci. Signal. *2006*, re14.

Robinson, P.J. (1991). Phosphatidylinositol membrane anchors and T-cell activation. Immunol. Today *12*, 35–41.

Saffman, P.G., and Delbrück, M. (1975). Brownian motion in biological membranes. Proc Natl Acad Sci U A *72*, 3111–3113.

Sankaram, M.B., and Thompson, T.E. (1990). Modulation of phospholipid acyl chain order by cholesterol. A solid-state deuterium nuclear magnetic resonance study. Biochemistry (Mosc.) *29*, 10676–10684.

Saxton, M. (2009). Single Particle Tracking. In Fudamental Concepts in Biophysics: Volume I, Handbook in Modern Biophysics., T. Jue, ed. (Humana Press),.

Saxton, M.J. (1994). Anomalous diffusion due to obstacles: a Monte Carlo study. Biophys. J. *66*, 394–401.

Saxton, M.J. (1997). Single-particle tracking: the distribution of diffusion coefficients. Biophys J *72*, 1744–1753.

Saxton, M.J. (2012). Wanted: a positive control for anomalous subdiffusion. Biophys J *103*, 2411–2422.

Schroeder, R., London, E., and Brown, D. (1994). Interactions between saturated acyl chains confer detergent resistance on lipids and glycosylphosphatidylinositol (GPI)-anchored proteins: GPI-anchored proteins in liposomes and cells show similar behavior. Proc. Natl. Acad. Sci. *91*, 12130–12134.

Scolari, S., Engel, S., Krebs, N., Plazzo, A.P., De Almeida, R.F., Prieto, M., Veit, M., and Herrmann, A. (2009). Lateral distribution of the transmembrane domain of influenza virus hemagglutinin revealed by time-resolved fluorescence imaging. J Biol Chem *284*, 15708–15716.

Sezgin, E., Levental, I., Grzybek, M., Schwarzmann, G., Mueller, V., Honigmann, A., Belov, V.N., Eggeling, C., Coskun, U., Simons, K., et al. (2012). Partitioning, diffusion, and ligand binding of raft lipid analogs in model and cellular plasma membranes. Biochim Biophys Acta *1818*, 1777–1784.

Sheets, E.D., Simson, R., and Jacobson, K. (1995). New insights into membrane dynamics from the analysis of cell surface interactions by physical methods. Curr. Opin. Cell Biol. *7*, 707–714.

Shelby, S.A., Holowka, D., Baird, B., and Veatch, S.L. (2013). Distinct Stages of Stimulated FcεRI Receptor Clustering and Immobilization Are Identified through Superresolution Imaging. Biophys. J. *105*, 2343–2354.

Sigma-Aldrich (2014). Quantum Dots.

Simons, K., and Gerl, M.J. (2010). Revitalizing membrane rafts: new tools and insights. Nat Rev Mol Cell Biol *11*, 688–699.

Simons, K., and Van Meer, G. (1988). Lipid sorting in epithelial cells. Biochemistry (Mosc.) *27*, 6197–6202.

Simons, K., and Toomre, D. (2000). Lipid rafts and signal transduction. Nat Rev Mol Cell Biol *1*, 31–39.

Simons, K., and Vaz, W.L. (2004). Model systems, lipid rafts, and cell membranes. Annu Rev Biophys Biomol Struct *33*, 269–295.

Simson, R., Sheets, E.D., and Jacobson, K. (1995). Detection of temporary lateral confinement of membrane proteins using single-particle tracking analysis. Biophys. J. *69*, 989–993.

Singer, S.J., and Nicolson, G.L. (1972). The fluid mosaic model of the structure of cell membranes. Science *175*, 720–731.

Skaug, M.J., Faller, R., and Longo, M.L. (2011). Correlating anomalous diffusion with lipid bilayer membrane structure using single molecule tracking and atomic force microscopy. J. Chem. Phys. *134*.

Smotrys, J.E., and Linder, M.E. (2004). Palmitoylation of intracellular signaling proteins: regulation and function. Annu. Rev. Biochem. *73*, 559–587.

Stefanova, I., Horejsi, V., Ansotegui, I.J., Knapp, W., and Stockinger, H. (1991). GPI-anchored cell-surface molecules complexed to protein tyrosine kinases. Science *254*, 1016–1019.

Strulovici, B., Cerione, R.A., Kilpatrick, B.F., Caron, M.G., and Lefkowitz, R.J. (1984). Direct demonstration of impaired functionality of a purified desensitized beta-adrenergic receptor in a reconstituted system. Science *225*, 837–840.

Suh, B.-C., and Hille, B. (2005). Regulation of ion channels by phosphatidylinositol 4,5-bisphosphate. Curr. Opin. Neurobiol. *15*, 370–378.

Suzuki, K.G.N., Kasai, R.S., Hirosawa, K.M., Nemoto, Y.L., Ishibashi, M., Miwa, Y., Fujiwara, T.K., and Kusumi, A. (2012). Transient GPI-anchored protein homodimers are units for raft organization and function. Nat. Chem. Biol. *8*, 774–783.

Triffo, S.B., Huang, H.H., Smith, A.W., Chou, E.T., and Groves, J.T. (2012). Monitoring Lipid Anchor Organization in Cell Membranes by PIE-FCCS. J Am Chem Soc *134*, 10833–10842.

Vaz, W.L., Criado, M., Madeira, V.M., Schoellmann, G., and Jovin, T.M. (1982). Size dependence of the translational diffusion of large integral membrane proteins in liquid-crystalline phase lipid bilayers. A study using fluorescence recovery after photobleaching. Biochemistry (Mosc.) *21*, 5608–5612.

Veatch, S.L., Soubias, O., Keller, S.L., and Gawrisch, K. (2007). Critical fluctuations in domain-forming lipid mixtures. Proc Natl Acad Sci U A *104*, 17650–17655.

Veatch, S.L., Cicuta, P., Sengupta, P., Honerkamp-Smith, A., Holowka, D., and Baird, B. (2008). Critical fluctuations in plasma membrane vesicles. ACS Chem Biol *3*, 287–293.

Waheed, A.A., and Freed, E.O. (2009). Lipids and membrane microdomains in HIV-1 replication. Virus Res. *143*, 162–176.

Wang, Y.-C., Peterson, S.E., and Loring, J.F. (2013). Protein post-translational modifications and regulation of pluripotency in human stem cells. Cell Res.

Whorton, M.R., Bokoch, M.P., Rasmussen, S.G., Huang, B., Zare, R.N., Kobilka, B., and Sunahara, R.K. (2007). A monomeric G protein-coupled receptor isolated in a high-density lipoprotein particle efficiently activates its G protein. Proc Natl Acad Sci U A *104*, 7682–7687.

Whorton, M.R., Jastrzebska, B., Park, P.S., Fotiadis, D., Engel, A., Palczewski, K., and Sunahara, R.K. (2008). Efficient coupling of transducin to monomeric rhodopsin in a phospholipid bilayer. J Biol Chem *283*, 4387–4394.

Wiedenmann, J., Ivanchenko, S., Oswald, F., Schmitt, F., Röcker, C., Salih, A., Spindler, K.-D., and Nienhaus, G.U. (2004). EosFP, a fluorescent marker protein with UV-inducible green-to-red fluorescence conversion. Proc. Natl. Acad. Sci. U. S. A. *101*, 15905–15910.

Wieser, S., and Schutz, G.J. (2008). Tracking single molecules in the live cell plasma membrane-Do's and Don't's. Methods *46*, 131–140.

Xiang, Y., Rybin, V.O., Steinberg, S.F., and Kobilka, B. (2002). Caveolar localization dictates physiologic signaling of beta 2-adrenoceptors in neonatal cardiac myocytes. J Biol Chem *277*, 34280–34286.

Yeagle, P.L. (1985). Cholesterol and the cell membrane. Biochim. Biophys. Acta BBA-Rev. Biomembr. *822*, 267–287.

Yu, J., Fischman, D.A., and Steck, T.L. (1973). Selective solubilization of proteins and phospholipids from red blood cell membranes by nonionic detergents. J. Supramol. Struct. *1*, 233–248.

Zhang, M., Chang, H., Zhang, Y., Yu, J., Wu, L., Ji, W., Chen, J., Liu, B., Lu, J., Liu, Y., et al. (2012). Rational design of true monomeric and bright photoactivatable fluorescent proteins. Nat Methods *9*, 727–729.

Zheng, H., Pearsall, E.A., Hurst, D.P., Zhang, Y.H., Chu, J., Zhou, Y.L., Reggio, P.H., Loh, H.H., and Law, P.Y. (2012). Palmitoylation and membrane cholesterol stabilize mu-opioid receptor homodimerization and G protein coupling. Bmc Cell Biol. *13*.

# Chapter 2

# Materials and Methods

## Reagents and key equipment

What follows is a list of reagents and key equipment used for the experiments detailed in the following sections as well as their sources.

Table 2-1 List of reagents, key equipment and their sources.

| Reagents | Commercial Source |
|---|---|
| HeLa cells (human cervical carcinoma ATCC© CCL-2™) | American Type Culture Collection (Manassas, VA.) via generous gift of the Akira Ono Lab, University of Michigan |
| CHO cells (Chinese hamster ovary) | American Type Culture Collection (Manassas, VA.) via generous gift of the Mukesh Nyati Lab, University of Michigan |
| C6 hMOR cells | Made and characterized by Jessica Anand, generous gift of the Henry Mosberg Lab, University of Michigan. |
| RBL 2h3 cells | Generous gift of the Barbara Baird Lab, Cornell University. |
| HEK 293T | Generous gift of the Henry Mosberg Lab, University of Michigan. |
| PC12 | Generous gift of Edward Stunkel Lab, University of Michigan. |
| Dulbecco's Modified Eagle Medium (DMEM) supplemented with glutamine | Gibco, Life Technologies (Carlsbad, CA.) |
| Fetal Bovine Serum (FBS) | Gibco, Life Technologies (Carlsbad, CA.) |
| Pen/Strep Reagent | Gibco, Life Technologies (Carlsbad, CA.) |
| 0.25% Trypsin-EDTA, Phenol red solution | Gibco, Life Technologies (Carlsbad, CA.) |
| Gentamicin reagent (50 mg/ml) | Gibco, Life Technologies (Carlsbad, CA.) |
| 35 mm glass-bottomed culture dishes, no. 1.5 thickness | MatTek (Ashland, MA) |
| GeneIn™ transfection reagents | Amsbio (Abingdon, UK) |
| Opti-MEM® I Reduced Serum Media | Gibco, Life Technologies (Carlsbad, CA.) |
| 100x N.A. 1.49 oil-immersion objective | Olympus America (Center Valley, PA.) |
| IX-81 inverted microscope | Olympus America (Center Valley, PA.) |
| Ixon Ultra 897 EMCCD camera | Andor (Belfast, Northern Ireland) |
| 405 nm 'Cube' laser | Coherent (Santa Clara, CA.) |
| 488 nm 'Sapphire' laser | Coherent (Santa Clara, CA.) |
| 561nm 'Sapphire' laser | Coherent (Santa Clara, CA.) |
| LED pE excitation system | CoolLED (Andover, UK) |
| Multi band pass filter cube UMF2 | Olympus America (Center Valley, PA.) |
| glucose oxidase from *Aspergillus niger* | Sigma-Aldrich (St. Louis, MO.) |
| catalase from bovine liver | Sigma-Aldrich (St. Louis, MO.) |
| bovine serine albumin | Sigma-Aldrich (St. Louis, MO.) |
| Trizma base | Sigma-Aldrich (St. Louis, MO.) |
| glutathione | Sigma-Aldrich (St. Louis, MO.) |
| glucose | Sigma-Aldrich (St. Louis, MO.) |
| MATLAB | The MathWorks (Natick, MA. |
| Sample Temperature Feedback Cooling & Heating Stage Top Incubator (INUCP-KRi-F1) | TOKAI HIT |
| didodecyltetramethylindocarbocyanine perchlorate (DiI $C_{12}$) | Invitrogen (Grand Island, NY.) |

## Selection and design of membrane probes

Model protein design is summarized in Table 2-2. mEos2 and mEos3.2 proteins were each anchored to the membrane by the following motifs: glycophosphatidylinositol (GPI), a geranylgeranyl moiety and polybasic sequence (GG), a palmitoyl and myristoyl modification (PM), a single transmembrane domain (A- TM and B-TM), or seven transmembrane helices ($\beta_2$AR) for a total of 12 model membrane proteins. For those constructs for which protein had to be delivered to the outside of the plasma membrane (GPI, A-TM, B-TM, and $\beta_2$AR) an ER translocation sequence was added upstream of mEos2/3.2 to ensure surface delivery: MELFWSIVFTVLLSFSCRGSDWESLQSTVPR. The constructs were mEos tagged versions of previously studied probes, assembled as in the following. Transmembrane domain A was derived from linker of activated T-cell (generous gift from Akira Ono). B- TM was composed of the transmembrane domain of hemagglutinin and is dimeric (Scolari et al., 2009). The GPI sequence was derived from CD58 (Keller et al., 2001). GG came from the C-terminal sequence for K-Ras and PM was derived from the N-terminal sequence for Lyn (Pyenta et al., 2003). The full-length human $\beta_2$ adrenergic receptor (amino acid residues 2-413) made up our $\beta_2$AR (generous gift from Roger Sunahara).

Table 2-2 – Amino acid sequences of model membrane protein constructs. ER refers to an endoplasmic reticulum signaling sequence required for correct trafficking of GPI and the transmembrane constructs.

| | **Sequence** | **Citation** |
|---|---|---|
| PM | A P K L P P R A R N M G C I K S K R K D – linker(KDLELKLRILQSTVPRARDPPVAT)–**mEos** | *(Pyenta et al., 2001)* |
| GG | **mEos**–R S D G K K K K K K S K T K C Q L L | |
| GPI | *ER* – **mEos** – linker(YGGNGSGQHQYDPR) – P S S G H S R H R Y A L I P I P L A V I T T C I V L Y M N V L | (Keller et al., 2001) |
| A-TM | *ER* – **mEos** – M E A D A L S P V G L G L L L L P F L V T L L A A L A V R A R E L P V S | Generous gift from Akira Ono, Univ. of Michigan |
| A-TM palm | *ER* – **mEos** – M E A D A L S P V G L G L L L L P F L V T L L A A L C V R C R E L P V S | |
| B-TM | *ER* – **mEos** – A S I R N N T Y D H S K Y R E E A M Q NR I Q I D P V K L S S G Y K D V I L W F S F G A S C F L L L A I A M G L V F I S V K N G N M R S T I S I | (Scolari et al., 2009) |
| B-TM palm | *ER* – **mEos** – A S I R N N T Y D H S K Y R E E A M Q NR I Q I D P V K L S S G Y K D V I L W F S F G A S C F L L L A I A M G L V F I C V K N G N M R C T I C I | |
| $\beta_2$AR | *ER* – **mEos** –S S G Q P G S G S A F L L A P D G S H A P D H D V T Q Q R D E V W V V G M G I V M S L I V L A I V F G N V L V I T A I A K F E R L Q T V T N Y F I T S L A C A D L V M G L A V V P F G A A H I L M K M W T F G N F W C E F W T S I D V L C V T A S I E T L C V I A V D R Y F A I T S P F K Y Q S L L T K N K A R V I I L M V W I V S G L T S F L P I Q M H W Y R A T H Q E A I N C Y A D E T C C D F F T N Q A Y A I A S S I V S F Y V P L V I M V F V Y S R V F Q E A K R Q L Q K I D K S E G R F H V Q N L S Q V E Q D G R T G H G L R R S S K F C L K E H K A L K T L G I I M G T F T L C W L P F F I V N I V H V I Q D N L I R K E V Y I L L N W I G Y V N S G F N P L I Y C R S P D F R I A F Q E L L ***C*** L R R S S L K A Y G N G Y S S N G N T G E Q S G Y H V E Q E K E N K L L C E D L P G T E D F V G H Q G T V P S D N I D S Q G R N C S T N D S (L L) | Generous gift from Roger Sunahara, Univ. of Michigan.<br><br>(highlighted residue represents location of C341G point mutation for removing palmitate site) |
| **ER** | M E L F W S I V F T V L L S F S C R G S D W E S L Q S T V P R | |

Multiple experimenters contributed to the design and molecular cloning of these constructs. Matt Stone adapted PM and GG from the sources listed by replacing the fluorescent protein with mEos2. GPI and B-TM were re-created from the sources listed by Jonathan Grover, and I replaced their fluorescent proteins with mEos2. A-TM is a truncated mutant of linker of activated T cells, designed by Jonathan Grover, and I replaced their fluorescent proteins with mEos 2. Roger Sunahara generously provided $\beta_2$AR, and I added back the C-terminal dileucine

motif, and replaced the fluorescent protein with mEos 2. I also deleted the dileucine motif from $\beta_2$AR mEos3.2 and 2 at a later time. Endoplasmic reticulum retention motifs were added to all constructs that expressed protein on the extracellular side of the plasma membrane: including $\beta_2$AR, A-TM, and both B-TMs. mEos 2 was replaced with mEos3.2 using one restriction site upstream of the mEos gene, and pflMI, in the middle of the gene, and much of that cloning was executed by Jing Wu.

## Cell Culture

Each cell line was carried in 5 ml media; split twice weekly (20x dilution of cells from confluent flask), using trypsin 0.25% Trypsin EDTA solution to aid re-suspension. Human cervical carcinoma (HeLa) cells were grown in Dulbecco's Modified Eagle Medium (DMEM) supplemented with glutamine, 5% FBS, and 1% PenStrep reagent. HeLas were the primary cell line used for this thesis, though occasionally the following were also investigated for comparison. Chinese hamster ovary cells (CHO) cells were grown in DMEM supplemented with glutamine, 10% FBS, and 1% PenStrep reagent. Rat basophil leukemia cells (RBL) were maintained in DMEM supplemented with 20% FBS, 50 μg/ml gentamicin reagent. Human embryonic kidney cells (HEK 293T) were carried in DMEM, 10% FBS, 1% Pen/Strep reagent. Rat adrenal pheochromocytoma cells (PC-12) were maintained in F-12K (GIBCO), horse serum (15%), FBS non heat-inactivated (2.5%), and 1% pen/strep. These were a gift from the Stunkel Lab, University of Michigan. Rat brain glioma cells (C6) stably transfected with human mu opioid receptor were maintained in DMEM media, 9% FBS, and 100 μl Geneticin 50 mg/ml, 1% Pen/Strep reagent. These were generously provided by the Mosberg Lab, University of Michigan, and were originally made and characterized by Jessica Anand.

## Transfection

2 ml of cell suspension (20x dilution of cells from confluent flask) was plated in glass-bottomed MatTek dishes 12-24 hours before transfection using proprietary GeneIn™ transfection reagent from GeneIn™. The protocol was as follows.

- Cells were washed once with OptiMEM media and replace with 1 ml OptiMEM.
- 2ul red reagent added to 100 µl OptiMEM media.
- 0.5 µg * DNA added to mix. Incubated 5 min.
- 2 µl blue reagent added to mix. Incubate 15 minutes.
- Entire 104.5 µl of GeneIn-DNA complex solution added to 1 ml cell.
- Cells were incubated for 12-36 hours before imaging.

*Lower concentrations (0.1 µg) of DNA were also used in order to test for altered delivery to the membrane and did not affect diffusion results.

## Generation of GPMVs

Giant plasma membrane vesicles (GPMVs, informally 'blebs') are membrane vesicles extracted from cells, about 0.5-15 µm in diameter. GPMVs occur naturally during apoptosis, cytokinesis, cell mobility and virus entry (Charras and Paluch, 2008). GPMVs are a useful model for the plasma membrane because they retain much of plasma membrane lipid composition and the cytosol of the intact cell, without the cytoskeleton or ATP. And unlike synthetic vesicles or vesicles reconstituted from tissue lipid extracts, they also contain much of the protein content of the intact plasma membrane (Scott, 1976) and possibly its leaflet asymmetry (Baumgart et al., 2007; Yavin and Zutra, 1979). The exact mechanism of GPMV formation is unknown but is dependent on removing connections between cytoskeleton and the membrane. They can be generated by multiple methods including laser pulsation (Kelly et al., 2009), latrunculin B (Keller et al., 2009) and other cytoskeleton-targeting drugs, salt buffers (Del Piccolo et al., 2012), N-Ethylmaleimide(Scott, 1976) or a combination of reducing agent and sub-fixation

concentrations of formaldehyde (Scott, 1976). This last approach is fast, reliable, and yields a large number of blebs detached from the cell, but the choice of reducing agent affects the degree of palmitoylation of proteins found in the GPMV (Levental et al., 2010). The N-Ethylmaleimide method keeps palmitoyl modifications intact (Levental et al., 2010). Additionally sub-cytosolic concentrations of glutathione or the non-reducing agent salt concentrations protocols are expected not to change palmitoylation state. We have experimented with all three of these techniques.

**Protocol for blebbing using reducing agent**

Inactive bleb buffer: (2 mM $CaCl_2$, 10 mM Hepes, 0.15 M NaCl, pH 7.4.) Active bleb buffer: Inactive bleb buffer with 24 mM formaldehyde and 4 mM glutathione, 24 mM formaldehyde and 2 mM DTT, or 2mM N-Ethylmaleimide.

Cells were washed 3x with inactive bleb buffer. Active bleb buffer was added, just enough to cover cells. (E.g. 1 ml buffer for 25 $cm^2$ flask.) Incubated with gentle shaking at 37°C for 1-2 hours. GPMVs are harvested by gently decanting buffer from cells.

**Protocol for blebbing without reducing agent**

Flasks were rinsed twice with 30% PBS (0.3x1.06 mM $KH_2PO_4$, 2.97 mM $Na_2HPO_4$, and 155 mM NaCl). 0.5-1 ml of vesiculation buffer (200 mM NaCl, 5 mM KCl, 0.5 mM $MgCl_2$, and 0.75 mM $CaCl_2$, pH 8.5) was added to each flask and incubated for 5 hours 37°C.

CHO GPMVs generated with glutathione reducing method were used in place of HeLa in Chapter 3 and 4. GPMVs were harvested and placed in a MatTek well and imaged as with cells.

Bleb data presented in this work were executed by Jing Wu or with the assistance of Eric Sink.

**Determining transition temperature of GPMVs**

Cells are labeled with lipid intercalating dye such as DiI $C_{12}$ prior to blebbing. GPMVs are placed on the slide attached on a Peltier controlled temperature plate. Images of the sample of recorded at multiple temperatures. The fraction of blebs that are phase-separated are determined by manual counting using custom graphic user interface in written in MATLAB. Transition temperature is defined as the point at which 50% of GPMVs have phase separated, and is assessed by fitting to sigmoidal curve.

## Imaging Buffer

Hypoxic imaging buffer: 15 mg/ml glutathione, 9 mg/ml glucose, and 1 mg/ml bovine serine albumin (BSA), 65 mM Tris, 5.6 mM glucose, 100 mM NaCl, 5 mM KCl, 1 mM $MgCl_2$, 1.8 mM $CaCl_2$. Adjusted to be pH 7.5 at the experimental temperature. An enzymatic oxygen-scavenging system composed of 0.5 mg glucose oxidase from *Aspergillus niger* and 0.04 mg catalase from bovine liver was added per 1 ml imaging buffer.

HEPES imaging buffer: 135 mM NaCl, 5 mM KCl, 1 mM $MgCl_2$, 1.8 mM $CaCl_2$, 5.6 mM glucose, 1 mg/mL BSA, and 20 mM HEPES, adjusted to pH 7.4.

Inclusion of oxygen scavenging and reducing agents are necessary for the superresolution imaging of carbocyanine dyes, and is compatible with mEos 3.2 and 2. The inclusion of reducing agent has been shown to cause reversibility in mEos photoconversion (or possibly a switching between a dark and 561-excitable state) (Endesfelder et al., 2011). This results in multiple tracks

per molecule and effectively no detectable depletion of events over several minutes of recording. Furthermore, bleb formation due to phototoxicity did not occur in the presence of hypoxic imaging buffer.

## Temperature regulation and temperature experiments

Temperature regulation was accomplished using a Tokai Hit sample temperature feedback cooling & heating stage top incubator. The temperature stage is equipped with several heaters: top, stage, lens, and bath, as well as a thin temperature probe inserted directly into the sample to monitor temperature at the sample in real time. The stage can also be cooled, for which there is an attached circulating water bath. The temperature range used for all experiments was about 17 to 38°C. The microscope acts as a heat sink, so especially for the higher temperatures, e.g. 37°C, equilibration is essential for a stable temperature and the temperature of the room may also need to be adjusted. For most experiments cells were maintained at 37°C to maintain experimental conditions as physiological as possible, though in practice this was a range of about 36.8 ± 1°C.

### Temperature settings

(More details on this available from the Tokai Hit manual.)

For 37°C: top 38°C, stage 38.1-38.5°C, lens 41°C, and bath 38°C.

For 25°C: top 38°C, stage 38.1-38.5°C, lens 41°C, and bath 38°C. Cooler on.

Only the stage heater was adjusted to change the temperature of the sample. The other temperature controls needed only to be adjusted in the case of large changes (>2°C).

### Changing temperature mid-experiment

For activation energy measurements or other experiments requiring temperature adjustment mid-experiment, the temperature stage was equilibrated to 20°C and the first recording made. Recording was then stopped and each of the settings increased by 3-5 degrees. Efforts were made to allow the temperature to re-stabilize before proceeding quickly to the next recording. In this fashion, the same cell could be recorded at few different temperatures under hypoxic conditions. Recording continuously during a temperature increase was incompatible with our set-up, because temperature changes in the sample result in a change in effective working distance of the objective and therefore a drift in focus, requiring manual adjustment of the objective collar at frequent intervals.

## Imaging of mEos constructs

While mEos 3.2 and 2 have documented differences in quantum yield (McKinney et al., 2009; Zhang et al., 2012), in practice, the imaging protocol was the same for either protein. The vast majority of the proteins are in a green state but stochastically photo-convert to a red state when illuminated with ultraviolet, allowing for single particle tracking.

Cells were imaged using a 100x numerical aperture 1.49 oil-immersion objective on an inverted microscope. An electron multiplied charge coupled device (EMCCD) camera provided the necessary sensitivity to detect single molecules. Total internal reflection fluorescence (TIRF) microscopy was used for single particle tracking but wide-field illumination was used for selecting cells as follows. Cells expressing mEos constructs were identified using the 495 ± 50 nm setting on an LED light source. Cells were chosen to be fairly representative of expressing cells, moderately bright, flat without obviously three-dimensional morphology on the bottom surface, and typically without bright intracellular organelles very close to the plasma membrane.

These tend to cause higher background even in TIRF. Once a cell was chosen, the image was cropped to ensure the fastest frame rate possible, while accommodating the entire cell or region of interest.

For recording, the cell was illuminated with 561 nm at an effective laser power of 10-30 mW. TIR angle was adjusted for maximum signal with minimal background fluorescence from inside the cell. Low intensity settings were chosen for 405 TIRF illumination. The settings used ranged from 1.3 mW with thick neutral density filters in place, to 10 mW with lower neutral density filters. The particle density of 'on' probes is empirically adjusted to be as high as possible without tracks frequently overlapping, which can be assessed by eye or as discussed in the section on particle tracking.

Custom acquisition software written by Sarah Veatch (MATLAB) was used for instrument control and recording. Movies are recorded in 500 frame segments over 4-10 minutes.

Settings for a typical experiment:

Gain is set to maximum value (incrementally to avoid accidental saturation).

Acquisition time is set to 20-30 ms.

Frame transfer is on to ensure maximum frame rate.

Voltage: 4+.

Shift Speed: 0.3 μsec.

**Limiting light exposure in HEPES imaging buffer**

Imaging under normoxic conditions was the same as described above with minor alterations: Care was taken not to exceed 50 mW of 561 nm illumination, the recording time was limited to 10 movies, or about five minutes. Also, only the thicker neutral density filter setting was used for illumination with 405 nm light. Finally, as much as possible the exposure to 495 nm

LED light was also limited. White light wide-field images were recorded prior to and after each recording, to assess morphology.

## Particle localization

Fluorophores in each frame of a recording were localized using custom software written in Matlab (The MathWorks, Natick, MA) as described previously (Veatch et al., 2012). Diffraction-limited spots were fit to a two-dimensional Gaussian shape through least squares fitting using 'fminfunc()', a built-in Matlab function. Identified spots are culled to remove outliers in width, brightness, aspect ratio, and localization precision. The image area is masked to exclude regions away from the cell, and single molecules identified outside of this mask are excluded from further analysis. Settings used in the application of custom software are accounted for below.

### Module I. Particle localization

Recordings to be included in analysis are selected. A representative image of the cell to be imaged is selected. The following parameters are selected and determine how particles are localized and including, including their brightness over background, and how proximal they can be to neighboring particles. Parameters for image processing in graphic user interface: 'STORM_analyzer'.

Process image numbers: 1 to 500

High frequency filter (pixels): 0.75

Low frequency filter (pixels): 10

Event threshold: 4

Crop dimensions: whole image

Closest neighbor distance (pixels): 3.5

Radius for locating particle center: 3.5

Tolerance for fit: 0.001

Subtract average image: selected.

The particle localization is executed and is the most time consuming portion of the processing.

**Module II. Culling**

Once particle are localized, unlikely candidates are filtered out through culling. In mEos data, parameters tend to follow normal distributions around the expected values, and filtering of the specific fluorescent contaminants is not required. The values consistently used are listed below.

Intensity range (sigmas around mean): -1 to 5

Allowed widths (sigmas around mean): -3 to 3

Allowed aspect ratios (absolute numbers): 0.2 to 5

Maximum localization error (absolute numbers): 0.5

Remove consecutive hits: selected

R min (pixels): 0.5

**Module III: Alignment**

Stochastic Optical Reconstruction Microscopy (STORM)/ Photoactivatable localization microscopy (PALM) reconstruction images are generated from each set of 500 frames and are

overlaid and their points aligned in a least-squares fashion to align movies and compensate for minor stage drift. Parameters:

Align every number frames: 500

Select: Align from STORM

Max displacements (pixels): 5

Threshold (fraction of max): 0.5

Align from uncalled data: deselect

Keep structure for tracking: select

**Module IV: Generate reconstruction**

Generates an image of all particle localizations from all frames.

Original pixel calibration (nanometers/ pixel): 160

Final image resolution: 25

Final point spread function (nanometer; halfwits): 30

Contrast factor: 5

Scale bar length (micron): 5

Color map: gray

**Module V: get resolution details**

Select region of interest and determine resolution.

Number of regions: one for each cell.

Click for a region of interest and double-click inside region to select. Update and run.

This mask also specifies which region of interest to track within in subsequent sections.

## Particle Tracking

Once the map of localized particles is compiled from each frame of a recorded experiment, the image is masked so as to select only the region of interest for tracking. Single particle trajectories are generated by a simple nearest-neighbor algorithm, which connects localized fluorophores in successive frames. A custom modular graphic user interface (tracking_gui) leads users through the following steps. Each 5-10 minute experiment is analyzed in blocks of 500 frames.

**Module I. Generating tracks by connecting localized particles.**

a.) Verifying pixel size: 160 nm.

The effective pixel size is calibrated by imaging commercially available grids of known sizes. Images of the grids, which are or known dimension (512 x 512) are measured using MATLAB and the known length scale divided by the number of pixels. This calibration must be performed at each time a camera is installed or the optical path in any way altered.

b.) Define maximum step cutoff: variable between constructs and conditions.

Incorrect connections are minimized using this maximum likely step cutoff. Tracks are terminated when more than one connection can be made within the maximum step radius. This is validated in the next step, and can be adjusted as necessary.

c.) Go back number of frames: 2 or 3.

If a spot cannot be linked to the previous frame the algorithm will seek candidate spots a second or third frame back to compensate for momentary blinking of the fluorophore or occasional losses of localized molecules in image processing. Allowing the algorithm to make connection to

more than two frames back is unnecessary unless fluorophore blinking is obvious during the course of the experiment, and should be avoided if the sample is very dense with fluorophores. This simple algorithm was found to yield very comparable results to those of more complicated tracking algorithms involving global minimizations (Jaqaman et al., 2008).

**Module II. Determining mean squared displacements.**

a.) Verify that the integration time and frame rate are correct.

b.) Minimum trajectory length: 2.

User defines minimum lengths of trajectories to be included in the analysis. For this project it was unnecessary to adjust this parameter. An example where this feature may be useful is in other fluorescent labeling schemes, where a membrane-interacting free fluorescent dye may be present in the sample. In such cases, if the dye briefly adsorbs to the membrane diffuses for a frame or two and desorbs again, increasing the minimum trajectory length will ensure that the faster soluble dye will not skew the average diffusion values.

c.) Maximum trajectory length: 500.

This parameter may be adjusted to remove persistent immobile fraction such as aggregated or glass-deposited fluorophores, which, unlike our diffusing trajectories may be on for the entire 500-frame recording.

All trajectories determined in Module I are quantified as follows. We tabulate mean squared displacements (MSD) as a function of time interval ($\tau$) for all trajectories drawn from a 500 frames of a recording. The interval $\tau$, is defined in increments of frame times, where $\tau(1)$ is one frame (or in our case 20 ms), $\tau(2)$ is two frames (40 ms), etc. As a point of clarity, on a plot of

mean squared displacements versus τ the second point represents the average displacement recorded for all two-frame segments along all tracks in 500 frames, not the average displacement of particles by the second step in all trajectories. The distinction is important because the former results in higher statistics than the latter, and explains why the statistics are far poorer for later points in the trajectory. The number of 100 ms segments in a given trajectory are always fewer than the number of 20 ms segments.

At the end of this module we also plot a step size histogram to confirm that the step size distribution follows the anticipated lognormal distribution. When the max step size in Module I is too small, trajectories are prematurely cut off and the step size histogram falls off sharply. Conversely, when the max step size is too long erroneous connections are made often resulting in a second peak. (Figure 2-1) The placement of this second peak depends on the density of particles in the sample. If the density and rate of diffusion are high, these peaks can be ill resolved and care must be taken to consider density especially for fast diffusing samples.

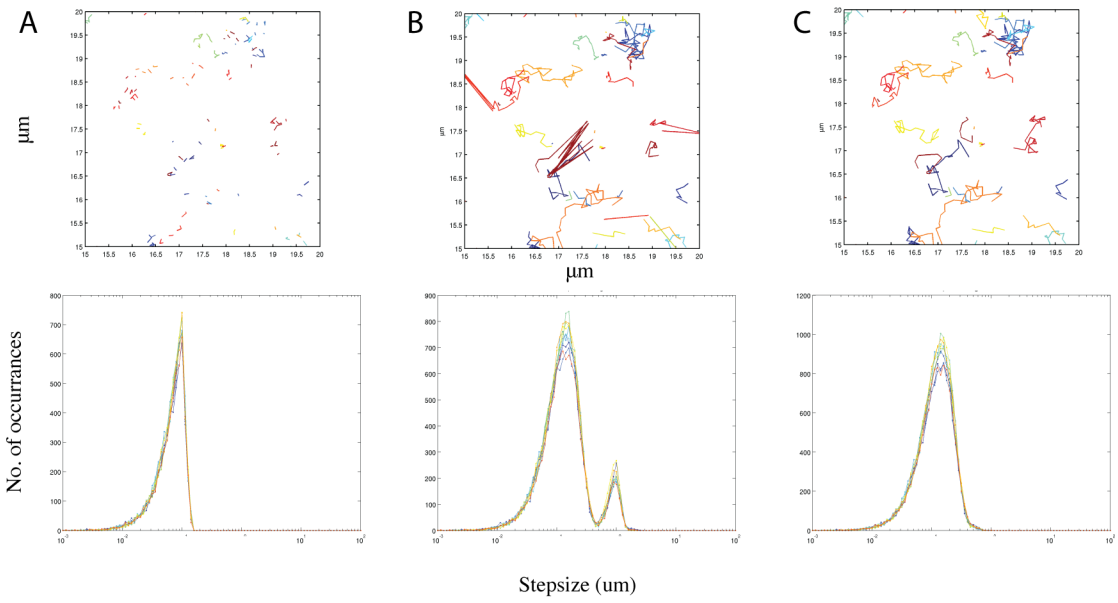


Figure 2-1. Choosing a maximum step cutoff. When the maximum step cutoff is too small such as in panel A, trajectories are prematurely terminated (top) and the step size histogram falls off sharply (bottom). The resulting diffusion constant is underestimated. In panel B where the maximum step cutoff is too large, erroneous connections are formed (top) and the step size histogram has a second peak related to density of particles in the sample (bottom). In this case diffusion constant is overestimated. Panel C demonstrates the ideal case, where the maximum step cutoff is high enough to capture all diffusers, but low enough to prevent more than the occasional erroneous connection. When the density of particles is high and diffusion is fast, these peaks tend to merge, ultimately making accurate determination of diffusion constant challenging. A dense immobile fraction poses a challenge for the same reason.

**Module III: Quantifying diffusion constants from mean squared displacements. ($D_{ave}$)**

From the mean squared displacement versus τ plots from Module II we determine the bulk diffusion constant $D_{ave}$. $D_{ave}$ is defined by fitting the 2nd through 4th points, corresponding to $40 \leq \tau_{2\text{-}4} \leq 80$ ms, of the measured MSD(τ) curves to $MSD(\tau_{2\text{-}4}) = 4D_{ave}\tau_{2\text{-}4} + C_{ave}$, where constant $C_{ave}$ accounts for the finite localization precision of the measurement in addition to possible contributions from confinement occurring at time-scales faster than probed in these measurements (Wieser and Schutz, 2008). The $D_{ave}$s are determined for each movie in an experiment and plotted over time in Module III. This allows us to appreciate changes over time.

**Module IV: Quantifying single trajectory diffusion constants. ($D_{SM}$)**

While the average diffusion constant is informative, information is lost about population

differences in diffusion behavior. To retain this information, we analyze the mean squared displacement of individual trajectories in the same way as we do average MSD. Single trajectory diffusion coefficients are determined for all trajectories extending at least 0.24s (12 segments) by tabulating $MSD_{ind}(\tau)$, averaging over segments in a single trajectory, then fitting to $MSD_{ind}(\tau_{2\text{-}4}) = 4D_{ind}\tau_{2\text{-}4} + C_{ind}$. The resulting $D_{ind}$s are then typically plotted in a histogram, which we use to determine overall diffusion constants and determine population heterogeneity, as described below under Brownian simulation-coupled analysis.

In addition to determining diffusion constants we also determine $\alpha$, the exponent of anomalous diffusion. To do this, we fit the same $MSD(\tau)$ curves to a modified form of diffusion equation, one which does not assume Brownian motion: $MSD_{ind}(\tau_{1\text{-}6}) = 4D_{ind}\tau^{\alpha}_{1\text{-}6}$. $\alpha$ provides an indication whether a diffuser experiences sub anomalous diffusion and therefore whether it is confined. $\alpha$ is one in cases of Brownian diffusion, between 1 and 0 for anomalous subdiffusion (confined diffusion), and greater than one in cases of directed motion.

## Analysis of diffusion constants using Brownian simulations

**For hypoxic conditions:** Simple Brownian trajectories were generated using MATLAB and analyzed in the same way as the experimental trajectories. Resulting distributions are used to predict the expected width of a histogram of diffusion constants of Brownian diffusers. This was done in order to determine how truly random diffusion presents in our system. The simulations were an important control because the trajectories arising from our experiments were short, yielding poorly specified single molecule diffusion constants ($D_{SM}$) and therefore broad $D_{SM}$ distributions. The simulations allowed us to 1.) identify whether the distribution was broad only because the trajectories were short or if there was also additional heterogeneity present (such as

obstacles or the diffuser existing in two states) and 2.) quantify the diffusion coefficient by fitting the experimental distribution with the simulated one.

Displacements (steps) were randomly generated and empirical data for distribution of track lengths and number-of-gaps were used to construct simulated Brownian trajectories. Gaps are instances where a trajectory contains connections that span two acquired frames. Diffusion coefficients were obtained for individual simulated tracks as described above. The experimental curve was fit with the simulated distribution by extrapolating the simulated distribution along the diffusion axis parameter using the lsqcurvefit minimization routine in Matlab. In cases where there is a significant immobile population, we also allow the amplitude of the simulated curve to vary. In Chapter 3, for cases where fitting to two distinct mobile populations is warranted, up to 4 fitting parameters are minimized: two distinct diffusion coefficients (E.g. one mobile, one immobile), and the fraction of diffusers in each population. In Chapter 4, diffusion fit parameters include diffusion constants for each population, and fraction of trajectories belonging to each population, and the immobile population is kept constant. Distributions of $\alpha$ for the simulated Brownian diffusers are also generated in Chapter 3, though these are not fit. In Chapter 4 they are fit with two Gaussian shapes.

**Simulations**

- Using the randn function in matlab we randomly assigned a number 0-1 for the step size multiplied by $\sqrt{(D*\text{dimensions}*\tau)}$, where D is the diffusion and is set to 1, and $\tau$ is the time interval (i.e. frame length = 1/frames per second).
- Trajectories of the same length as empirically determined tracks are generated from the simulated steps and their diffusion constant determined as for experimental trajectories.
- Simulation of immobile trajectories entailed the same process, except that displacements were not cumulative.
- The distribution of histogram (which is arbitrarily centered around 1) is interpolated along the diffusion axis and fit to empirically determined diffusion constants.

- Whether one population or two were more appropriate was determined visually by superimposing the experimental data on the simulated distribution.

## Bootstrapping

The bootstrapping method tests sampling error, by performing reiterative sampling. A bootstrapping analysis was performed as in Thompson *et al* (Thompson et al., 2013) for two applications. The first was to determine errors in $D_{MP}$ for single cells. The second application was to determine if experimentally determined $\alpha_{SM}$ values were significantly different from those obtained in Brownian simulations.

**Bootstrapping to determine error bounds and statistical significance.**

To determine errors in $D_{MP}$ for single cells.

- We pooled all $D_{SM}$ measured within a single cell.
- Then sampled this pool 1000 times with replacement to generate 1000 new data sets of the same size
- We determined $D_{MP}$ from each resampled set.
- The resampled $D_{MP}$ values are normally distributed, and error is determined by measuring the standard deviation.

**Bootstrapping to determine error bounds and statistical significance.**

To test the hypothesis that the empirical and simulated $\alpha_{SM}$ have the same mean we perform the following steps.

- Determined the mean of a pool of $\alpha_{SM}$ experimental data and the corresponding pool of simulated data and subtracted them. In our case these mean difference values are small (±0.03 between simulated and experimental) for all constructs.
- Combined the simulated and experimental data sets into a new mixed data pool.
- Sampled the mixed pool without replacement, to generate new data sets of the same length as the original experimental and simulated datasets, effectively randomizing their values. Their means were then subtracted as before. This step was repeated 1000 times, yielding a distribution of values centered around 0 and establishing the confidence interval.
- Significance was evaluated by comparing the difference between the mean of the experimental and simulated sets to the distribution of values obtained by re-sampling. In our

case if it falls outside the 99% confidence interval we considered it significantly different from the simulated data.

- Due to the immobile population, which was present in empirical data but not in simulation, we limited this analysis to all $\alpha_{SM}$ values above 0.5.

## Models for Diffusion vs. radius

Chapters 3 and 4 show plots of the size dependence of diffusion (Figure 3-7, Figure 3-11, and Figure 4-6). They show lines describing predictions of models describing how $D_{MP}$ should vary with radius, r. The Saffman-Delbrück (SD) equation is:

$$D_{SD} = \frac{k_B T}{4\pi\eta}\left(\ln\left(\frac{\lambda}{r}\right) - \gamma + \frac{1}{2}\right)$$

λ is the ratio of the viscosity of the membrane over the viscosity of the bulk fluid, which is the only free parameter in this model and which we set to 10 μm (Cicuta et al., 2007; Honerkamp-Smith et al., 2012; Hughes et al., 1982; Petrov and Schwille, 2008). λ was adjusted to 25 in Figure 4-6.The viscosity of the membrane (η) is λ multiplied by the viscosity of the bulk fluid, which has been measured to be 1.1 centipoise for cytoplasm proximal to the plasma membrane in other cell types (Bicknese et al., 1993). Euler's constant (γ) is 0.5772 and the 1⁄2 comes from choosing boundary conditions appropriate for proteins embedded in a membrane. To approximate the free area (FA) model (Vaz et al., 1985), we use the relation:

$$D_{FA} = A \times exp\{-r^2/a_o\}$$

A is the amplitude, which can in principle also be a function of radius (Vaz et al., 1985), but which we assume is a constant for the purposes of this study. The curves in Figure 3-7 and Figure 3-11 use A = 1μm$^2$/s. $a_o$ is the critical free area, and $a_o$ = 0.3 nm$^2$ provides a good fit to the data presented. We also consider a third functional form, which has a power law dependence

on radius instead of an exponential dependence. An additional curve shown in Figure 3-11 follows:

$$D_{PL} = \frac{C}{r^2}$$

C is a fit parameter that was chosen to be $10^5 nm^4/s$ (0.1 $\mu m^2 nm^2/s$). The plots in Figure 3-7 and Figure 3-11 how $D_{SD}$, $D_{SD}+D_{FA}$, and $D_{SD}+D_{PL}$. In Figure 3-11, we also show $D(r)/D(\sqrt{2}r)$ for these same three scenarios.

## Estimating anchor size

**(Chapters 3 and 4)** $\beta_2$AR was estimated to be a cylinder of 4 nm diameter based on pdb structure 2RH1 (Cherezov et al., 2007). A single transmembrane domain (A-TM) was estimated to be have a radius of 0.67 nm based on previous studies of multi transmembrane proteins (Eskandari et al., 1998) and a modeled single helix (Lee et al., 2003). The error is based on the minimum and maximum cross sectional area of the helix in Lee et al (Lee et al., 2003). B-TM was the approximated as $\sqrt{2}$ times the radius of A-TM. Lipid anchors were estimated as having a radius 0.41 nm each. This value was determined from the average areas of an unsaturated (Alwarawrah et al., 2010) and saturated (Edholm and Nagle, 2005; Falck et al., 2004) lipid at a range of cholesterol concentrations. The error was based on this range. mEos2-labeled anchors were approximated as $\sqrt{2}$ times the radius of the monomeric anchors listed above.

## Works Cited


Alwarawrah, M., Dai, J., and Huang, J. (2010). A Molecular View of the Cholesterol Condensing Effect in DOPC Lipid Bilayers. J. Phys. Chem. B *114*, 7516–7523.

Baumgart, T., Hammond, A.T., Sengupta, P., Hess, S.T., Holowka, D.A., Baird, B.A., and Webb, W.W. (2007). Large-scale fluid/fluid phase separation of proteins and lipids in giant plasma membrane vesicles. Proc. Natl. Acad. Sci. *104*, 3165–3170.

Bicknese, S., Periasamy, N., Shohet, S.B., and Verkman, A.S. (1993). Cytoplasmic viscosity near the cell plasma membrane: measurement by evanescent field frequency-domain microfluorimetry. Biophys. J. *65*, 1272–1282.

Charras, G., and Paluch, E. (2008). Blebs lead the way: how to migrate without lamellipodia. Nat. Rev. Mol. Cell Biol. *9*, 730–736.

Cherezov, V., Rosenbaum, D.M., Hanson, M.A., Rasmussen, S.G.F., Thian, F.S., Kobilka, T.S., Choi, H.-J., Kuhn, P., Weis, W.I., Kobilka, B.K., et al. (2007). High-Resolution Crystal Structure of an Engineered Human β2-Adrenergic G Protein–Coupled Receptor. Science *318*, 1258–1265.

Cicuta, P., Keller, S.L., and Veatch, S.L. (2007). Diffusion of liquid domains in lipid bilayer membranes. J Phys Chem B *111*, 3328–3331.

Edholm, O., and Nagle, J.F. (2005). Areas of Molecules in Membranes Consisting of Mixtures. Biophys. J. *89*, 1827–1832.

Endesfelder, U., Malkusch, S., Flottmann, B., Mondry, J., Liguzinski, P., Verveer, P.J., and Heilemann, M. (2011). Chemically induced photoswitching of fluorescent probes--a general concept for super-resolution microscopy. Molecules *16*, 3106–3118.

Eskandari, S., Wright, E.M., Kreman, M., Starace, D.M., and Zampighi, G.A. (1998). Structural analysis of cloned plasma membrane proteins by freeze-fracture electron microscopy. Proc. Natl. Acad. Sci. *95*, 11235–11240.

Falck, E., Patra, M., Karttunen, M., Hyvönen, M.T., and Vattulainen, I. (2004). Lessons of Slicing Membranes: Interplay of Packing, Free Area, and Lateral Diffusion in Phospholipid/Cholesterol Bilayers. Biophys. J. *87*, 1076–1091.

Honerkamp-Smith, A.R., Machta, B.B., and Keller, S.L. (2012). Experimental observations of dynamic critical phenomena in a lipid membrane. Phys. Rev. Lett. *108*, 265702.

Hughes, B.D., Pailthorpe, B.A., White, L.R., and Sawyer, W.H. (1982). Extraction of membrane microviscosity from translational and rotational diffusion coefficients. Biophys J *37*, 673–676.

Jaqaman, K., Loerke, D., Mettlen, M., Kuwata, H., Grinstein, S., Schmid, S.L., and Danuser, G. (2008). Robust single-particle tracking in live-cell time-lapse sequences. Nat Methods *5*, 695–702.

Keller, H., Lorizate, M., and Schwille, P. (2009). PI(4,5)P2 degradation promotes the formation of cytoskeleton-free model membrane systems. Chemphyschem *10*, 2805–2812.

Keller, P., Toomre, D., Diaz, E., White, J., and Simons, K. (2001). Multicolour imaging of post-Golgi sorting and trafficking in live cells. Nat Cell Biol *3*, 140–149.

Kelly, C.V., Kober, M.M., Kinnunen, P., Reis, D.A., Orr, B.G., and Banaszak Holl, M.M. (2009). Pulsed-laser creation and characterization of giant plasma membrane vesicles from cells. J Biol Phys *35*, 279–295.

Lee, C.C., Revington, M., Dunn, S.D., and Petersen, N.O. (2003). The lateral diffusion of selectively aggregated peptides in giant unilamellar vesicles. Biophys J *84*, 1756–1764.

Levental, I., Lingwood, D., Grzybek, M., Coskun, U., and Simons, K. (2010). Palmitoylation regulates raft affinity for the majority of integral raft proteins. Proc Natl Acad Sci U A *107*, 22050–22054.

McKinney, S.A., Murphy, C.S., Hazelwood, K.L., Davidson, M.W., and Looger, L.L. (2009). A bright and photostable photoconvertible fluorescent protein. Nat Methods *6*, 131–133.

Petrov, E.P., and Schwille, P. (2008). Translational diffusion in lipid membranes beyond the Saffman-Delbruck approximation. Biophys J *94*, L41–3.

Del Piccolo, N., Placone, J., He, L., Agudelo, S.C., and Hristova, K. (2012). Production of Plasma Membrane Vesicles with Chloride Salts and Their Utility as a Cell Membrane Mimetic for Biophysical Characterization of Membrane Protein Interactions. Anal. Chem. *84*, 8650–8655.

Pyenta, P.S., Holowka, D., and Baird, B. (2001). Cross-correlation analysis of inner-leaflet-anchored green fluorescent protein co-redistributed with IgE receptors and outer leaflet lipid raft components. Biophys J *80*, 2120–2132.

Pyenta, P.S., Schwille, P., Webb, W.W., Holowka, D., and Baird, B. (2003). Lateral diffusion of membrane lipid-anchored probes before and after aggregation of cell surface IgE-receptors. J. Phys. Chem. A *107*, 8310–8318.

Scolari, S., Engel, S., Krebs, N., Plazzo, A.P., De Almeida, R.F., Prieto, M., Veit, M., and Herrmann, A. (2009). Lateral distribution of the transmembrane domain of influenza virus hemagglutinin revealed by time-resolved fluorescence imaging. J Biol Chem *284*, 15708–15716.

Scott, R.E. (1976). Plasma membrane vesiculation: a new technique for isolation of plasma membranes. Science *194*, 743–745.

Thompson, A.R., Hoeprich, G.J., and Berger, C.L. (2013). Single-molecule motility: statistical analysis and the effects of track length on quantification of processive motion. Biophys J *104*, 2651–2661.

Vaz, W.L.C., Clegg, R.M., and Hallmann, D. (1985). Translational diffusion of lipids in liquid crystalline phase phosphatidylcholine multibilayers. A comparison of experiment with theory. Biochemistry (Mosc.) *24*, 781–786.

Veatch, S.L., Machta, B.B., Shelby, S.A., Chiang, E.N., Holowka, D.A., and Baird, B.A. (2012). Correlation Functions Quantify Super-Resolution Images and Estimate Apparent Clustering Due to Over-Counting. Plos One *7*.

Wieser, S., and Schutz, G.J. (2008). Tracking single molecules in the live cell plasma membrane-Do's and Don't's. Methods *46*, 131–140.

Yavin, E., and Zutra, A. (1979). Translocation and turnover of phospholipid analogs in plasma membrane-derived vesicles from cell cultures. Biochim. Biophys. Acta *553*, 424–437.

Zhang, M., Chang, H., Zhang, Y., Yu, J., Wu, L., Ji, W., Chen, J., Liu, B., Lu, J., Liu, Y., et al. (2012). Rational design of true monomeric and bright photoactivatable fluorescent proteins. Nat Methods *9*, 727–729.

# Chapter 3

# Diffusion of minimal protein anchors in the membranes of live cells

## Introduction

Single particle tracking (SPT) is a powerful tool for investigating living systems. Here we use SPT in conjunction with (fluorescent) photoactivatable light microscopy ((F)PALM) (Betzig et al., 2006; Hess et al., 2006; Manley et al., 2008) to study the dynamics of minimal anchor proteins in the plasma membrane of live HeLa cells. Our goal is to determine how different modes of membrane anchoring affect diffusion behavior in cells. The plasma membrane is densely packed with a variety of membrane proteins anchored to the membrane in up to three ways: by transmembrane domain, post-translational lipid modification, or polybasic sequence. Many membrane proteins utilize a combination of these three motifs (Levental et al., 2010a).

We perform SPT-PALM using the photo-switchable fluorescent protein mEos3.2 (Zhang et al., 2012). When plasma membrane anchor proteins are expressed as fusions with this fluorophore, the number of fluorescent proteins visible at a given time is controlled by tuning the intensity of activation and excitation lasers. This results in a

constant low density of single molecules even if the total surface density is high, as is frequently the case when proteins are transiently transfected (Gibson et al., 2013). This approach has advantages over single particle tracking methods that use conventional protein fluorophores because a large number of trajectories can be visualized in a single cell over an extended time-frame (Hofmann et al., 2005). Imaging photo-switchable fusion proteins also avoids potential artifacts associated with multivalent or sub-stoichiometric labeling, as can sometimes occur when proteins are labeled with ligands or antibodies conjugated to quantum dots, gold, or organic fluorophores (Clausen and Lagerholm, 2011; Kasai et al., 2011; Mittal and Bruchez, 2011).

One major disadvantage of SPT-PALM is that trajectories are frequently much shorter than those obtained using traditional fluorescent proteins, organic fluorophores, or quantum dots (Clausen and Lagerholm, 2011). This leads to inherent limitations in specifying the mobility of individual molecules, and broad distributions for diffusion parameters extracted from plots of mean squared displacement (MSD) as a function of time-interval (Qian et al., 1991; Saxton, 1997). It is possible to average over all trajectories to obtain a well-specified diffusion coefficient, but information is lost regarding heterogeneity that may be present in the membrane. To overcome these limitations, we quantify the diffusion of the mobile population by comparing to simulations of Brownian motion with the same distribution of trajectory lengths. By this method, we are able to accurately specify diffusion coefficients, test for consistency with Brownian motion, and identify multiple populations of diffusers when present.

The present work quantifies the mobility of a series of simple membrane proteins with different modes of anchoring to the HeLa cell plasma membrane. We explore how

distributions of diffusion coefficients depend on anchor type, anchor size, putative phase association, and temperature. We compare the mobility of monomeric anchors to anchors conjugated to mEos2 (McKinney et al., 2009), a photo-switchable protein previously shown to form dimers and tetramers in solution (Zhang et al., 2012). We also compare how diffusion dynamics in cells compare to the same anchors expressed in isolated plasma membrane vesicles. Overall, we find that the motion of nearly all anchors investigated at 37°C is in surprisingly good agreement with a single population Brownian diffusers at the 20 ms to several second time-scale probed in these measurements. We also find that protein mobility is strongly dependent on temperature for all anchors and strongly dependent on size for smaller anchors. Dimerization of membrane receptors is a requisite first step in the activation of many signaling pathways, including the single-helix transmembrane receptor tyrosine kinases (RTK) (Weiss and Schlessinger, 1998). Our results show that oligomerization of single leaflet or single helix proteins substantially slow down diffusion, suggesting that dimerization could be a modulator of diffusion-sensitive processes.

## Results and Discussion

### Quantifying diffusion of mobile proteins in live cells

We have characterized the diffusion of a series of biologically inert, minimal model membrane proteins in order to assess the contributions of membrane-anchoring motifs to protein mobility in intact cells. The model proteins are composed of a fluorescent protein, mEos2 (McKinney et al., 2009) or mEos3.2 (Zhang et al., 2012), anchored to the membrane by one of several membrane-interacting domains. Three of

these are lipid-anchors including a glycophosphatidylinositol (GPI) that links expressed protein to the outer membrane leaflet, and either palmitoyl-myristoyl (PM) or geranylgeranyl (GG) post-translational modifications that result in inner membrane leaflet association. Both GPI and PM have been previously used as markers for ordered lipid domains, sometimes referred to as 'lipid rafts,' in cells and model membranes (Kenworthy et al., 2004; Lommerse et al., 2006; Pyenta et al., 2001; Suzuki et al., 2012). We also examined two minimal proteins containing single-pass transmembrane helices here called A-TM and B-TM. A-TM is a truncated version of the linker of activated T-cell protein with the cysteine palmitoylation sites mutated to alanine to prevent post-translational modification, and is expected to partition away from ordered lipid domains in the absence of palmitoylation (Levental et al., 2010b). B-TM is a truncated transmembrane sequence from the influenza hemagglutinin protein, also with mutated cysteine residues to prevent palmitoylation, and B-TM has been shown to form a stable dimer (Scolari et al., 2009). In order to also investigate a multiple-pass transmembrane protein, we included the full-length $\beta_2$ adrenergic receptor ($\beta_2$AR), although this protein retains its protein interaction domains and may have some biological activity. The sequences of these constructs and their sources are accounted for in Table 2-2 of Materials and Methods and a schematic of their modes of anchoring with the membrane are depicted in Figure 3-1 *A*.

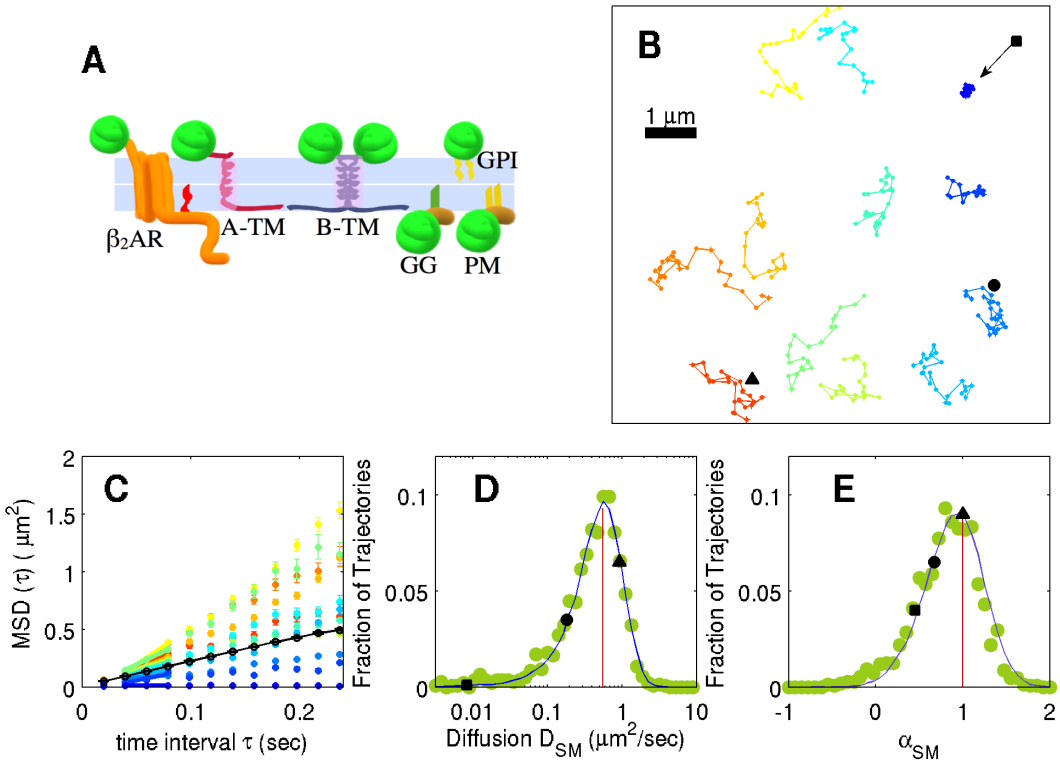


Figure 3-1 Characterizing diffusion of model membrane proteins in live cells. (A) Schematic representation of the membrane proteins used in this study, consisting of mEos2 or mEos3.2 anchored to the membrane by one of six modes. The proteins include: one glycophosphatidylinositol–linked protein expressed on the outer leaflet (GPI), two proteins localized on the inner leaflet either through a geranylgeranyl moiety (GG) or palmitoyl-myristoyl modifications (PM), and three transmembrane motifs a dimerizing single helix (B-TM), or a full-length GPCR with seven transmembrane segments ($\beta_2$AR). (B) Representative trajectories of GPI mEos3.2 recorded at 37°C at 50 frames per second. Error bars indicate localization error. (C) Plots of mean squared displacement as a function of time interval, MSD(τ) averaged over all segments in representative trajectories from panel B (color matches trajectory.) The black line represents the average MSD(τ) over the entire experiment lasting 4 min. The diffusion coefficient is determined by fitting the slope between the 2nd and 4th points of MSD(τ) corresponding to $40 \leq \tau \leq 80$ ms as described in the main text (short solid lines). (D) A histogram of single-trajectory diffusion constants determined for all tracks of at least 12 steps (0.24 sec) recorded in a single cell over 4 min. The solid line is a histogram of diffusion coefficients obtained by simulating Brownian motion with the same track-length distribution as obtained in experiment for D = 0.58 μm2/sec. The red line marks D = 0.56 μm2/sec, the diffusion coefficient determined from the black line in panel C. (E) Histogram of α values determined when MSD (τ) curves for the same trajectories as described in the main text. The solid line represents the histogram obtained from a Brownian simulation with an identical trajectory length distribution and no fit parameters. The red line marks α = 1.

We monitor the mobility of the plasma membrane-anchored proteins described above using SPT-PALM (Betzig et al., 2006; Hess et al., 2006; Manley et al., 2008). In a typical measurement, roughly 5000 individual trajectories lasting at least 12 frames are recorded over a 3-6 minute measurement. To accomplish this, we select cells that

robustly express mEos-tagged constructs by imaging fields of cells using 495 ± 50 nm LED excitation. Single proteins within these cells are resolved by photo-converting a small fraction of mEos probes to a second 561 nm-excitable state using ultraviolet (405 nm) light. Excitation and photo-conversion are accomplished with total internal reflection illumination in order to activate and excite only fluorophores located at the bottom membrane of the cell. Cells are constantly illuminated with low intensity ultraviolet light to ensure that activated fluorescent probes are continuously replenished. In this way, the number of fluorescent probes on the membrane can be finely tuned to a constant density that is low enough to resolve and track individual particles. Representative single molecule trajectories for the mEos3.2-tagged GPI construct are shown in Figure 3-1 *B*.

A reducing imaging buffer and an enzymatic oxygen-scavenging system are also used to reduce light induced cellular toxicity (van de Linde et al., 2012), improve mEos photo-stability, and enable reversible cycling between the 561 nm-excitable and a dark state (Endesfelder et al., 2011). In this buffer, cells could be imaged for extended times (>20 min) without observed blebbing, and cells did not stain with propidium iodide after extensive incubation in buffer (Figure 3-2). Similar results for lateral diffusion are obtained for B-TM in the absence of reducing agent although more significant differences are observed when the enzymatic oxygen scavenging system is removed (Figure 3-3), indicating that the physical properties of plasma membranes change as a result of hypoxia. For the purposes of this study, hypoxic conditions were retained to enable quantitative comparisons between plasma membrane anchors. Changes in the mobility of plasma membrane proteins under low oxygen conditions have been documented previously (Celedón et al., 1998; Paller, 1993) and are a topic of future study.

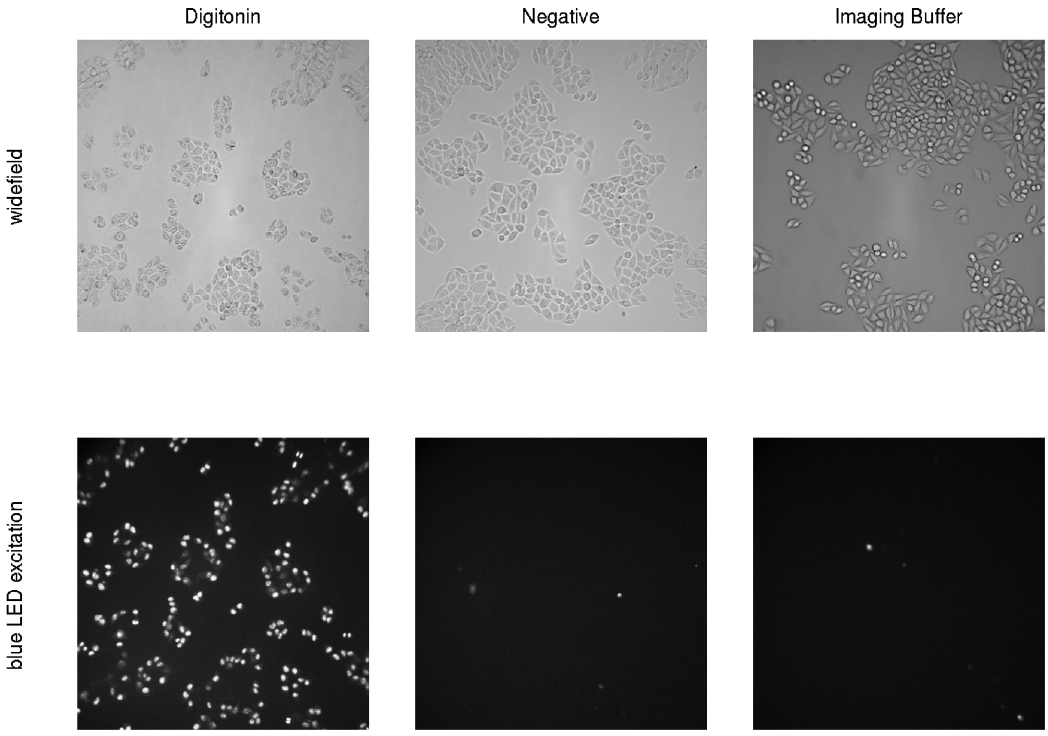


Figure 3-2 Cells remain viable after 30min incubation in hypoxic imaging buffer. HeLa were stained with 2.5 μg/ml propidium iodide in PBS and imaged using the same camera and light settings. (Left) For a positive control, cells were permeabilized with 30 μg /ml digitonin in PBS for 2 minutes at 4°C. (Middle) Negative control cells were stained immediately after removing from media containing serum. (Right) HeLa cells were incubated for 30min at 37°C in the imaging buffer containing glutathione and the enzymatic oxygen scavenging system prior to staining.

It is common practice to quantify the average diffusion of proteins by generating trajectories and then calculating the mean squared displacement (MSD) as a function of time interval ($\tau$) from all track segments (Wieser and Schutz, 2008). From this average MSD($\tau$) curve it is possible to extract an average diffusion coefficient, $D_{ave}$, by fitting a subset of the points to a line: $MSD(\tau) = 4D_{ave}\tau + C_{ave}$. The constant $C_{ave}$ accounts for the finite localization precision of the measurement in addition to possible contributions from confinement occurring at time-scales faster than probed in these measurements (Kusumi et al., 2005; Saxton, 1995). For the trajectories in Figure 3-1 *B* single molecule diffusion

coefficients are listed in Table 3-1. If MSD(τ) curves are not linear, this indicates the presence of anomalous diffusion. One way to quantify anomalous diffusion is to instead fit MSD(τ) curves to $MSD(\tau) = 4D_{\alpha}\tau^{\alpha}$, where α is the confinement exponent (Saxton, 2012). While this provides a robust method to quantify mobility of the average protein, it does not yield information regarding the heterogeneity of motion demonstrated by single molecules.

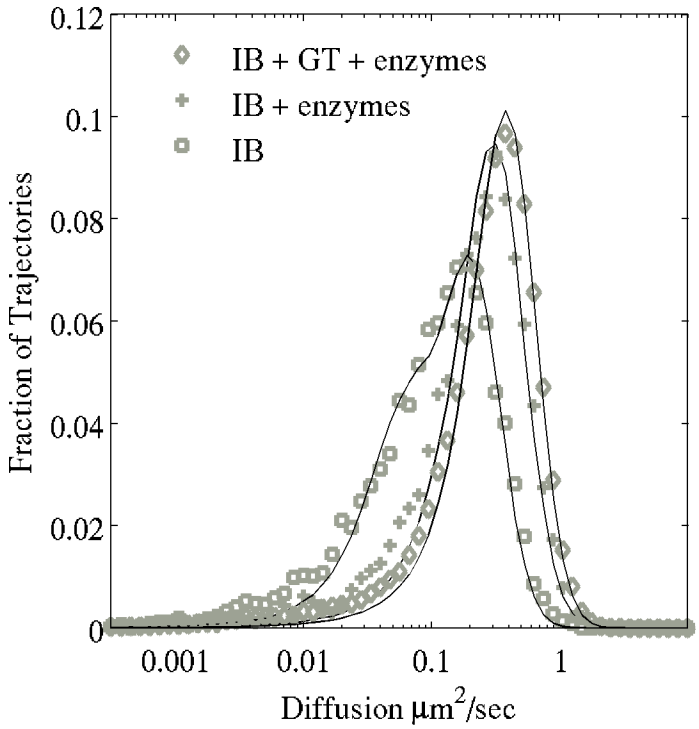


Figure 3-3 Effect of glutathione and oxygen scavenging on diffusion coefficients and heterogeneity. The data is pooled from multiple cells and fit. Diffusion constant was 0.37 $\mu m^2$/sec (n = 10) in the imaging buffer with glutathione and the oxygen scavenging system used in the rest of the study (IB + GT + enzymes). Eliminating glutathione resulted in a fit of 0.29 $\mu m^2$/sec (n = 2) (IB + enzymes). The diffusion histogram remains consistent with a single homogeneous population of Brownian diffusers. In imaging buffer alone (IB) diffusion is both slower and more heterogeneous, consistent with two populations of diffusers: 0.06 and 0.22 $\mu m^2$/sec. Fit to simulated data for each data set (solid black lines.)

In order to quantify the mobility of single molecules, we instead tabulate MSD(τ) for single trajectories extending at least 0.24 sec (12 segments) and extract a single molecule diffusion coefficient, $D_{SM}$, by fitting to $MSD_{SM}(\tau) = 4D_{SM}\tau + C_{SM}$. In this

study, we only fit to the 2nd through 4th time interval, corresponding to $40 \leq \tau \leq 80$ ms. The MSD for the first $\tau$ interval is not included in order to reduce potential artifacts due to finite integration time (Kusumi et al., 1993; Wieser and Schutz, 2008) and longer $\tau$ are not included because they average over fewer track segments and therefore have reduced counting statistics (Saxton, 1997; Wieser and Schutz, 2008). We also quantify anomalous diffusion from single trajectories through the confinement exponent $\alpha$ by fitting $MSD_{SM}(\tau)$ to $4D_{\alpha}\tau^{\alpha}$ for $\tau \leq 120$ms. The average diffusion coefficient and confinement exponent determined by fitting the $MDS(\tau)$ curve shown in Figure 3-1 *C* are $D_{ave} = 0.56 \pm 0.01$ $\mu m^2/sec$ and $\alpha_{ave} = 0.95$. Histograms summarizing the distribution of $D_{SM}$ and $\alpha_{SM}$ from trajectories acquired in a single cell are shown in Figure 3-1 *D*, *E*. For both $D_{SM}$ and $\alpha_{SM}$, the peaks of the histograms correspond to $D_{ave}$ and $\alpha_{ave}$, but the average diffusion parameters fail to represent the wide range of values observed in a single cell.

Table 3-1 - Single molecule diffusion coefficients $D_{SM}$ ($\mu m^2/sec$) for the individual tracks shown in Figure 3-1 B. The values are listed in order from red (bottom left) to blue (top right.)

| Diffusion ($\mu m^2/sec$) |
|---|
| 0.9219 |
| 1.5261 |
| 0.9047 |
| 1.5872 |
| 0.7606 |
| 1.1462 |
| 0.7668 |
| 0.6706 |
| 0.3851 |
| 0.1818 |
| 0.4858 |
| 0.0084 |

**Anchor dynamics are indistinguishable from Brownian motion**

Distributions of single molecule diffusion and confinement parameters are broad, spanning over an order of magnitude in $D_{SM}$ and ranging between 0 and 1.5 in $\alpha_{SM}$. It is not immediately apparent whether this is due to heterogeneity in motion arising from the complex cellular environment, or if it is a consequence of inherent limitations in specifying MSD($\tau$) curves for short trajectories (Saxton, 1997; Qian et al., 1991). To distinguish these alternatives, we compare our empirical distributions to ones obtained by simulating Brownian trajectories using the empirical track length distribution, as shown in Figure 3-1 *D* and *E*. Remarkably, the experimental distributions of $D_{SM}$ and $\alpha_{SM}$ are accurately described by Brownian motion using a diffusion coefficient of 0.58 $\mu m^2$/sec. This indicates that the observed heterogeneity in both parameters is dominated by the inherent spread arising from short trajectories.

The shape of histograms describing the distribution of $D_{SM}$ from Brownian simulations depends only on the track length distribution and is independent of the diffusion coefficient applied in the simulation. We take advantage of this property to extract mobile population diffusion coefficients, $D_{MP}$, from experimental histograms of $D_{SM}$ by interpolating the simulated histogram along the diffusion axis to determine the best fit to experimental data. A bootstrapping technique (Thompson et al., 2013) is applied to determine experimental error for a single cell as described in Chapter 2 Materials and Methods. For the example of B-TM mEos3.2 in Figure 3-4 *A*, $D_{MP}$ = 0.403 ± 0.006 $\mu m^2$/sec. This approach determines the diffusion constant of the mobile population independently of immobile fluorophores and with high accuracy.

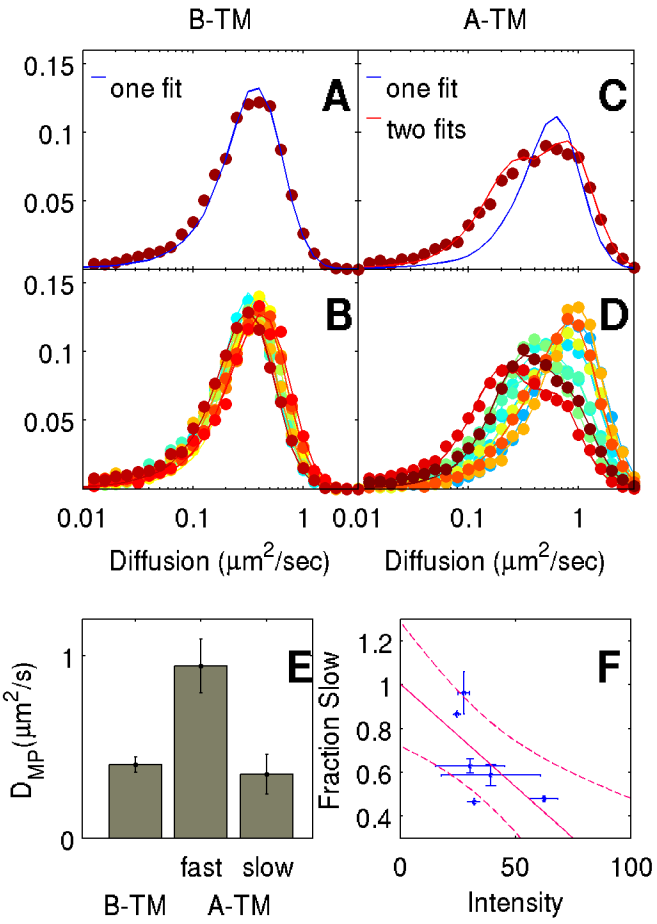


Figure 3-4 Simulations of Brownian diffusers identify diffusion heterogeneity. (A) Histogram of $D_{SM}$ acquired from a single cell expressing B-TM. The blue line represents the histogram of a single population of simulated Brownian diffusers with D = 0.403 μm$^2$ /sec. (B) Superimposed histograms from each of ten cells expressing B-TM. (C) A histogram of single molecule diffusion constants from a single cell expressing A-TM. The blue line represents the histogram of a single population of simulated Brownian diffusers. The red line represents the histogram of two populations of simulated Brownian diffusers with D = 0.25 and 0.85 μm$^2$/sec. (D) Diffusion distributions from each of ten cells expressing A-TM. The diffusion histograms are each best fit with two populations of Brownian diffusers with variable fractions of fast and slow. (E) A bar chart shows the average diffusion constants of each population from all cells B-TM, A-TM faster population ('fast'), A-TM slower population ('slow'), and their standard errors. (F) Fluorescence intensity measured in a region of interest in cells expressing A-TM plotted against the fraction slow population, suggesting that expression level is inversely correlated with slow diffusion. The line is a least-squares fit to the data, and the dotted lines represent the error bounds on the fit. The Pearson correlation coefficient was calculated as -0.51 with a p-value of 0.03.

Figure 3-4 *B* shows $D_{SM}$ histograms acquired from 10 different cells expressing the B-TM anchor when temperature is controlled at 36.8 ± 0.5°C. Each of these distributions is well described by a single population of Brownian diffusers, and we use the method described above to compare the cell-to-cell variation in $D_{MP}$. We observe remarkably little cell-to-cell variation in the mobility of this anchor, with average $D_{MP}$ = 0.40 ± 0.04 $\mu m^2$/sec, where error bounds indicate the standard deviation between cells. The effective viscosity of the plasma membrane is robust between cells, at least in HeLa cells under our imaging conditions.

Nearly all of the constructs we have investigated produce distributions of diffusion coefficients whose shapes are accurately described by a single population of Brownian trajectories. This includes the example of GPI-mEos3.2 shown in Figure 3-1 *D* and the examples of B-TM shown in Figure 3-4 *A* and *B*. A-TM is the only construct investigated that produces trajectories not well described by a single population of Brownian diffusers as illustrated in Figure 3-4 *C*. This $D_{SM}$ distribution is significantly broader than the one generated from a single population of Brownian diffusers. Instead, it is better described by a superposition of two Brownian populations, each with a different $D_{MP}$. In this example, 23% of A-TM anchors diffuse with $D_{MP}$ = 0.25 ± 0.03 $\mu m^2$/sec while 77 % of proteins diffuse with $D_{MP}$ = 0.85 ± 0.01 $\mu m^2$/sec. From this one example, it is difficult to distinguish if this distribution is representative of two distinct states that persist for longer than the lifetime of single trajectories of 0.25-2 seconds, or if the distribution is broadened because single molecules exchange between states within trajectories. Evidence supporting the presence of two long-lived states is presented in Figure 3-4 *D*, which shows $D_{SM}$ histograms from 10 cells expressing A-TM anchors.

While significant cell-to-cell variation is found for this construct, this variation is largely in the fraction of trajectories that belong to these two populations, and not to differences in the best-fit values for diffusion coefficients. $D_{MP}$ for these two populations are 0.94 ± 0.15 $\mu m^2$/sec and 0.35 ± 0.11 $\mu m^2$/sec respectively, where errors are standard deviations between the 10 cells (Figure 3-4 *D*).

One possible explanation for the two distinct populations of A-TM is that this peptide is present as both a monomer and homo-oligomer in these cells. If this were the case, we would expect that the fraction of trajectories in the slower state would be positively correlated with peptide expression level, which we do not observe. Figure 3-4 *F* plots the fraction of trajectories in the slow population vs. relative expression level as estimated by imaging mEos3.2 under 495 ± 50 nm wide-field light prior to photo-switching and single molecule imaging. Based on these observations, it is more likely that the slow population of A-TM is interacting with another endogenously expressed protein because the fraction of slower trajectories varies inversely with expression level.

Previous studies have circumvented the inherent limitations of short trajectories by instead examining cumulative probability distributions of single molecule displacements as a function of time interval (Lommerse et al., 2006), or by examining correlations between single molecule localizations in both time and space (Semrau and Schmidt, 2007; Hebert et al., 2005). In these methods, cumulative distribution functions or correlation functions are fit with an exponential to extract the MSD at each time interval or with a sum of exponentials if multiple populations are present. MSD($\tau$) curves are then used to characterize the mobility of the average diffuser. We find our current method to be complementary to these previously described methods. For the example

shown in Figure 3-4 *A*, we obtain the same diffusion coefficient for B-TM in this cell by examining the cumulative distribution of displacements as a function of time-interval (0.40 $\mu m^2/s$, Figure 3-5 *A* and *B*) when we include a second population to account for a small fraction (5%) of trajectories that are immobile. Diffusion coefficients obtained for A-TM by both methods are in qualitative but not quantitative agreement (Figure 3-5 *C* and *D*). When cumulative distribution functions are fit to a sum of two exponentials, diffusion coefficients are 0.68 and 0.09 $\mu m^2/s$ for the fast and slow components. Both values are lower than those determined by fitting distributions of $D_{SM}$ to obtain $D_{MP}$ (0.85 and 0.25 $\mu m^2/sec$). This is most likely related to there being a third minor population of immobile trajectories that are not easily fit by including a third decay time. In this context, an advantage of using distributions of $D_{SM}$ to specify diffusion coefficients is that they can be determined for the mobile population independently of immobile fluorophores. Also, heterogeneity, if present, is easily identified without the need for fitting to a sum of exponentials, which is sometimes poorly specified (Waterfall et al., 2006). One disadvantage of our approach is that it is only expected to be valid when motions are well approximated as Brownian, and therefore would not be expected to apply when probes are highly confined; such as occurs when immune receptors are clustered with multivalent antigen (Shelby et al., 2013).

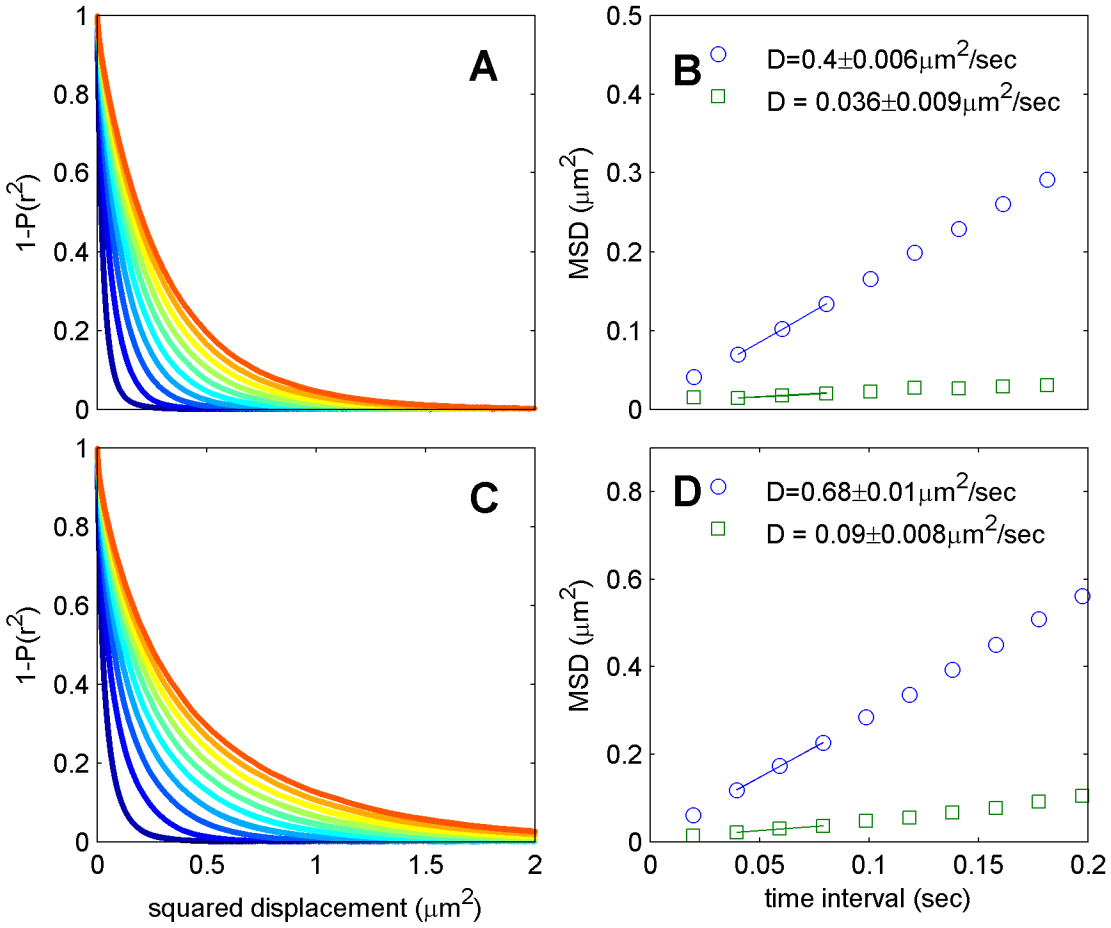


Figure 3-5 Diffusion coefficients obtained from cumulative distribution functions of B- TM mEos 3.2 and A-TM mEos 3.2. (A) Cumulative distribution functions of B-TM over sequential time intervals using the same trajectories as used in Fig 2A of the main text. (B) Fitting each to the sum of two exponentials yields mean squared displacement over time interval curves. The second population accounts for the small immobile population. These are in quantitative agreement to the Brownian simulation coupled method yielding 0.4 μm2/sec for the mobile fraction. (C) Cumulative distribution functions of A-TM over sequential time intervals using the same trajectories as used in Fig 2C of the main text. (D) When cumulative distribution functions are fit to the sum of two exponentials, diffusion coefficients are 0.68 and 0.09 μm2/sec for the fast and slow components respectively. Both values are lower than those determined by the Brownian simulation coupled method: 0.85 and 0.25 μm2/sec. The discrepancy is likely due to the contribution of a third immobile population that was not easily fit using a third exponential (not shown).

We apply the method described above to measure confinement exponents and diffusion coefficients from the mobile population of the six mEos3.2 fusion proteins schematically represented in Figure 3-1 *A* in Figure 3-6 and Figure 3-7 *A*. Figure 3-6 shows histograms $\alpha_{SM}$ and Figure 3-7 *A* shows histograms of $D_{SM}$ where in both cases single trajectory parameters are pooled from at least 5 cells to improve statistics. With the

exception of A-TM, a single population of Brownian diffusers accurately describes the mobility of all probes. Empirical $D_{SM}$ distributions are also fit to obtain $D_{MP}$ on a cell-by-cell basis, and these values are reported in Figure 3-7, with error bounds that indicate the standard error between cells.

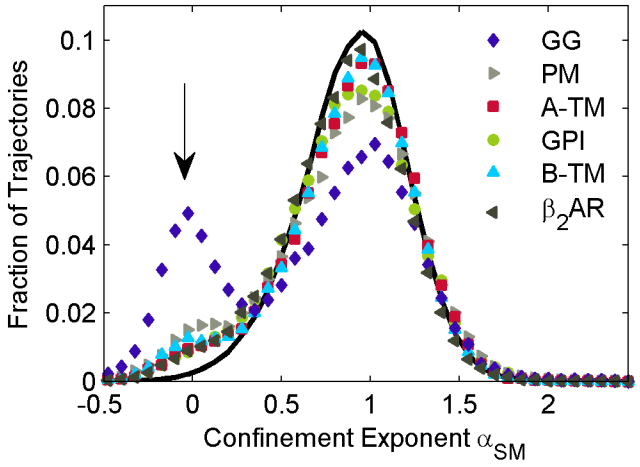


Figure 3-6 Diffusion of mobile population is unconfined. Overlaid histograms of $\alpha_{SM}$ for cells expressing all six mEos3.2 fusion proteins. Immobile population appears at $\alpha = 0$ (black arrow) whereas the mobile population is centered at $\alpha = 1$ consistent with unconfined diffusion. The black line represents a histogram of $\alpha_{SM}$ from simulated Brownian trajectories. Significance of differences between the simulated and experimental confinement values are presented in Table 3-2.

**An immobile population is observed for all anchors**

Immobile trajectories are easily identified in histograms of $\alpha_{SM}$ as a peak centered around $\alpha = 0$ and follow a broad distribution in histograms of $D_{SM}$ centered near $D_{SM}$ = 0.01 $\mu m^2$/sec for the imaging conditions used here. In the example of GPI mEos3.2 shown in Figure 3-1 *D* and *E*, the vast majority of observed trajectories are mobile (95%) as seen previously (Kenworthy et al., 2004). In this case $D_{ave}$ and the peak of $D_{SM}$ give roughly the same value for diffusion coefficient, as indicated in Figure 3-1 *D*. We have also investigated constructs that contain a larger percentage of immobile trajectories, an example being GG-mEos3.2 (Figure 3-8 and Figure 3-6). For GG-mEos3.2, we observe

a pronounced peak centered at $\alpha_{SM} = 0$, in good agreement with previous studies which also found a large fraction of highly confined trajectories of a prenylated probe (Lommerse et al., 2006). We also find a large number of immobile trajectories of GG-meos3.2 outside of the cellular footprint, suggesting that this anchor is excreted or otherwise deposited on the cover-glass and therefore does not reflect features of the membrane (Figure 3-9).

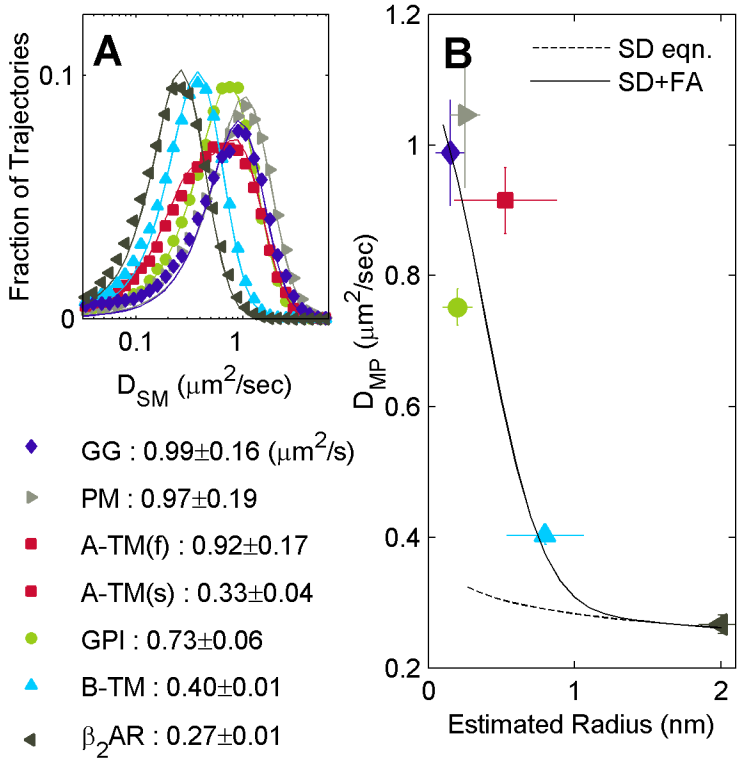


Figure 3-7 Rate of diffusion of mEos 3.2 proteins decreases with increasing anchor size. (A) Single molecule diffusion constant ($D_{SM}$) distributions are presented for each mEos 3.2 fusion protein along with its fit to simulated data (solid lines.) All distributions are accounted for by a single population of diffusers except A- TM. (B) Diffusion values for the mobile populations and faster A-TM mobile population are plotted against estimated anchor size. Error bars on the x-axis represent uncertainty in size estimation (see Materials and Methods) and y-axis error bars are the standard error of means of $D_{MP}$ averaged over at least 5 cells (also shown on left). Models represented include the Saffman-Delbrück (SD eqn), and a superposition of the SD and free area (FA) models (SD+FA) as detailed in Materials and Methods.

In previous studies, confined or immobile trajectories have been attributed to specific interactions between diffusing proteins and components bound to cortical

cytoskeleton(Valentine and Haggie, 2011), or from putative association of diffusing proteins with more ordered lipid domains (Meder et al., 2006). In our studies, we find the origin of the immobile population to be challenging to interpret. Overall, we do not observe a larger fraction of confined probes in cells expressing PM, GPI, or $\beta_2$AR anchors thought to be associated with more ordered lipid domains, suggesting that ordered lipids do not contribute significantly to this mode of motion. Also, the majority of probes investigated here are minimal anchors and are not expected to engage in significant interactions with other protein components, including those associated with cortical actin. The exception is $\beta_2$AR, where previous studies in other cell types have found a significant fraction of immobile trajectories arising from direct tethering to cytoskeleton through PDZ and AKAP binding (Valentine and Haggie, 2011). In HeLa cells under hypoxic imaging conditions, we do not observe a large immobile population for $\beta_2$AR, nor do we observe that mutations to interrupt PDZ binding impact the number of immobile trajectories (Figure 3-10), suggesting that binding to actin through this mechanism is not a major factor in these experiments. It is possible that direct interactions between anchors and glass plays a role in the observed confinement of all constructs, or that confined trajectories are present in internal structures such as endocytic vesicles that are visible in the TIR field. For this reason, we refrain from attributing much significance to the immobile component and instead focus on the mobile fraction for our analysis.

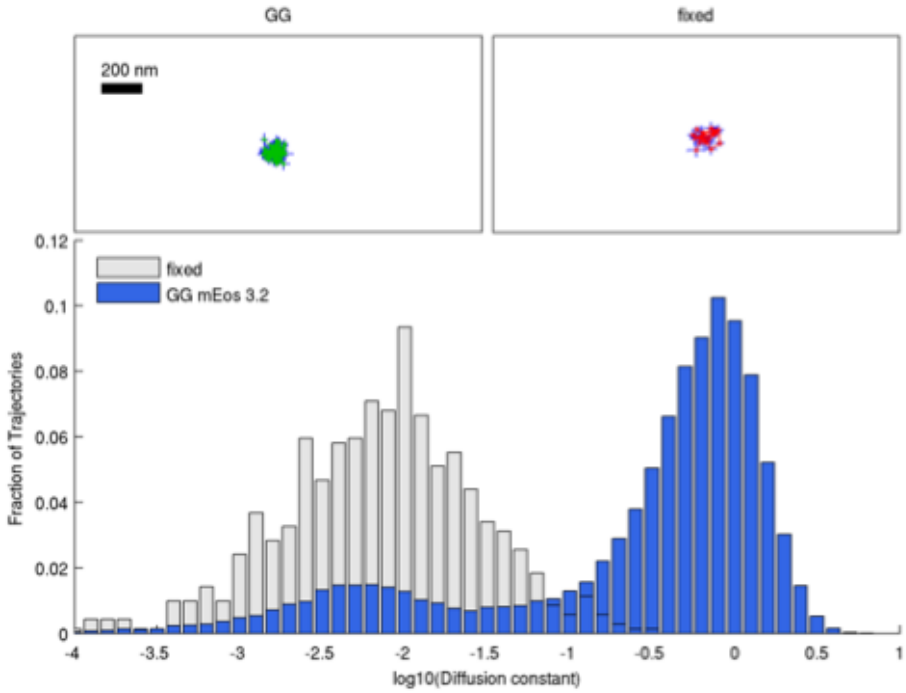


Figure 3-8 Diffusion constant of immobile fraction is accounted for by localization error. (Top) A representative trajectory of an immobile fluorophore from a GG mEos 3.2- expressing sample (left) and a trajectory from a fixed cell sample expressing B-TM mEos 3.2 (right). Error bars estimating localization precision for points within both trajectories are shown in blue. (Bottom) Histograms of diffusion constant are shown for the fixed (white) and GG (blue) samples. The diffusion constant of the fixed sample encompasses a broad range centered around 0.01 $\mu m^2/sec$, and is approximately overlaid with the immobile fraction of GG mEos 3.2 sample. The slightly higher Diffusion coefficient at the peak value of the fixed fraction compared to the immobile GG mEos 3.2 fraction can be attributed to the reduced quantum yield of the fluorophore upon fixation, resulting in reduced localization precision and subsequently higher apparent diffusion constant. These observations are consistent with the immobile fraction being immobile to a resolution of 30 nm.

### The mobile population is not confined

The six mEos3.2 fusion proteins also appear unconfined at the time-scales investigated in this measurement, with a $\alpha_{SM}$ distributions centered around 1, in good agreement with those of simulated of Brownian diffusers as shown in Figure 3-6. A-TM exhibits only one mobile peak in histograms of $\alpha_{SM}$ even though two mobile populations are observed when examining $D_{SM}$, indicating that both states are unconfined. We performed bootstrap analysis (Thompson et al., 2013) to determine the significance of

differences between $\alpha_{SM}$ distributions from experimental and simulated Brownian trajectories. While the differences are small, they are significant at a 99% confidence interval, with the exception of GPI (Table 3-2). A-TM, B-TM, GG, and PM produce histograms of $\alpha_{SM}$ that are marginally shifted to higher values than expected for Brownian diffusion suggesting that these probes undergo slightly directed motion. In contrast, distributions for $\beta_2$AR are slightly shifted to lower values, indicating that they are marginally confined. This could be due to interactions with other endogenous factors since this construct retains its protein interaction domains.

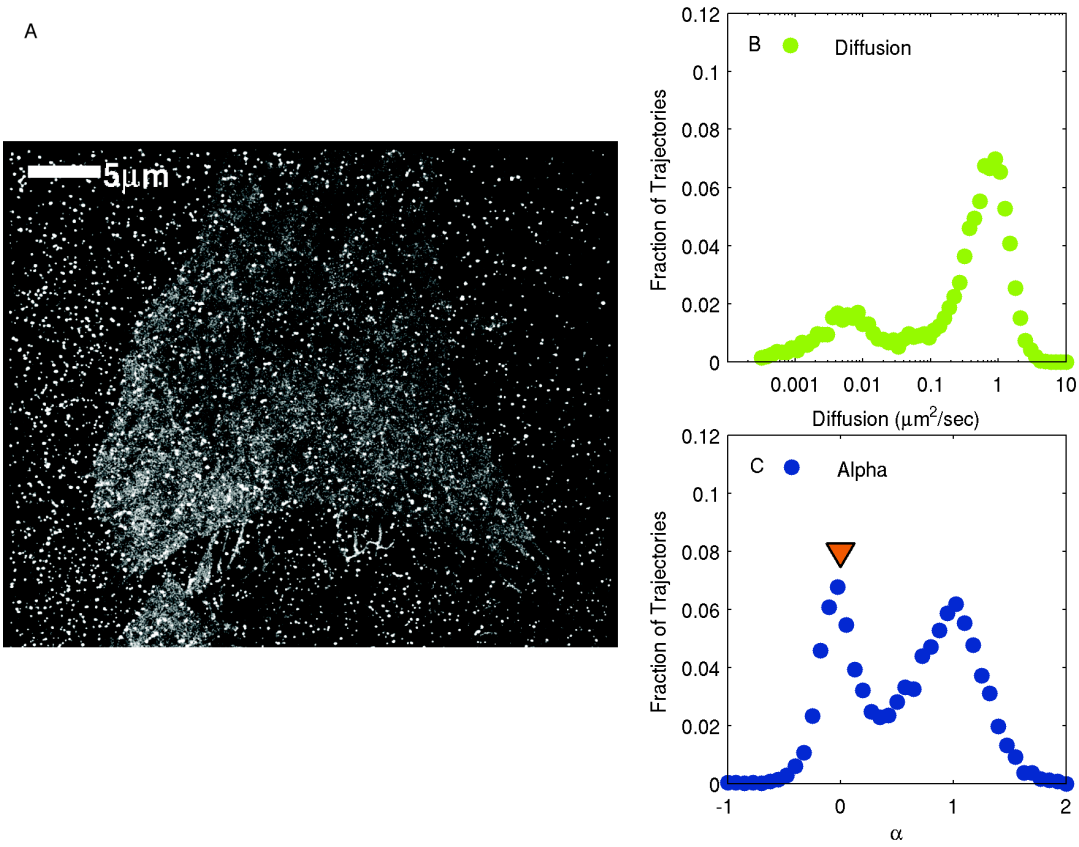


Figure 3-9 Some immobile particles are glass deposited. (A) Reconstruction of localized particles from a cell expressing GG mEos 3.2. All fluorescent events in each of 7500 frames are represented. Immobile particles appear repeatedly in the same spot, and are recognized in this picture as brighter puncta. Immobile particle appear outside the footprint of the cell in this figure, suggesting that immobile fluorophores are deposited on the glass surface. (B, C) Histograms of $D_{SM}$ and $\alpha_{SM}$ for this cell both show a significant immobile population.

Overall, protein diffusion is remarkably consistent with Brownian motion over the time and distance scales investigated in this study. Previous studies have presented significant evidence of confined motions at shorter time and distance scales than were accessible in our experiments. For example, studies have shown that single proteins diffuse quickly on very short time-scales, but take additional time to hop between barriers presented by cortical actin (Kusumi et al., 2005). GPI-linked proteins, including one similar to the construct examined here, have been shown to transiently associate on time-scales of 50 ms (Suzuki et al., 2012). Also some membrane components, mainly lipids

containing a sphingo-linkage, have been shown to experience transient immobilization on time-scales of 10 ms (Eggeling et al., 2009; Sahl et al., 2010). In all of these examples, the motions described are not expected to be observable in the experiments presented here. The displacement over one frame (20 ms) is on the order of 150 nm even for the slowest mEos 3.2 protein examined at 37°C. Our observation that the motions of all constructs appears Brownian indicates that any complex interactions that occur on these small time and distance scales help to determine the long time diffusion coefficient and do not also introduce confinement at longer times. It is possible that GPI-mEos3.2 diffuses more slowly in our experiments than PM-mEos3.2 due to indirect interactions with actin (Chaudhuri et al., 2011) or transient dimerization on time-scales shorter than accessible to our measurement (Suzuki et al., 2012; Kusumi et al., 2005).

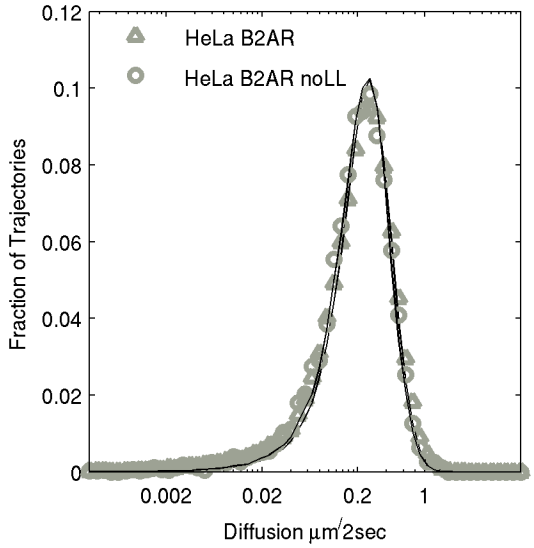


Figure 3-10 – Deleting the dileucine motif has no effect on lateral diffusion. An LL deletion mutation introduced to eliminate the interaction with PDZ domain as in Valentine et al. but has no effect on lateral diffusion in our system. Rates of diffusion: $\beta_2$AR = 0.28 μm²/sec, $\beta_2$AR without LL = 0.26 μm²/sec.

**Protein mobility depends on anchor size**

Not surprisingly, we observe that anchor mobility depends on anchor size. In Figure 3-6 *B* we plot the rate of diffusion against the radius of the membrane anchor, estimated as described in Materials and Methods. Overall, diffusion coefficients are highest for probes that are anchored to a single leaflet of the plasma membrane through lipid modifications. The mobility of GPI, which is anchored on the outer leaflet, is lower than that of GG and PM, which reside on the inner leaflet, possibly due to differences in effective viscosity of these two monolayers or transient dimerization. The faster population of A-TM is expected to be a single transmembrane helix and has a diffusion coefficient that resembles that of the inner leaflet anchored probes. B-TM is presumed to be a dimer (Scolari et al., 2009) consisting of two transmembrane helices and it diffuses more slowly. Finally, $\beta_2$AR is both the largest and the slowest membrane anchor investigated, with seven transmembrane helices.

A large number of previous theoretical and experimental studies have sought to describe how the mobility of membrane inclusions should depend on anchor size in simple membranes (Balcom and Petersen, 1993; Cicuta et al., 2007; Gambin et al., 2006; Guigas and Weiss, 2006; Harb et al., 2012; Lee et al., 2003; Liu et al., 1997; Petrov and Schwille, 2008; Ramadurai et al., 2009; Vaz et al., 1984, 1985, 1982), and our observed size-dependent mobility is not described by a single model of diffusion. The Saffman-Delbrück (SD) equation (Saffman and Delbrück, 1975) or one of its variations (Almeida and Vaz, 1995; Evans and Sackmann, 1988; Hughes et al., 1982) is expected to apply for larger inclusions, where the anchor is both larger than the size of a single lipid (~1 nm) and smaller than the hydrodynamic length, $\lambda$. $\lambda$ is a ratio of the 2 dimensional viscosity of

the membrane and the 3 dimensional viscosity of the surrounding fluid and has been measured to be on the order of several microns in model bilayer membranes (Cicuta et al., 2007; Honerkamp-Smith et al., 2012; Hughes et al., 1982; Petrov and Schwille, 2008). In this regime, protein diffusion is predicted to vary only weakly with radius, going as $ln(1/r)$. The SD eqn. with $\lambda$=10 μm accurately describes the diffusion coefficient for the multi-pass transmembrane anchor $\beta_2$AR, but fails to capture the increased diffusion coefficients of the smaller anchors. This is expected because the SD eqn. and other continuum models do not apply to anchors whose radii are close to the size of the average lipid. In this size regime, it becomes important to also consider the hopping of the diffuser around solvent molecules as it undergoes diffusive motions(Nir and Stein, 1971) and diffusion depends more strongly on anchor radius in model membranes (Gambin et al., 2006; Harb et al., 2012; Lee et al., 2003; Liu et al., 1997; Ramadurai et al., 2009). A free area (FA) model has been proposed that considers the probability of hopping into regions with enough free area to accommodate the diffuser (Almeida and Vaz, 1995; Cohen and Turnbull, 1959; Galla et al., 1979; Vaz et al., 1982, 1984, 1985). The FA model gives diffusion coefficient that depends exponentially on area, or as a Gaussian function with radius. A superposition of the SD eqn. and an approximation of the FA model is in good general agreement with our observations, although we observe significant scatter in diffusion coefficients between constructs. This likely indicates that factors other than hydrodynamics or hopping play important roles in determining the mobility of proteins on the time-scales investigated. These could include effects due to protein crowding, transient interactions with immobile membrane components, or corralling by the cortical actin cytoskeleton, but not putative phase

association consistent with previous observations (Kenworthy et al., 2004; Lommerse et al., 2006).

Table 3-2 Mean α values from experiment and simulated Brownian data are very similar, but differences are statistically significant(*) for all except GPI.

| Construct | α values |
|---|---|
| GG mEos 3.2 | 1.03 * |
| PM mEos 3.2 | 1.02 * |
| GPI mEos 3.2 | 1.00 |
| A-TM mEos 3.2 | 1.02* |
| B-TM mEos 3.2 | 1.01* |
| $\beta_2$AR mEos 3.2 | 0.97* |
| Simulated | 0.99-1.00 |

**Protein diffusion is slowed with mEos2**

The photoconvertible fluorescent proteins mEos3.2 and mEos2 differ only by three amino acids but the latter can form concentration-dependent oligomers in solution, ranging from monomers to tetramers (McKinney et al., 2009; Zhang et al., 2012). We find that replacing mEos3.2 with mEos2 results in slower diffusion for most anchor proteins, consistent with mEos2 forming oligomers. Figure 3-11 *A* shows superimposed $D_{SM}$ histograms of mEos3.2 or mEos2 conjugated anchors. Proteins anchored to the plasma membrane through acyl chains (GG, PM, and GPI) show the largest reductions in single molecule diffusion coefficients while distributions of $D_{SM}$ for the transmembrane proteins B-TM and $\beta_2$AR are not greatly affected by the choice of label. Both A-TM fusion proteins exhibit two populations, and we observe that the faster component experiences a larger reduction in diffusion compared to the slower component.

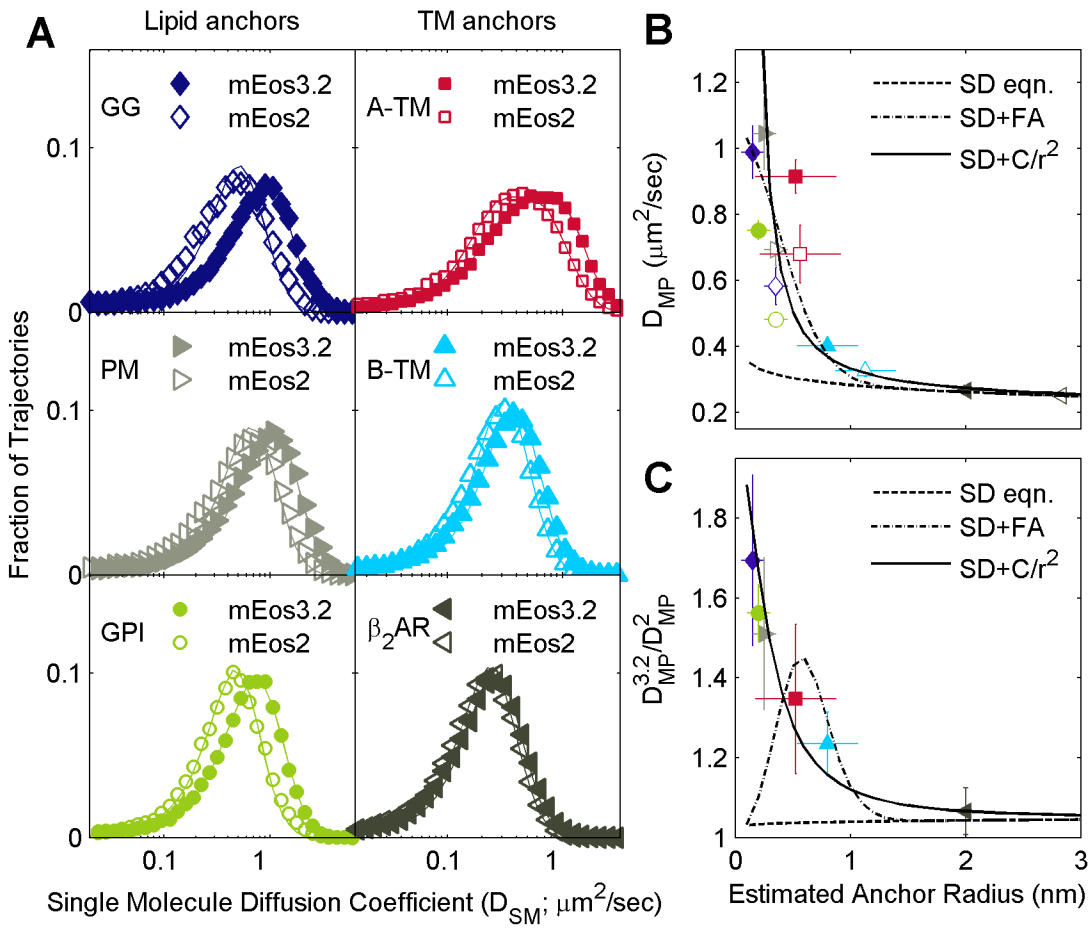


Figure 3-11 Protein diffusion is slowed with mEos2. (A) Superimposed histograms of single molecule diffusion coefficients ($D_{SM}$) from cells expressing either mEos3.2 or mEos2 fusion proteins. mEos2 lipid-anchored proteins, GPI, PM, and GG, are shifted towards lower diffusion coefficients than mEos 3.2. Transmembrane proteins appear to be less affected. A-TM fast population is slowed more than the slow population. (B) $D_{MP}$ values for all twelve fusion proteins are plotted versus estimated size. Only the faster population is included for A-TM. Models represented include the Saffman-Delbrück (SD eqn), a superposition of the SD and free area models (SD+FA), SD plus a third functional form $C/r^2$ (SD+ $C/r^2$) as detailed in Materials and Methods. mEos 2 anchor sizes are estimated as dimers of mEos 3.2 (monomer diameter × √2). (C) Ratios of mEos 3.2 and mEos2 diffusion coefficients plotted against anchor radius. The same three models are represented here as in panel B.

All anchors conjugated to mEos2 produce distributions of $D_{SM}$ that are consistent with a single population of Brownian diffusers with the exception of A-TM, which retains two distinct mobile populations each consistent with Brownian diffusion. This observation suggests that the mEos2 fusion proteins are a single species and not a heterogeneous array of oligomers. This is consistent with previous observations of mEos2

oligomers in solution with an affinity of close to 50 μM obtained by fitting an exponential to measured fractions of monomer to oligomer ratios at different concentrations (Zhang et al., 2012). If we assume that membrane tethering confines the protein to occupy a 1 nm shell adjacent to the membrane, then this corresponds to a surface density of 30 proteins/$\mu m^2$, which is lower than is typically observed in most transient over-expression measurements (James et al., 2006; Mercier et al., 2002; Ramsay et al., 2002). Alternatively, it is possible that different oligomeric species are present, but exchange between states on a time scale that is fast compared to a typical trajectory. We anticipate that additional constraints on the orientation of membrane anchored probes will limit oligomers to only dimers, since the tetrameric crystal structure of mEos2 (Zhang et al., 2012, 2011) shows a dimer of antiparallel dimers that are unlikely to form in a two dimensional plane.

Figure 3-11 *B* shows the radial dependence of anchor diffusion including results from anchors conjugated to mEos2. This plot includes the assumption that mEos2 conjugated anchors exist as a single population of dimers with effective radius √2 times larger than the monomeric mEos3.2 species. Again we observe significant scatter in $D_{MP}$ values obtained for the different anchor species, but retain the general trend that smaller anchors exhibit greater radial dependence on their mobility, while the diffusion coefficient of larger anchors vary only weakly with radius.

In order to better isolate the radial dependence of anchor mobility from other factors that determined diffusion coefficients of these constructs, we present a ratio of $D_{MP}$ values determined for mEos3.2 and mEos2 conjugated species in Figure 3-11 *C*. We find that this ratio of diffusion coefficients follows a smoothly varying curve and does not

exhibit the scatter observed in plots of $D_{MP}$ vs. r. One possible explanation for this observation is that the contributions to diffusion that depend on factors such as crowding or actin corralling that act to reduce diffusion by a constant pre-factor that does not depend on anchor radius at the time-scales investigated. By taking a ratio of the monomeric and presumed dimeric versions of these proteins, this pre-factor cancels, making it possible to more directly compare constructs. Even if this interpretation is not correct, our results indicate that dimerization more significantly affects the mobility of small anchors than it does large ones when probed at these time and distance scales.

It appears that the observed ratio of diffusion coefficients distinguishes between functional forms of radial dependence of diffusion within the hopping regime at small radii. The observed radial dependence of this ratio vs. radius monotonically decreases with increasing radius, as is expected when D diverges at small r, but not when D varies as a Gaussian function as is predicted from the approximated free area model function used here. Further experiments are needed to clearly distinguish possible models because several assumptions contribute to this conclusion but are not easily verified. For example, it is possible that dimerization does not simply increase radius by the same factor for all constructs. Also, we cannot rule out the alternative interpretation that larger proteins are less affected by mEos2 simply because geometrical or other constraints prevent dimerization.

Dimerization commonly occurs within membrane proteins. For some, like most receptor tyrosine kinases, dimerization is an obligatory step in activation (Weiss and Schlessinger, 1998). Furthermore, G protein-coupled receptors (GPCR) such as $\beta_2$AR are well known to oligomerize, though the reasons for this are unknown except for class C

GPCRs (Gurevich and Gurevich, 2008). Diffusion-limited reactions are necessarily sensitive to rates of reactant diffusion(Axelrod, 1983; Emeis and Fehder, 1970). It is tempting to speculate that dimerization may have evolved as a way to modulate the rate of such reactions or other processes that are diffusion dependent, such as maintenance of polarity (Otsuji et al., 2007). Our results suggest that single transmembrane or lipid-anchored proteins, whose diffusions are reduced up to 40% by dimerization, could modulate diffusion in this way. In contrast, we do not expect that dimerization of GPCRs would lead to changes in the rates of diffusion limited reactions.

**Temperature dependence of anchor mobility**

We find that the mobility of plasma membrane anchors depends dramatically on temperature. This is apparent when comparing distributions of $D_{SM}$ obtained from a single HeLa cell expressing B-TM mEos3.2 and imaged at different temperatures, as shown in Figure 3-12 *A*. Overall we observe that histograms of $D_{SM}$ shift to lower values at lower temperatures, but the shape of the distributions do not change outside of a slight increase in the number of immobile trajectories observed at the lowest temperature investigated (23.5°C). Since data for this example was acquired for this lowest temperature first, it is possible that immobile trajectories are not observed at higher temperatures simply because this population was depleted early in the measurement and not replaced.

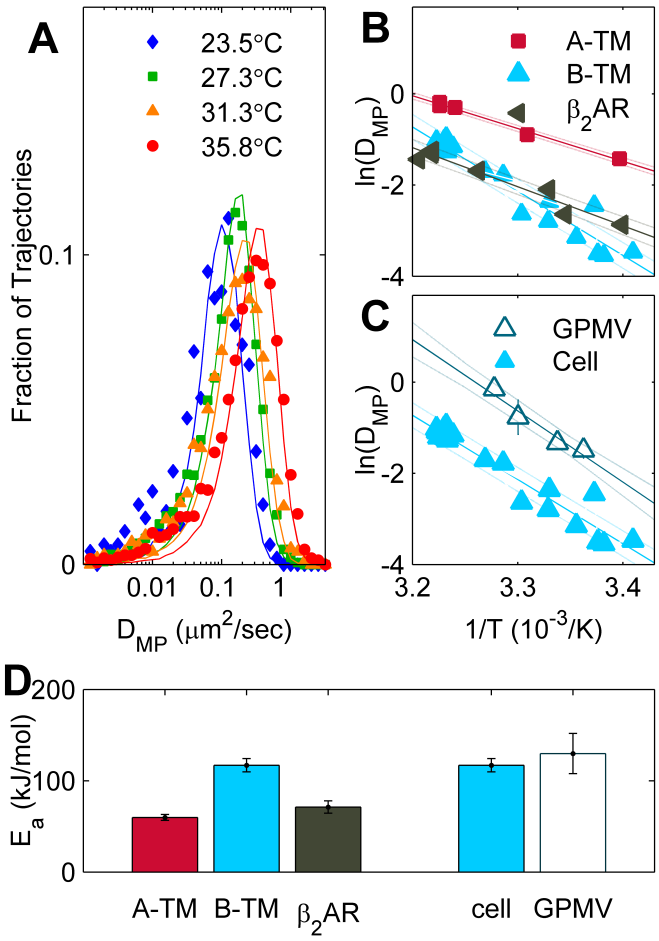


Figure 3-12 (A) $D_{SM}$ histograms from a single cell expressing B-TM mEos 3.2 recorded at four temperatures. Diffusion coefficients $D_{MP}$ are determined for each condition. (B) An Arrhenius plot shows the exponential temperature dependence of three mEos 3.2 fusion proteins. The apparent activation energies ($E_a$) in intact cells are 59 ± 6 kJ mol$^{-1}$ for A-TM, 117 ± 7 kJ mol$^{-1}$ for B-TM, 75 ± 17 kJ mol$^{-1}$for $\beta_2$AR. (C) An Arrhenius plot of the same B-TM data is plotted in panel B in addition to diffusion recordings from giant plasma membrane vesicles (GPMV) extracted from CHO cells expressing the same construct. The GPMV yields apparent activation energy of 130 ± 22 kJ mol$^{-1}$. For both B and C Error bars represent fit errors as determined by bootstrapping for the y-axis and experimental temperature error on the x-axis. Confidence intervals are plotted alongside the linear fits. (D) The bar chart shows the apparent activation energy for each protein.

We find that $D_{MP}$ for all three transmembrane anchors exhibit Arrhenius behavior as depicted in Figure 3-12 *B,* indicating that diffusion occurs through a thermally activated process. The slope of the lines in Figure 3-12 *B* yield effective activation energy of this barrier ($E_a$). $E_a$ for the faster population of A-TM is 59±6 kJ mol$^{-1}$, 117±7 kJ mol$^{-1}$ for B-TM, and 75±18 kJ mol$^{-1}$ for $\beta_2$AR, where errors are extracted directly from the

linear fit. These measurements of $E_a$ are in good agreement or significantly higher than similar measurements in intact cells. A recent study of the transferrin receptor reported an activation energy of 134 kJ/mol (Di Rienzo et al., 2013), whereas in A-431 cells, a FRAP study of EGFR found an $E_a$ of 25.5 kJ/mol (Hillman and Schlessinger, 1982). Previous work has also demonstrated that lipids and other small molecules in model membranes show thermally activated diffusion, with apparent $E_a$ in the range of 25-40 kJ/mol (Gaede and Gawrisch, 2003; Lee et al., 2003; Liu et al., 1997; Wassall, 1996; Wu et al., 1978). Currently it is unclear what leads to the range of $E_a$ values determined for different components in cell and model membranes. Based on our current study, we conclude that it is unlikely that anchor radius alone determines $E_a$ in cells since we do not observe a monotonic trend in $E_a$ as the size of the anchor is increased from a single helix (A-TM) to a helical dimer (B-TM) to a 7 pass transmembrane protein ($\beta_2$AR).

Recent work has implicated active ATP-dependent processes in contributing to the temperature-dependent diffusion of macromolecules (Sunyer et al., 2009; Weber et al., 2012). One recent study implicated cytoskeleton as the free-energy barriers to diffusion, and suggested that temperature dependence of diffusion is related to the energy of cytoskeletal remodeling (Di Rienzo et al., 2013). To investigate the role of cytoskeleton and active processes, we quantified the diffusion of B-TM in isolated giant plasma membrane vesicles (GPMVs) which contain no cytoskeletal components and are depleted of ATP (Tank et al., 1982), as shown in Figure 3-12 *C*. We find that B-TM probes are more mobile in GPMVs by roughly a factor of 5 and the temperature-dependence retains its Arrhenius behavior. The apparent $E_a$ is $130 \pm 22$ kJ $mol^{-1}$ and is indistinguishable within error from that measured in intact cells. Based on this

observation, we conclude that the activation energy of diffusion is not dependent on cytoskeleton corrals or active cellular processes. Instead, it appears that the temperature dependence of diffusion arises from the temperature dependences of membrane physical properties such as viscosity or factors that contribute to hopping behaviors on short time and distance scales.

## Conclusion

The present study introduces a method of analysis for single particle tracking with short trajectories by comparison to simulations of Brownian trajectories. We demonstrate the use of this tool to identify heterogeneity in the otherwise broad distributions of single molecule diffusion parameters, and to quantify population diffusion coefficients. We find that under hypoxic conditions, the diffusion of membrane proteins is consistent cell-to-cell, for the most part homogenous, and unconfined. Furthermore we show that in intact cells, diffusion is highly temperature-dependent for all proteins, and size-dependent for smaller proteins. While our experimental conditions resulted in simple diffusion profiles, the method presented deals well with multiple populations of the same diffuser whether immobile or mobile, and is used in Chapter 4 to aid in interpreting more complex diffusion profiles present under different experimental conditions.

As to one of our central questions of how palmitoylation affects lateral diffusion of transmembrane proteins, we come to the following conclusions. First, we see that in intact cells, just as in model membranes, the relationship between anchor size and diffusion is more size-dependent for smaller anchors. Based on this finding we hypothesize that changes in size with palmitoylation may slow lateral diffusion, but the

extent depends on size of the transmembrane domain. E.g. single transmembrane proteins with three palmitate moieties will be more affected than a singly palmitoylated seven transmembrane protein. Similarly if palmitoylation causes dimerization, then based on these results we would expect that small anchors would be slowed more than large anchors. Secondly, in this chapter we characterize the cell-to-cell variability of lateral diffusion, which under careful temperature control is approximately 10% (E.g. B-TM which was $0.40 \pm 0.04$ standard deviation determined from 10 cells). This gives an indication of the effective detection limit of our system and underscores the necessity for high statistics to overcome cell-to-cell variability when investigating small differences between conditions.

## Works Cited


Almeida, P.F.F., and Vaz, W.L.C. (1995). Lateral Diffusion in Membranes. In Structure and Dynamics of Membranes, R. (Reinhard) Lipowsky, and E. (Erich). Sackmann, eds. (Amsterdam ; New York :: Elsevier Science), pp. 305–357.

Axelrod, D. (1983). Lateral motion of membrane proteins and biological function. J Membr Biol *75*, 1–10.

Balcom, B.J., and Petersen, N.O. (1993). Lateral diffusion in model membranes is independent of the size of the hydrophobic region of molecules. Biophys J *65*, 630–637.

Betzig, E., Patterson, G.H., Sougrat, R., Lindwasser, O.W., Olenych, S., Bonifacino, J.S., Davidson, M.W., Lippincott-Schwartz, J., and Hess, H.F. (2006). Imaging intracellular fluorescent proteins at nanometer resolution. Science *313*, 1642–1645.

Celedón, G., González, G., Sotomayor, C.P., and Behn, C. (1998). Membrane lipid diffusion and band 3 protein changes in human erythrocytes due to acute hypobaric hypoxia. Am. J. Physiol.-Cell Physiol. *275*, C1429–C1431.

Chaudhuri, A., Bhattacharya, B., Gowrishankar, K., Mayor, S., and Rao, M. (2011). Spatiotemporal regulation of chemical reactions by active cytoskeletal remodeling. Proc. Natl. Acad. Sci. *108*, 14825–14830.

Cicuta, P., Keller, S.L., and Veatch, S.L. (2007). Diffusion of liquid domains in lipid bilayer membranes. J Phys Chem B *111*, 3328–3331.

Clausen, M.P., and Lagerholm, B.C. (2011). The probe rules in single particle tracking. Curr Protein Pept Sci *12*, 699–713.

Cohen, M.H., and Turnbull, D. (1959). Molecular transport in liquids and glasses. J. Chem. Phys. *31*, 1164.

Eggeling, C., Ringemann, C., Medda, R., Schwarzmann, G., Sandhoff, K., Polyakova, S., Belov, V.N., Hein, B., von Middendorff, C., Schonle, A., et al. (2009). Direct observation of the nanoscale dynamics of membrane lipids in a living cell. Nature *457*, 1159–1162.

Emeis, C.A., and Fehder, P.L. (1970). Microscopic Mechanism for Diffusion and Rates of Diffusion-Controlled Reaction in Simple Liquid Solvents. J. Am. Chem. Soc. *92*, 2246–+.

Endesfelder, U., Malkusch, S., Flottmann, B., Mondry, J., Liguzinski, P., Verveer, P.J., and Heilemann, M. (2011). Chemically induced photoswitching of fluorescent probes--a general concept for super-resolution microscopy. Molecules *16*, 3106–3118.

Evans, E., and Sackmann, E. (1988). Translational and Rotational Drag Coefficients for a Disk Moving in a Liquid Membrane-Associated with a Rigid Substrate. J. Fluid Mech. *194*, 553–561.

Gaede, H.C., and Gawrisch, K. (2003). Lateral diffusion rates of lipid, water, and a hydrophobic drug in a multilamellar liposome. Biophys J *85*, 1734–1740.

Galla, H.-J., Hartmann, W., Theilen, U., and Sackmann, E. (1979). On two-dimensional passive random walk in lipid bilayers and fluid pathways in biomembranes. J. Membr. Biol. *48*, 215–236.

Gambin, Y., Lopez-Esparza, R., Reffay, M., Sierecki, E., Gov, N.S., Genest, M., Hodges, R.S., and Urbach, W. (2006). Lateral mobility of proteins in liquid membranes revisited. Proc. Natl. Acad. Sci. U. S. A. *103*, 2098–2102.

Gibson, T.J., Seiler, M., and Veitia, R.A. (2013). The transience of transient overexpression. Nat. Methods *10*, 715–721.

Guigas, G., and Weiss, M. (2006). Size-dependent diffusion of membrane inclusions. Biophys J *91*, 2393–2398.

Gurevich, V.V., and Gurevich, E.V. (2008). How and why do GPCRs dimerize? Trends Pharmacol. Sci. *29*, 234–240.

Harb, F., Sarkis, J., Ferte, N., and Tinland, B. (2012). Beyond Saffman-Delbruck approximation: a new regime for 2D diffusion of alpha-hemolysin complexes in supported lipid bilayer. Eur Phys J E Soft Matter *35*, 118.

Hebert, B., Costantino, S., and Wiseman, P.W. (2005). Spatiotemporal Image Correlation Spectroscopy (STICS) Theory, Verification, and Application to Protein Velocity Mapping in Living CHO Cells. Biophys. J. *88*, 3601–3614.

Hess, S.T., Girirajan, T.P., and Mason, M.D. (2006). Ultra-high resolution imaging by fluorescence photoactivation localization microscopy. Biophys J *91*, 4258–4272.

Hillman, G.M., and Schlessinger, J. (1982). Lateral diffusion of epidermal growth factor complexed to its surface receptors does not account for the thermal sensitivity of patch formation and endocytosis. Biochemistry (Mosc.) *21*, 1667–1672.

Hofmann, M., Eggeling, C., Jakobs, S., and Hell, S.W. (2005). Breaking the diffraction barrier in fluorescence microscopy at low light intensities by using reversibly photoswitchable proteins. Proc. Natl. Acad. Sci. U. S. A. *102*, 17565–17569.

Honerkamp-Smith, A.R., Machta, B.B., and Keller, S.L. (2012). Experimental observations of dynamic critical phenomena in a lipid membrane. Phys. Rev. Lett. *108*, 265702.

Hughes, B.D., Pailthorpe, B.A., White, L.R., and Sawyer, W.H. (1982). Extraction of membrane microviscosity from translational and rotational diffusion coefficients. Biophys J *37*, 673–676.

James, J.R., Oliveira, M.I., Carmo, A.M., Iaboni, A., and Davis, S.J. (2006). A rigorous experimental framework for detecting protein oligomerization using bioluminescence resonance energy transfer. Nat Methods *3*, 1001–1006.

Kasai, R.S., Suzuki, K.G., Prossnitz, E.R., Koyama-Honda, I., Nakada, C., Fujiwara, T.K., and Kusumi, A. (2011). Full characterization of GPCR monomer-dimer dynamic equilibrium by single molecule imaging. J Cell Biol *192*, 463–480.

Kenworthy, A.K., Nichols, B.J., Remmert, C.L., Hendrix, G.M., Kumar, M., Zimmerberg, J., and Lippincott-Schwartz, J. (2004). Dynamics of putative raft-associated proteins at the cell surface. J Cell Biol *165*, 735–746.

Kusumi, A., Sako, Y., and Yamamoto, M. (1993). Confined Lateral Diffusion of Membrane Receptors as Studied by Single Particle Tracking (Nanovid Microscopy). Effects of Calcium-induced Differentiation in Cultured Epithelial Cells. Biophys. J. *65*, 2021–2040.

Kusumi, A., Nakada, C., Ritchie, K., Murase, K., Suzuki, K., Murakoshi, H., Kasai, R.S., Kondo, J., and Fujiwara, T. (2005). Paradigm shift of the plasma membrane concept from the two-dimensional continuum fluid to the partitioned fluid: high-speed single-molecule tracking of membrane molecules. Annu Rev Biophys Biomol Struct *34*, 351–378.

Lee, C.C., Revington, M., Dunn, S.D., and Petersen, N.O. (2003). The lateral diffusion of selectively aggregated peptides in giant unilamellar vesicles. Biophys J *84*, 1756–1764.

Levental, I., Grzybek, M., and Simons, K. (2010a). Greasing their way: lipid modifications determine protein association with membrane rafts. Biochemistry (Mosc.) *49*, 6305–6316.

Levental, I., Lingwood, D., Grzybek, M., Coskun, U., and Simons, K. (2010b). Palmitoylation regulates raft affinity for the majority of integral raft proteins. Proc Natl Acad Sci U A *107*, 22050–22054.

Van de Linde, S., Heilemann, M., and Sauer, M. (2012). Live-Cell Super-Resolution Imaging with Synthetic Fluorophores. Annu. Rev. Phys. Chem. *63*, 519–540.

Liu, C., Paprica, A., and Petersen, N.O. (1997). Effects of size of macrocyclic polyamides on their rate of diffusion in model membranes. Biophys J *73*, 2580–2587.

Lommerse, P.H., Vastenhoud, K., Pirinen, N.J., Magee, A.I., Spaink, H.P., and Schmidt, T. (2006). Single-molecule diffusion reveals similar mobility for the Lck, H-ras, and K-ras membrane anchors. Biophys J *91*, 1090–1097.

Manley, S., Gillette, J.M., Patterson, G.H., Shroff, H., Hess, H.F., Betzig, E., and Lippincott-Schwartz, J. (2008). High-density mapping of single-molecule trajectories with photoactivated localization microscopy. Nat. Methods *5*, 155–157.

McKinney, S.A., Murphy, C.S., Hazelwood, K.L., Davidson, M.W., and Looger, L.L. (2009). A bright and photostable photoconvertible fluorescent protein. Nat Methods *6*, 131–133.

Meder, D., Moreno, M.J., Verkade, P., Vaz, W.L.C., and Simons, K. (2006). Phase coexistence and connectivity in the apical membrane of polarized epithelial cells. Proc. Natl. Acad. Sci. U. S. A. *103*, 329–334.

Mercier, J.F., Salahpour, A., Angers, S., Breit, A., and Bouvier, M. (2002). Quantitative assessment of beta 1- and beta 2-adrenergic receptor homo- and heterodimerization by bioluminescence resonance energy transfer. J Biol Chem *277*, 44925–44931.

Mittal, R., and Bruchez, M.P. (2011). Biotin-4-fluorescein based fluorescence quenching assay for determination of biotin binding capacity of streptavidin conjugated quantum dots. Bioconjug Chem *22*, 362–368.

Nir, S., and Stein, W.D. (1971). Two Modes of Diffusion in Liquids. J. Chem. Phys. *55*, 1598.

Otsuji, M., Ishihara, S., Co, C., Kaibuchi, K., Mochizuki, A., and Kuroda, S. (2007). A mass conserved reaction-diffusion system captures properties of cell polarity. Plos Comput. Biol. *3*, 1040–1054.

Paller, M.S. (1993). Lateral diffusion of lipids in renal cells: effects of hypoxia and reoxygenation and role of cytoskeleton. Am. J. Physiol. *264*, C201–208.

Petrov, E.P., and Schwille, P. (2008). Translational diffusion in lipid membranes beyond the Saffman-Delbruck approximation. Biophys J *94*, L41–3.

Pyenta, P.S., Holowka, D., and Baird, B. (2001). Cross-correlation analysis of inner-leaflet-anchored green fluorescent protein co-redistributed with IgE receptors and outer leaflet lipid raft components. Biophys J *80*, 2120–2132.

Qian, H., Sheetz, M.P., and Elson, E.L. (1991). Single particle tracking. Analysis of diffusion and flow in two-dimensional systems. Biophys J *60*, 910–921.

Ramadurai, S., Holt, A., Krasnikov, V., van den Bogaart, G., Killian, J.A., and Poolman, B. (2009). Lateral diffusion of membrane proteins. J Am Chem Soc *131*, 12650–12656.

Ramsay, D., Kellett, E., McVey, M., Rees, S., and Milligan, G. (2002). Homo- and hetero-oligomeric interactions between G-protein-coupled receptors in living cells monitored by two variants of bioluminescence resonance energy transfer (BRET): hetero-oligomers between receptor subtypes form more efficiently than between less closely related sequences. Biochem J *365*, 429–440.

Di Rienzo, C., Gratton, E., Beltram, F., and Cardarelli, F. (2013). Fast spatiotemporal correlation spectroscopy to determine protein lateral diffusion laws in live cell membranes. Proc. Natl. Acad. Sci. *110*, 12307–12312.

Saffman, P.G., and Delbrück, M. (1975). Brownian motion in biological membranes. Proc Natl Acad Sci U A *72*, 3111–3113.

Sahl, S.J., Leutenegger, M., Hilbert, M., Hell, S.W., and Eggeling, C. (2010). Fast molecular tracking maps nanoscale dynamics of plasma membrane lipids. Proc. Natl. Acad. Sci. *107*, 6829–6834.

Saxton, M.J. (1995). Single-particle tracking: effects of corrals. Biophys J *69*, 389–398.

Saxton, M.J. (1997). Single-particle tracking: the distribution of diffusion coefficients. Biophys J *72*, 1744–1753.

Saxton, M.J. (2012). Wanted: a positive control for anomalous subdiffusion. Biophys J *103*, 2411–2422.

Scolari, S., Engel, S., Krebs, N., Plazzo, A.P., De Almeida, R.F., Prieto, M., Veit, M., and Herrmann, A. (2009). Lateral distribution of the transmembrane domain of influenza virus hemagglutinin revealed by time-resolved fluorescence imaging. J Biol Chem *284*, 15708–15716.

Semrau, S., and Schmidt, T. (2007). Particle Image Correlation Spectroscopy (PICS): Retrieving Nanometer-Scale Correlations from High-Density Single-Molecule Position Data. Biophys. J. *92*, 613–621.

Shelby, S.A., Holowka, D.A., Baird, B.A., and Veatch, S.L. (2013). Distinct stages of stimulated FcεRI receptor clustering and immobilization are identified through super-resolution imaging. Biophys. J. *(in press)*.

Sunyer, R., Ritort, F., Farré, R., and Navajas, D. (2009). Thermal activation and ATP dependence of the cytoskeleton remodeling dynamics. Phys. Rev. E *79*.

Suzuki, K.G.N., Kasai, R.S., Hirosawa, K.M., Nemoto, Y.L., Ishibashi, M., Miwa, Y., Fujiwara, T.K., and Kusumi, A. (2012). Transient GPI-anchored protein homodimers are units for raft organization and function. Nat. Chem. Biol. *8*, 774–783.

Tank, D.W., Wu, E.S., and Webb, W.W. (1982). Enhanced molecular diffusibility in muscle membrane blebs: release of lateral constraints. J Cell Biol *92*, 207–212.

Thompson, A.R., Hoeprich, G.J., and Berger, C.L. (2013). Single-molecule motility: statistical analysis and the effects of track length on quantification of processive motion. Biophys J *104*, 2651–2661.

Valentine, C.D., and Haggie, P.M. (2011). Confinement of beta(1)- and beta(2)-adrenergic receptors in the plasma membrane of cardiomyocyte-like H9c2 cells is mediated by selective interactions with PDZ domain and A-kinase anchoring proteins but not caveolae. Mol Biol Cell *22*, 2970–2982.

Vaz, W.L., Criado, M., Madeira, V.M., Schoellmann, G., and Jovin, T.M. (1982). Size dependence of the translational diffusion of large integral membrane proteins in liquid-crystalline phase lipid bilayers. A study using fluorescence recovery after photobleaching. Biochemistry (Mosc.) *21*, 5608–5612.

Vaz, W.L.C., Goodsaid-Zalduondo, F., and Jacobson, K. (1984). Lateral diffusion of lipids and proteins in bilayer membranes. FEBS Lett. *174*, 199–207.

Vaz, W.L.C., Clegg, R.M., and Hallmann, D. (1985). Translational diffusion of lipids in liquid crystalline phase phosphatidylcholine multibilayers. A comparison of experiment with theory. Biochemistry (Mosc.) *24*, 781–786.

Wassall, S.R. (1996). Pulsed field gradient-spin echo NMR studies of water diffusion in a phospholipid model membrane. Biophys J *71*, 2724–2732.

Waterfall, J.J., Casey, F.P., Gutenkunst, R.N., Brown, K.S., Myers, C.R., Brouwer, P.W., Elser, V., and Sethna, J.P. (2006). Sloppy-Model Universality Class and the Vandermonde Matrix. Phys. Rev. Lett. *97*, 150601.

Weber, S.C., Spakowitz, A.J., and Theriot, J.A. (2012). Nonthermal ATP-dependent fluctuations contribute to the in vivo motion of chromosomal loci. Proc Natl Acad Sci U A *109*, 7338–7343.

Weiss, A., and Schlessinger, J. (1998). Switching signals on or off by receptor dimerization. Cell *94*, 277–280.

Wieser, S., and Schutz, G.J. (2008). Tracking single molecules in the live cell plasma membrane-Do's and Don't's. Methods *46*, 131–140.

Wu, E.S., Jacobson, K., Szoka, F., and Portis, A. (1978). Lateral diffusion of a hydrophobic peptide, N-4-nitrobenz-2-oxa-1,3-diazole gramicidin S, in phospholipid multibilayers. Biochemistry (Mosc.) *17*, 5543–5550.

Zhang, M., Chang, H., Zhang, Y., Yu, J., Wu, L., Ji, W., Chen, J., Liu, B., Lu, J., Liu, Y., et al. (2012). Rational design of true monomeric and bright photoactivatable fluorescent proteins. Nat Methods *9*, 727–729.

Zhang, M.S., Wu, L.J., Xu, P.Y., Liu, Y.F., and Xu, T. (2011). mEos2 Fluorescent Protein-Green Form.

# Chapter 4

# Hypoxic buffer conditions result in fast and homogenous diffusion

## Introduction

In Chapter 3, the imaging buffer used for live cell single particle tracking included reducing agent and an enzymatic oxygen-scavenging system. These photoprotective hypoxic buffer conditions enable reproducible diffusion observations and improved imaging of mEos proteins. As in Figure 3-3, with the omission of the oxygen-scavenging system, lateral diffusion is slowed and heterogeneous. In the following chapter we explore the lateral diffusion of the same panel of model membrane proteins under normoxic conditions in HeLa cells and compare them to our previous findings.

Hypoxia occurs in a variety of conditions such as in wounds (Chang and Goodson, 1983), traumatic injury, diabetes, coronary heart disease, and stroke (Carreau et al., 2011). Other conditions where hypoxia occurs include mountain sickness, physical exercise, pregnancy, ageing, inflammation and respiratory failures (Behn et al., 2007). Most notably, solid tumors are hypoxic (Giaccia et al., 2004). Hypoxia correlates with aggression, treatment resistance, and ultimately worse prognoses for patients of many cancers, including head-and-neck squamous carcinoma patients (Giaccia et al., 2004; Hoogsteen et al., 2012). This may be due to the enhanced migratory capacity of cancer

cells, activation of EGFR, which can occur by hypoxic stress (Wang and Schneider, 2010), or upregulation of harmful genes due to oxygen-responsive transcriptional regulation (Ivan et al., 2001; Ohh et al., 2000).

The partial pressure of oxygen ($PO_2$) is 160 mmHg in the atmosphere, 10-20 mmHg in cells and 30-79 mmHg in specialized organs such as liver, brain, lungs, and kidney. $PO_2$ levels in solid tumors measure less than 2.5 mmHg in severe hypoxia. A critical point is reached at 8 mmHg $PO_2$ (Carreau et al., 2011), as below this threshold cells exhibit detrimental effects of low oxygen such as ATP depletion, intracellular acidosis and apoptosis. Even at oxygen concentrations above this threshold, cells respond to decreasing oxygen conditions by reducing consumption of ATP, by halting protein production, ion pumping, and other energetically expensive processes (Heerlein et al., 2005). Consequently, the effects of acute hypoxia are reversible to an extent, but less so after chronic hypoxia (Lemasters et al., 1983).

Contrary to what the name might suggest, hypoxic conditions can actually increase the amount of reactive oxygen species (ROS) in cells due to ROS release from mitochondria under hypoxic stress (Giaccia et al., 2004). Hypoxic conditions can make cells susceptible to oxidative stress from ROS including lipid peroxidation (Celedón et al., 1998; de Groot and Noll, 1987). Lipid peroxidation is a chain reaction initiated by ROS such as hydroxyl radicals that react particularly well with unsaturated lipids. The resulting lipid peroxyl radicals can combine with each other, attack membrane proteins, or extract hydrogen from adjacent fatty acids, thus propagating the peroxidation chain reaction (Halliwell and Chirico, 1993; Halliwell and Cross, 1994). These chain reactions typically quench only with the application of antioxidants, which are maintained by a

healthy cell as a part of its antioxidant defenses against ROS. In membranes, $\alpha$-tocopherol, a type of vitamin E, is one of the most important such antioxidants (Halliwell and Chirico, 1993). Lipid peroxidation itself is associated with a number of pathologies such as inflammation, muscular dystrophy, and ischemia reperfusion injury (de Groot and Noll, 1987).

Lateral diffusion is faster under hypoxic, or post-hypoxic reoxygenated circumstances. The increased diffusion may be due to change in membrane fluidity which increases with peroxidation of lipids (Behn et al., 2007; Celedón et al., 1998; Paller, 1993). Additionally, cytoskeletal dysfunction is proposed to be responsible for the hypoxic phenotype, as stabilization of the cytoskeleton with phallicidin eliminates the hypoxic effect on lateral diffusion in renal cells (Paller, 1993). The diffusion profile observed in our experiments is likely representative of this state, as diffusion is both homogeneous and faster in the presence of the oxygen-scavenging buffer.

The choice to image live cells in the particular hypoxic imaging buffer used in Chapter 3 was based on two main reasons: photo-protection and maintaining physiological pH. Phototoxicity is mediated via multiple mechanisms. Photons from illumination with short wavelengths of light, ranging from UV to blue can be absorbed directly by proteins and DNA, resulting in excitation and subsequent chemical reactions. Alternatively, endogenous or exogenous chemicals such as drugs or organic fluorophores (Hoebe et al., 2007) can be excited to form free radicals or singlet oxygen, which in turn react with cellular components. Ultimately, DNA becomes lesioned or reactive and proteins aggregate, and the cell descends into dysfunction and death (Godley et al.,

2005). In our experiments, phototoxicity was morphologically apparent due to blebbing, or the formation of bulging membrane protrusions.

Serendipitously, blebbing did not occur in the presence of hypoxic buffer. This buffer was originally developed for use with organic fluorophores (Rust et al., 2006) and is required to maintain the majority of fluorophores in the dark state and increase their photo-stability. An enzymatic oxygen-scavenging system, composed of glucose oxidase, catalase and glucose are included, in addition to reducing agent. Glucose oxidase depletes oxygen from the sample by reacting it with glucose to form gluconic acid and hydrogen peroxide. Depleting oxygen reduces the occurrence of other damaging reactive oxygen species that bleach organic fluorophores. Catalase then converts $H_2O_2$ to water and $½O_2$ to eliminate the harmful effects of the peroxide. Hydrogen peroxide is tolerated at low concentrations, and in fact is a signaling molecule in healthy cells (Miller et al., 2005), but is damaging at higher concentrations. Reduced glutathione itself also scavenges free radicals directly from the solution. Oxygen scavenging buffer is compatible with mEos proteins and was previously determined to be compatible with live cell imaging (Bates et al., 2007; Huang et al., 2008). Furthermore, the reducing agent induces cycling between a dark and fluorescent state of mEos proteins, increasing the possible number of trajectories from each protein (Endesfelder et al., 2011).

The presence of the oxygen-scavenging system acidifies the imaging buffer over time due to generation of gluconic acid (Shi et al., 2010). Acidification is unfavorable for the dual reason that cells remain viable only in a narrow pH range (pH 6-8) and the mEos proteins begins to blink rapidly at pH<6.5. The latter results in shorter trajectories and poorer imaging outcomes, but provides a useful indicator during imaging that the pH is

drifting out of the favorable range for cells. To extend the experimental time window we increased the buffering component of the imaging buffer by increasing buffer as in Shi *et al* (Shi et al., 2010). This is how we came to use the particular variant of the hypoxic imaging buffer we employed and refer to as 'hypoxic' imaging buffer in this chapter. (see Materials and Methods). We find that in this imaging buffer, continuous imaging for >20 minutes yields consistent and stable results.

In Chapter 3, we introduced a method for analysis of short tracks and quantification of diffusion. In oxidatively stressed cells, we saw homogenous diffusion, consistent with Brownian motion. In the current chapter we seek to explore lateral diffusion of the same panel of model membrane proteins under normoxic imaging conditions. It should be noted that 'HEPES-buffered' and 'normoxic' imaging conditions are used interchangeably in the following chapter to contrast with hypoxic conditions. However, strictly speaking, atmospheric conditions are not 'normoxic' for cells either, as the close to 160 mmHg $PO_2$ available to cells under atmospheric conditions are higher than what occurs in cells (Carreau et al., 2011). The goals for this chapter are the following. The first is to characterize the differences in diffusion profiles under normoxic imaging conditions and compare to hypoxic diffusion. The second is to determine how the Brownian simulation-coupled method holds up under apparently more complex diffusion profiles. The final goal is to ascertain which experimental conditions are most suitable to test the effect of palmitoylation on lateral diffusion.

## Results and Discussion

### Limiting light exposure prevents cell phototoxicity

HEPES-buffered imaging solution is a popular bicarbonate-independent solution for extended imaging of live cells. This buffer is amenable to imaging proteins. However, exposure to 561 nm light results in phototoxicity in the form of blebbing in cells under these buffer conditions. Cells expressing $\beta_2$AR mEos2 are shown in Figure 4-1 illuminated under white light. Blebbing is observed within twenty minutes of illumination under the same laser intensity as was used during most experiments (15-30 mW of 561 nm light). Surrounding cells in the same samples did not show blebbing at the end of this time period, indicating that illumination was necessary to induce this morphologic change.

Accounts differ as to why blebbing occurs in HEPES imaging conditions. HEPES generates the toxic reactive oxygen species hydrogen peroxide in response to light (Dailey et al., 2013; Lepe-Zuniga et al., 1987). Some accounts attribute the toxicity to absence of bicarbonate in the HEPES buffer (Dailey et al., 2013). Our data suggest that phototoxicity is likely unrelated to HEPES but the direct consequence of absorbing light. Cells in other imaging buffers produced similar phenotypes in response to the light exposure.

The literature approaches the challenge of maintaining healthy cells using a handful of imaging media that could be used as HEPES alternatives. First is the use of various growth media such as Ham's FK 12 DMEM or RPMI, which are free of phenol red. The phenol red pH indicator is fluorescent and can interfere with sensitive fluorescent imaging applications such as single molecule TIRF by increasing background

fluorescence (Dailey et al., 2013). Growth media such as Ham's FK 12, DMEM and RPMI, typically contain bicarbonate buffer and require constant application of 5-7% carbon dioxide to the air surrounding the sample during imaging to maintain the pH. Alternatively the media must be supplemented with HEPES to avoid pH drift within five minutes (Frigault et al., 2009). We found that imaging in Ham's FK12 DMEM media did not result in decreased blebbing compared to HEPES conditions.

Alternatively, phosphate buffered saline (PBS) can be used for short-term applications, up to 30 minutes, but does not support function or growth (Dailey et al., 2013). Due to the absence of calcium, PBS may also cause cytoskeletal retreat (Paller, 1993). A PBS buffer with supplemented calcium and magnesium has also been used, though in our experiments this buffer (PBS +) is no more photo-protective than HEPES.

Having found no obvious alternative to the HEPES-buffered imaging solution, further experiments were performed in HEPES buffer, taking care to limit the potential for phototoxicity in other ways. The first measure recommended in literature is to restrict as much as possible the intensity and duration of exposure to harmful light. Specialized techniques to minimize exposure have been developed (Nishigaki et al., 2006; Hoebe et al., 2007). We minimize the exposure of the cell to 405 nm excitation (necessary for photoconversion) as well as the 495 ± 50 nm LED light used to identify expressing cells. Cells were recorded maximally for 5000 frames or about 3-5 minutes. Each sample was discarded within one hour of removing growth media. We observe blebbing in a variety of buffers, and so buffer-independent phototoxicity is likely the predominant cause of cellular distress in our system. Nonetheless, we took the precaution of adding catalase to

the medium to decompose any hydrogen peroxide that might evolve from exposing HEPES to light.

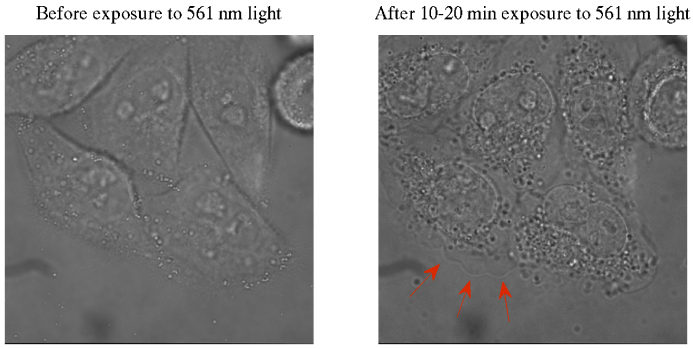


Figure 4-1 Phototoxicity manifested as blebbing. Red arrows point to membrane protrusions, or blebs that developed over the course of the cell.

As a quality control measure, care was taken to examine the morphology of the cell at the beginning and end of each experiment to assess cell health, using wide field white light. Primarily we looked for blebs, enlarged vacuoles, or cell shrinkage. To ensure that more subtle phototoxic effect on lateral diffusion has not occurred, all single molecule diffusion values from the first 1500 frames of recording were compared against those from the last 1500 frames. We performed a two-variable student's T-test to determine if the ensemble averages of early and late diffusion data can be said to come from the same mean with a 95% confidence interval. If the null hypothesis was rejected, we omitted the recording from further analysis. Approximately $1/5^{th}$ of the recordings were omitted using this test.

By point of comparison, imaging buffers used by similar studies of single particle imaging in live cells include PBS (Lommerse et al., 2006; Schutz et al., 2000), unspecified imaging buffer plus oxygen scavenging and β-mercaptoethanol (Bates et al.,

2007), PBS with 1% BSA (Clausen and Lagerholm, 2013), Dulbecco's phosphate buffered saline (Wieser et al., 2007) and phenol-red free DMEM/Ham's F12 with 10% fetal bovine serum (Johnson et al., 2011). Some do not specify their media beyond imaging buffer (Manley et al., 2008; Di Rienzo et al., 2013).

**Proteins diffuse more slowly under normoxic conditions**

In Figure 4-2, a small subset of representative long trajectories are drawn for the transmembrane domain constructs. Trajectory shapes are drastically different in HEPES buffer. They cover less ground than the same constructs in the hypoxic buffer. Subjectively, mEos 3.2 proteins appeared less bright in comparison to background in the HEPES-buffered condition, necessitating a slower acquisition rate for higher localization precision. Thus recordings in the HEPES-buffered conditions are primarily acquired at 33 frames per second (30 ms frames) rather than at 50 frames per second (20 ms frames) as in Chapter 3. Considering this, the shape differences in the trajectories are even more striking as tracks in the HEPES-buffered conditions exhibit smaller displacements in longer time intervals. Diffusion constants and α exponents are calculated from these trajectories in the same way as described in Chapter 3, and Material and Methods in order to characterize diffusion under normoxic conditions.

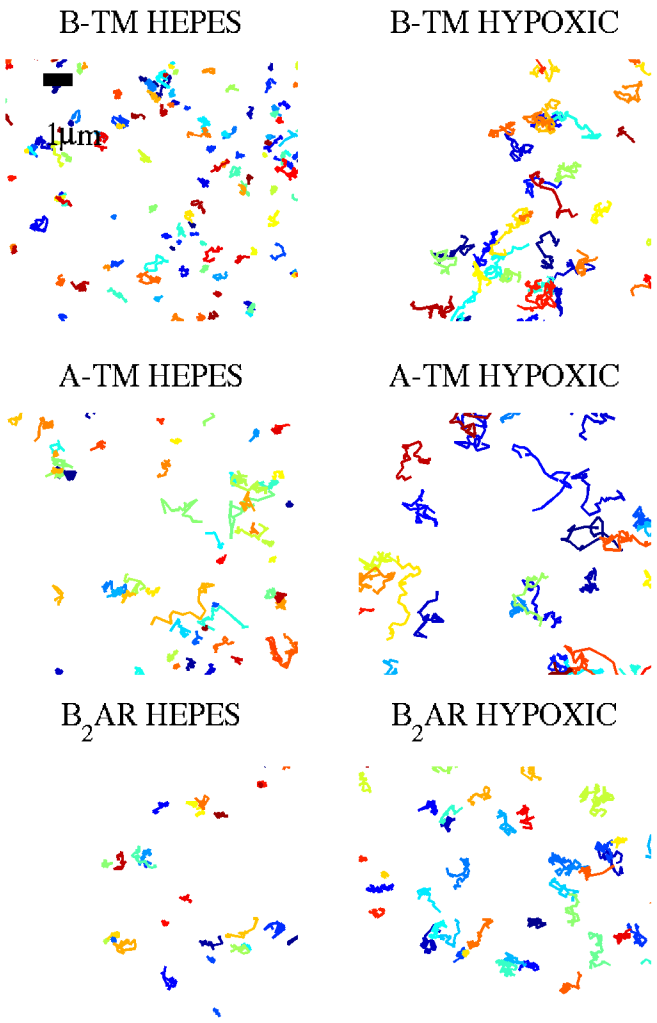


Figure 4-2 Representative long trajectories of transmembrane proteins B-TM, A-TM, and $\beta_2$AR in HEPES - buffered imaging solution and hypoxic imaging buffer. Constructs with higher diffusion constants (A-TM >B-TM>$\beta_2$AR ) cover more area, but in all cases, trajectories in the HEPES buffer cover a smaller area and appear more confined than their hypoxic counterparts.

The reason for the slower diffusion under normoxic conditions is not obvious. In one frame, even the slowest of the probes $\beta_2$AR, exhibits step sizes on the order of 120 nm. Thus the obstacles to fast diffusion observed in these experiments, are on a relatively large size scale. The heterogeneity present in the normoxic conditions, and absent in hypoxic systems, could be due to lipid phase heterogeneity, binding to other proteins, or

non-specific protein obstacles such as cytoskeleton. In HeLa cells, cytoskeletal corrals as understood by the picket fence model are on average 68 nm in size. Though they are heterogeneous, they should be too small to detect at our frame rates (Kusumi et al., 2005). Similarly, the criticality model predicts that the size of phase-heterogeneity may be dictated by the size of the cortical actin meshwork, so we will detect effects of phase-association only if diffusion is affected long range, or if critical phases are stabilized into larger fluctuations by affinity with larger protein clusters. Non-specific protein obstacles must be immobile in order to cause confinement (Saxton, 1994) which is unlikely in the absence of cytoskeletal involvement. Confinement due to specific affinities to other proteins in the membrane cannot be excluded, though this is less likely when three unrelated proteins all exhibit similar confined trajectories. We conclude that the confined trajectories of transmembrane proteins we observe under normoxic conditions are likely dependent on stabilization by cytoskeleton either directly or indirectly. This confinement is absent under hypoxic conditions, which is consistent with impaired function of cytoskeleton in hypoxia (Paller, 1993).

**The lower limit of single molecule diffusion $D_{SM}$**

In Chapter 3 we determined the diffusion constant of fixed proteins in order to determine the lower limit for diffusion detectable by our method. Because the HEPES-buffered experiments require limiting the illumination intensity to which cells are exposed, and recording at a lowered frame rate, the lower limit is defined again for these experiments. Under hypoxic imaging conditions a fixed mEos3.2 sample yielded diffusion constants of about 0.01 $\mu m^2$/sec, consistent with the localization error inherent in our system. There was a small discrepancy whereby fixed proteins appeared to have

higher ‘diffusion’ constants, but this was due to a lower average quantum yield of the fixed proteins and subsequently a higher localization error. In place of measuring the ‘diffusion’ in fixed cells, we take advantage of glass-deposited proteins that have been secreted or otherwise deposited in a region of interest selected outside the cellular footprint. The cell depicted in Figure 4-3 expressed construct GG mEos3.2. This has the advantage that no reduction in quantum yield results from protein fixation in this sample. The immobile population is again centered around 0.01 $\mu m^2$/sec, and this represents the lower limit of detection in our system.

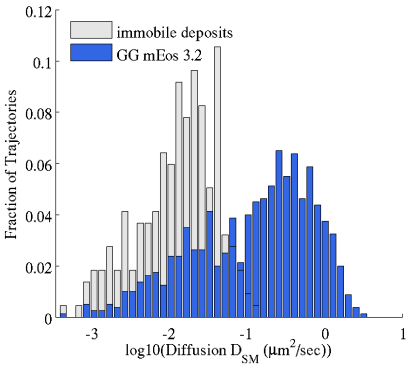


Figure 4-3 Histograms of single molecule ‘diffusion’ constants of localized particles inside and outside the footprint of a single cell expressing GG mEos3.2. The particles outside the footprint are fluorescent immobilized deposits and serve as an empirical measure of the diffusion constant of a truly mobile population. This population is centered around 0.01 $um^2$/sec as before.

**Adjusting fitting method to heterogeneous normoxic diffusion**

Figure 4-4 shows the single trajectory diffusion distribution of B-TM in both HEPES and hypoxic imaging buffers. The hypoxic conditions are treated as before, fitting to one population of Brownian diffusers. For the HEPES condition, fitting to a single population of simulated Brownian tracks is insufficient to account for the distribution of $D_{SM}$ values in this sample. The fit to two populations is shown (red) but also does not capture the entire width of the diffusion distribution. The histogram shows a

substantial peak around 0.01 $\mu m^2$/sec, where the immobile peak appears (see Figure 4-3). In comparison, B-TM barely exhibits an immobile population under hypoxic conditions.

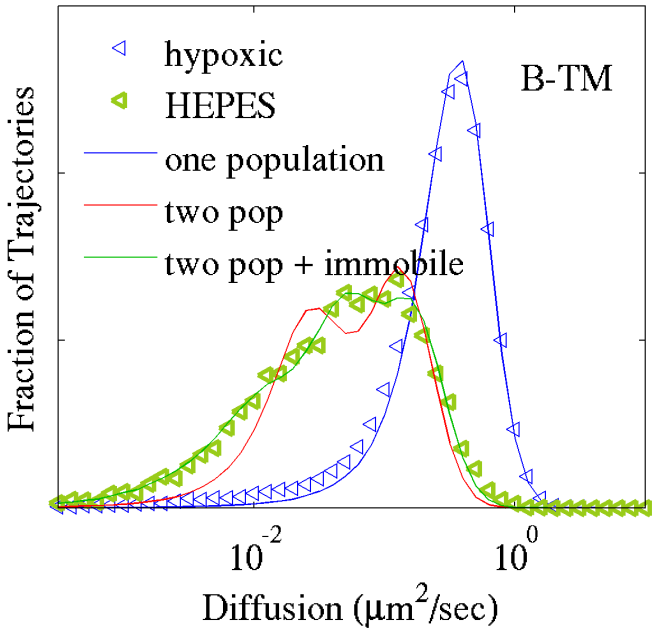


Figure 4-4 Single molecule diffusion coefficients from cells expressing B-TM. Pooled from 4 cells. In HEPES-buffered imaging solution diffusion constants are heterogeneous and slower than under hypoxic conditions. Fitting to two populations of Brownian diffusers (red line) does not sufficiently account for the distribution of data. Fitting to two mobile populations, with a fixed immobile population (not a fit parameter) the heterogeneous diffusion distribution is accounted for (green).

We chose to adapt the fitting method from Chapter 3 to include a fixed simulated immobile peak. The difference between this approach (green) and the mobile population fit only (red) are shown in Figure 4-4. We find that fitting using two populations and one immobile population accounts well for the distribution in the data. Because we can fix the immobile population instead of interpolating it as a fit parameter, both 'two population' (red) and 'two population+ immobile' (green) fits include four fit parameters. For hypoxic conditions, up to 4 fitting parameters are minimized: two distinct diffusion coefficients, the fraction of diffusers in each population, and the fraction of immobile

trajectories. With immobile fitting, fit parameters include the diffusion constants for each population, and the fraction of trajectories belonging to each population.

**Diffusion is heterogeneous for all constructs under normoxic conditions**

We apply the modified Brownian simulation-coupled fitting approach described above to determine diffusion constants of each of the constructs from Chapter 3 in HEPES buffer. Figure 4-5 shows each of the six mEos 3.2 fusion proteins. In each case, regardless of size, phase association, and mode of membrane anchoring, the single molecule diffusion distributions are heterogeneous and slower than under hypoxic conditions.

Notably, the three population fits appears to represent the width of single molecule diffusion distributions fairly well, but does not capture all of its features. For example, especially for the inner leaflet lipid anchored probes GG and PM appear to have single molecule diffusion values in between the immobile and slower mobile population. There are a couple of reasons why this could be. First, this method of fitting diffusion distributions may not predict the data well when diffusion is not Brownian. Second, there could be an exchange between the slower mobile population and the immobile. Finally, it is possible that while the width is consistent with two mobile and one immobile population, that the lateral diffusion behavior is more actually complex.

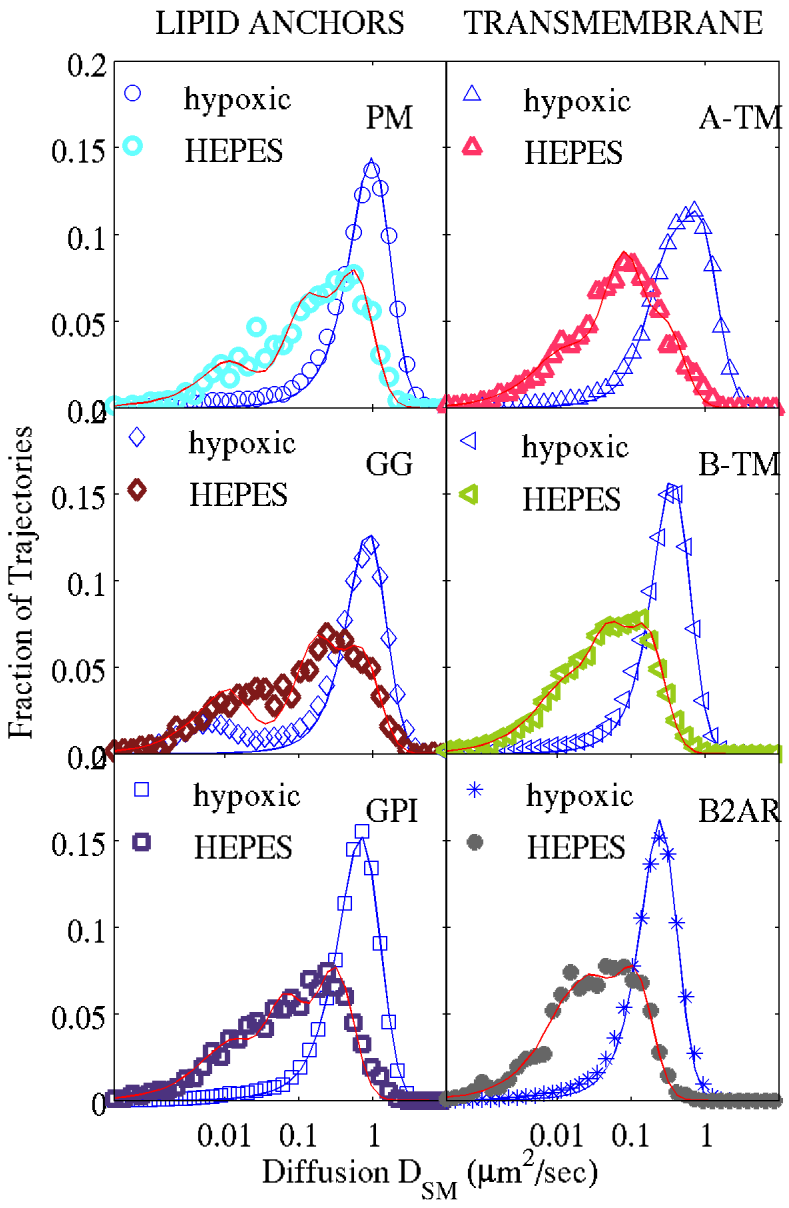


Figure 4-5 Diffusion is slower and heterogeneous under hypoxic conditions. Histograms of single molecule diffusion constants of each fusion protein recorded in HEPES overlaid on histograms of diffusion histograms of the same construct under hypoxic conditions.

We present the population diffusion values of each of the mobile peaks and their overall fraction in Table 4-1. Comparing these to the diffusion constants determined for the hypoxic conditions we find that the faster mobile peak of the transmembrane proteins in HEPES-buffered imaging solution diffuse a factor of two or more slower than in the hypoxic conditions. The diffusion of the acyl probes is decreased by a factor of 1.2 to 1.7.

The slow mobile population is a factor of approximately 3.5 to 4.6 fold slower than the faster mobile population in all cases. This factor decreases with decreasing rate of diffusion (PM 4.6 fold to $\beta_2$AR 3.5 fold). For all constructs, 20-29% of the detected particles are immobile in the HEPES-buffered conditions, whereas under hypoxic conditions 3-20% were immobile depending on the construct.

Table 4-1 Diffusion values comparing overall diffusion constants from hypoxic conditions determined for Chapter 3, and the diffusion constants of the fast and slow populations detected in HEPES buffer. The fraction of trajectories that are mobile are also listed. Each value is averaged from 2-10 recordings. The errors represented are the standard error of the means.

| Anchor | Hypoxic Diffusion ($\mu m^2$/sec) | Diffusion in HEPES fast ($\mu m^2$/sec) | Diffusion in HEPES slow ($\mu m^2$/sec) | Fraction mobile |
|---|---|---|---|---|
| PM | 0.97 ± 0.19 | 0.59 ± 0.04 | 0.127 ± 0.007 | 0.79 ± 0.04 |
| GG | 0.99 ± 0.16 | 0.81 ± 0.08 | 0.18 ± 0.02 | 0.71 ± 0.04 |
| GPI | 0.73 ± 0.056 | 0.42 ± 0.09 | 0.10 ± 0.03 | 0.79 ± 0.04 |
| A-TM | 0.92 ± 0.17<br>0.33 ± 0.037 | 0.37 ± 0.06 | 0.09 ± 0.01 | 0.78 ± 0.04 |
| B-TM | 0.40 ± 0.012 | 0.16 ± 0.02 | 0.047 ± 0.005 | 0.78 ± 0.07 |
| $\beta_2$AR | 0.275 ±0.0082 | 0.14 ± 0.02 | 0.04 ± 0.01 | 0.74 ± 0.01 |

Lommerse *et al.* found that analysis of probes similar to our PM and GG anchors resulted in a freely diffusing population with a similar rate of diffusion as ours, and then a confined and less mobile component (Lommerse et al., 2006). Our findings are consistent with theirs except they do not distinguish between highly confined and outright immobile components. This may be because they use cumulative displacement analysis rather than trajectories to examine the mobility of their probes. As explored in Chapter 3, our method offers an alternative approach to identifying multiple populations.

Interestingly, the fractions of fast mobile, slow mobile, and immobile are similar across all constructs (Table 4-1). The immobile fraction represents less than a third and each of the mobile populations have half the remaining trajectories. As discussed for

Figure 4-2, the diffusion heterogeneity may be caused by protein obstacles stabilized by cytoskeleton or phase-heterogeneity stabilized by cytoskeleton. In either case, these diffusion profiles are remarkably consistent among these probes which have different modes of membrane anchoring, different sizes, diffusion constants ranging over half an order of magnitude, and different putative phase-associations. This suggests that heterogeneity stems from general structural features to which all these probes are equally subject.

Overall, the diffusion values determined for these probes fall within the range published in the literature. The range is very broad due to a variety of experimental differences such as methods, diffusion models, treatment of populations, cell lines, etc. GG and PM diffuse between 0.4 and 1.1 $\mu m^2$/sec (Kenworthy et al., 2004; Lommerse et al., 2006; Niv et al., 2002). GPI-anchored proteins diffuse at 0.17-1.1 $\mu m^2$/sec (Kenworthy et al., 2004; Nishimura et al., 2006; Shvartsman et al., 2003; Umemura et al., 2008; Wieser et al., 2007). Diffusion constants of transmembrane constructs like B-TM and A-TM have been recorded at 0.14 - 0.58 $\mu m^2$/sec (Kenworthy et al., 2004; Nishimura et al., 2006; Shvartsman et al., 2003; Umemura et al., 2008). Finally, GPCRs diffuse at rates between 0.013 - 0.48 $\mu m^2$/sec (Daumas et al., 2003; Horvat et al., 1999; Nelson et al., 1999; Sauliere-Nzeh Ndong et al., 2010; Suzuki et al., 2005; Young et al., 2001). Because this range of diffusion constants for each construct is so wide, both hypoxic and normoxic diffusion constants agree with literature.

Previous studies have found comparable fractions of immobile components. Kenworthy *et al.* found 85-90% mobile fraction, across multiple constructs (Kenworthy et al., 2004). Lommerse et al. found approximately 40% confinement for constructs that

are similar to PM and GG, and as mentioned before, are likely composed of both an immobile and highly confined mobile diffusers (Lommerse et al., 2006). Neither group found correlations between the degree of immobilization and phase-association, which agrees with our data. Cholesterol depletion also had no effect on the mobile fraction (Lommerse et al., 2006), which the authors attributed to cytoskeletal stabilizing effects of cholesterol depletion (Kwik et al., 2003). That the immobile fraction and cytoskeleton are linked is consistent with an interpretation that cytoskeleton is dysfunctional in hypoxic cells, resulting in the substantially decreased fraction of immobile proteins.

**Protein mobility depends on anchor size under normoxic conditions**

In Chapter 3 we showed the relationship between size of membrane anchor and diffusion, and found that size-dependence of diffusion rates was greater for smaller membrane anchors, consistent with studies in model membranes. We have seen that diffusion rate in the membrane of hypoxic cells appear simpler than those in normoxic buffer conditions. We ask, therefore, whether the diffusion of the faster mobile component in HEPES buffer is dependent on the radius in the same way (Figure 4-6).

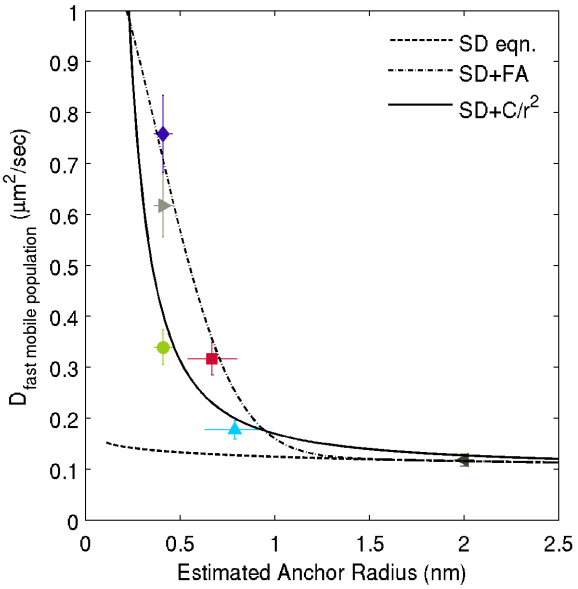


Figure 4-6 Diffusion values of the faster of the two mobile populations versus estimated size of embedded membrane anchor lateral diffusion in HEPES buffer. Error bars on the x-axis represent uncertainty in size estimation (see Materials and Methods). Y-error bars are the standard error of means of $D_{MP}$ averaged over at least three cells. Models represented include the Saffman-Delbrück (SD) and a super position of the SD and free area models (FA) as detailed in Materials and Methods. Saffman-Delbrück length was adjusted to 25 µm, whereas 10 µm were used in the Chapter 3.

The relationship between estimated anchor radius and diffusion constant largely holds under normoxic conditions (Figure 4-7). However, adjustments had to be made to the fit parameters of the models presented. Most notably, the hydrodynamic length in the Saffman-Delbrück model was changed from 10 to 25 µm. The hydrodynamic length is dependent on the ratio of viscosities of the membrane and surrounding fluid (see Materials and Methods). That this value had to be increased to fit the data suggests that the membrane viscosity is higher under normoxic conditions. This is consistent with the decrease in diffusion constant for all probes under hypoxic conditions, and also, with changes to the lipid bilayer in response to hypoxic conditions, as previously observed for lipid peroxidation.

Importantly, our conclusions about the size dependence of diffusion from Chapter 3 hold under normoxic conditions, namely, size dependence of diffusion is greater for

smaller probes. This means that oligomerization of lipid-anchored and single transmembrane proteins result in a substantial diffusion decrease, whereas larger proteins like GPCRs are less affected. Consequently, the diffusion of small proteins may be modulated by oligomerization events *in vivo*, and not just under hypoxic conditions. Furthermore, this indicates that single particle tracking is a valuable technique to monitor dimerization events based on diffusion, but only for small proteins because the sensitivity of the technique is insufficient to unambiguously determine dimerization events of larger proteins.

**B-TM is confined under normoxic conditions**

In Figure 4-2 we showed that trajectories of B-TM appeared confined under normoxic conditions. We quantify the degree of confinement using single molecule $\alpha_{SM}$ histograms as in Figure 4-7.

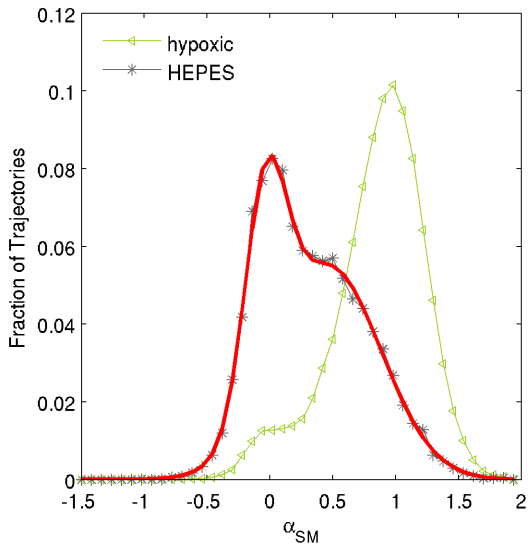


Figure 4-7 Single trajectory α histogram for B-TM in hypoxic or HEPES-buffered imaging solution. The HEPES condition is fit by two Gaussian functions with peak values at 0 and 0.5 ± 0.1 α.

The diffusion of B-TM is substantially more confined in HEPES-buffered imaging solution than under hypoxic conditions. There is a much larger population at α of 0, which in Chapter 3 was due to immobile trajectories. The mobile trajectories are also more confined. Most trajectories have α values less than one, indicating anomalous subdiffusion. The populations are not well resolved. Either this represents a wide range of confinements or the exchange of individual trajectories between the mobile, less mobile, and immobile states, or possibly both. Together, this indicates that one reason the diffusion of this construct is slower in normoxic samples is higher confinement.

Assigning an overall α value to represent these populations of confined diffusers is done using two Gaussian fits. Since α represents non-Brownian diffusion, it is not as simple to predict the width of the single molecule α or diffusion distributions with simulations, as we do in Chapter 3. One alternative approach is presenting the ensemble average. These are listed in Table 4-2. In Chapter 3, we also present the mean of $\alpha_{SM}$ values above 0.45, and compare these by bootstrapping to simulated Brownian tracks to determine if the two means are significantly different. Because the mobile and immobile populations are resolved, 0.45 is a reasonable cut-off to analyze one population separately from the other. In the normoxic case, the two populations are overlapped, and 0.45 is not a reasonable cut-off. Furthermore the α values of the mobile peak is so substantially lower than the Brownian value of $\alpha = 1$ that bootstrapping to determine difference from simulations is unnecessary. Therefore we fit with two Gaussian functions to determine the overall α values of the two peaks. These are presented along with $\alpha>0.45$ values for hypoxic conditions in Table 4-2.

In Chapter 3 we discovered that one anchor (A-TM mEos3.2 and A-TM mEos2) exhibited two populations of diffusers but neither population showed confinement. In Figure 4-7 we have a substantial population at $\alpha = 0$, and a broad, less confined population of sub-anomalous diffusers. We determine the fraction of trajectories belonging to the broad, less confined population and compare this value with the fraction of mobile trajectories from the $D_{SM}$ distribution. This gives an indication of whether $\alpha = 0$ represents only immobile trajectories or also some fraction of mobile trajectories. We find that the less confined peak contains 71% of the trajectories for this construct. This agrees well with the fraction of mobile diffusers for this construct, which is $0.78 \pm 0.07$, as shown in Table 4-1. This indicates that mobile diffusers belong to the less confined $\alpha$ peak and that $\alpha = 0$ represents almost exclusively immobile trajectories.

**All constructs are confined under normoxic conditions**

Histograms of single trajectory $\alpha$ values are presented in Figure 4-8 for all Chapter 3 constructs. Under hypoxic conditions, all proteins diffuse in a manner consistent with Brownian and unconfined diffusion as established in Chapter 3. Diffusion of all constructs in HEPES buffer is more confined, similar to B-TM (Figure 4-7).

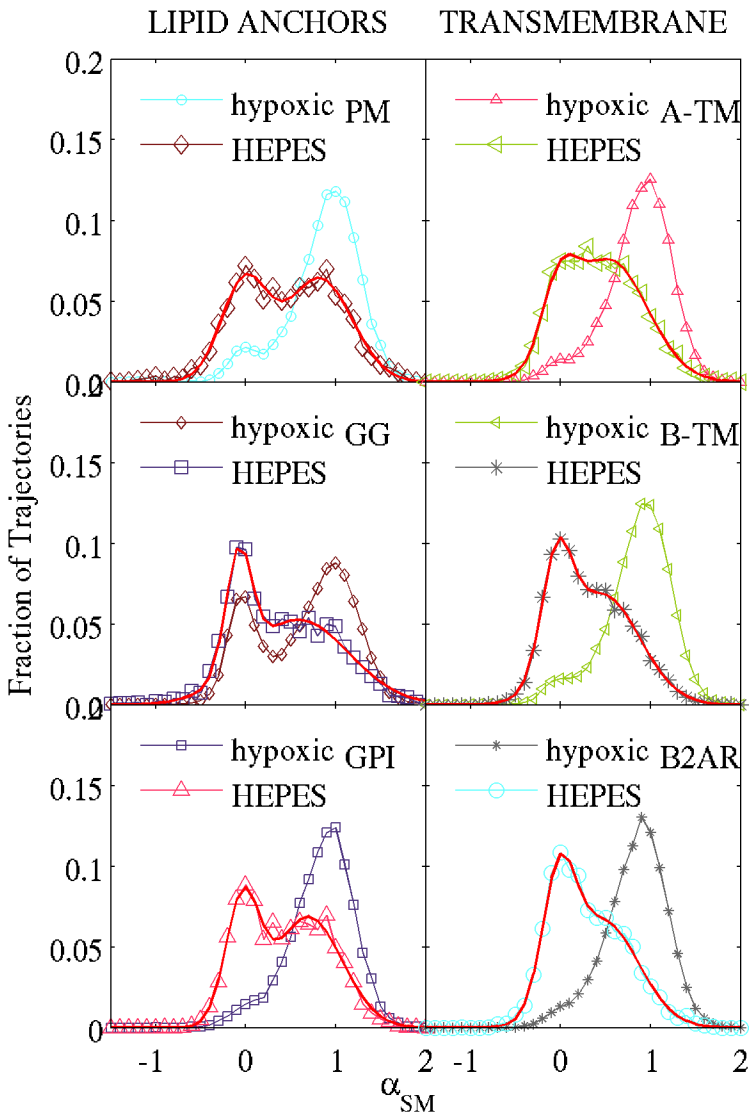


Figure 4-8 The lateral diffusion of fusion proteins is confined for all constructs tested under normoxic conditions. Fitting to two Gaussian fits consistently yields peaks centered around zero for the confined population and values between 0.5 and 0.83 for the less confined population. See Table 4-2.

Table 4-2 Population α values of lateral diffusion under hypoxic and HEPES-buffered conditions.

| Buffer: | Hypoxic | | HEPES-buffer | |
|---|---|---|---|---|
| Anchor | Mean α (ensemble) | Mean α greater than 0.45 | Mean α (ensemble) | Mobile peak Gaussian fit ± S.E.M. |
| PM | 0.90 | 0.98 | 0.52 | 0.83 ± 0.08 |
| GG | 0.69 | 1.0 | 0.45 | 0.58 ± 0.01 |
| GPI | 0.88 | 0.97 | 0.48 | 0.70 ± 0.03 |
| A-TM | 0.91 | 1.0 | 0.48 | 0.55 ± 0.06 |
| B-TM | 0.89 | 0.99 | 0.48 | 0.5 ± 0.1 |
| $\beta_2$AR | 0.87 | 0.96 | 0.35 | 0.52 ± 0.07 |

Under HEPES-buffered conditions, all transmembrane proteins appear to be similarly confined, with $\alpha_{SM}$ values of about 0.5 for the mobile peak. In contrast, lipid-anchored proteins are less confined, and the $L_o$-associated PM and GPI appear to be less confined than $L_d$-associated GG.

It is striking that GG is so confined, especially in light of the small difference between its diffusion in hypoxic and normoxic conditions. It is possible that this is the product of an artifact. When short trajectories terminate close to immobile particles their tracks can be erroneously joined. This artifact is exacerbated when samples are dense, the immobile fraction is high, and diffusion is fast. Alternatively, perhaps the confinement stems from membrane heterogeneity with a structure amenable to both confinement and fast diffusion at short time scales. Such heterogeneity would be disrupted under hypoxic conditions.

Again we compare the fraction of mobile diffusers in Table 4-1 to the less confined peak in of each $\alpha_{SM}$ histogram in Figure 4-8 to confirm that the $\alpha = 0$ peak represents the immobile fraction only. The fraction mobile are listed in Table 4-3. The values for the mobile peak estimated from αSM and DSM histograms agree fairly well. Discrepancies fall within the error presented for the DSM mobile fraction for the A-TM,

B-TM, and GG constructs, but for PM, GPI, and $\beta_2$AR the discrepancy is 10% or higher difference. This suggests that for these constructs, the $\alpha = 0$ peak is populated by the immobile fraction primarily but that an additional fraction of highly confined mobile trajectories contribute to the $\alpha = 0$ peak. These probes are putatively $L_o$-associated and so this difference may be attributable to membrane heterogeneity.

Table 4-3 Fraction of trajectories that belong to less confined $\alpha$ peak

| Construct | Fraction of trajectories that belong to less confined $\alpha$ peak |
|---|---|
| PM | 0.59 |
| GG | 0.74 |
| GPI | 0.65 |
| A-TM | 0.80 |
| B-TM | 0.71 |
| $\beta_2$AR | 0.65 |

**Temperature dependence is lower under normoxic than hypoxic conditions**

In Chapter 3 we determine the temperature dependence of apparent activation energy ($E_a$) of diffusion in cells under hypoxic imaging conditions. In Figure 4-9 we compare diffusion values at 23°C and 37°C as an indication of whether a similarly steep relationship to temperature is maintained under normoxic conditions. We find a relatively small difference in diffusion in cells expressing B-TM mEos3.2. As a preliminary indication, the slope between these two points on an Arrhenius plot corresponds to 26 kJ $mol^{-1}$ apparent $E_a$. This is the same value as determined for EGFR (Hillman and Schlessinger, 1982). Diffusion values for more points must be collected for a meaningful conclusion and determination of errors. $E_a$ for the same construct imaged in cells imaged in hypoxic buffer is 117 ± 7 kJ $mol^{-1}$ apparent $E_a$ and 130 ± 22 kJ $mol^{-1}$ in giant plasma membrane vesicles (GPMVs).

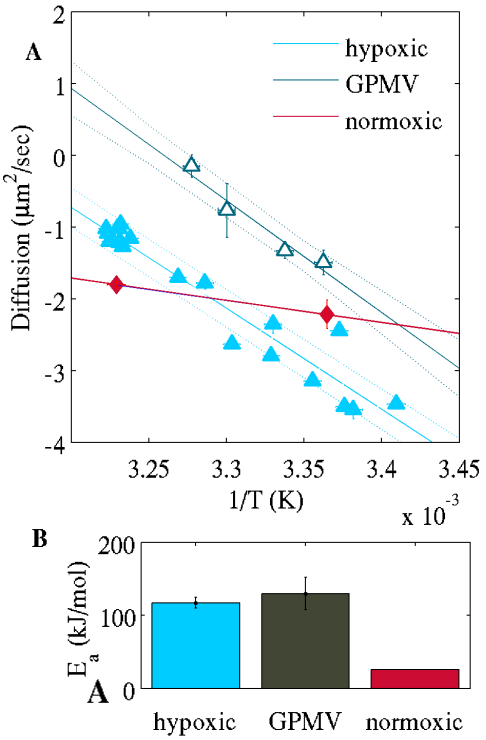


Figure 4-9 Apparent activation energy is lower for lateral diffusion of B-TM in normoxic buffer than either GPMVs or hypoxic conditions. (A) Shows Arrhenius plots of lateral diffusion of B-TM in hypoxic conditions, a CHO cell GPMV, and normoxic cells. Error bars on points from hypoxic conditions are determined by bootstrapping, and by standard deviation of the mean for GPMV and normoxic cells. Dotted lines represent error bounds, which are absent for normoxic cells due to the dearth of data points. (B) Bar chart comparing the calculated apparent activation energies for each condition: 117 ± 7 kJ $mol^{-1}$ for hypoxic, 130 ± 22 kJ $mol^{-1}$ in GPMVs, and 26 $kJmol^{-1}$ for normoxic conditions. The values plotted for normoxic conditions are means of the 3-5 cells recorded at each temperature.

The apparent activation energy of B-TM in hypoxic cells is more similar to $E_a$ in GPMVs than normoxic cells. In Chapter 3 we concluded that temperature dependent physical properties of membrane, such as viscosity, govern the temperature dependence of diffusion. Under normoxic conditions, this is not the case. Again, this suggests that hypoxic cells have impaired cytoskeletal function, as GPMVs are void of cytoskeleton.

For the purpose of lateral diffusion studies the low temperature-dependence of diffusion is important because it makes diffusion studies less restrictive. In hypoxic conditions, because the temperature sensitivity of diffusion is so high, careful temperature control is a prerequisite for cell-to-cell consistency. Under normoxic

conditions, cell-to-cell variability may still be considerable but it stems from heterogeneity inherent to the cells under study.

**Transition temperature increases under hypoxic conditions**

Literature suggests that faster diffusion of proteins in the membrane under oxidative stress relates to lipid peroxidation. This encompasses a large number of possible chemical changes to the membrane lipids such as chain shortening, rearrangements, and decomposition (Paller, 1993). If this is a major contributor to the differences we see between the hypoxic and normoxic conditions, we would hypothesize that the transition temperature of the membrane would change.

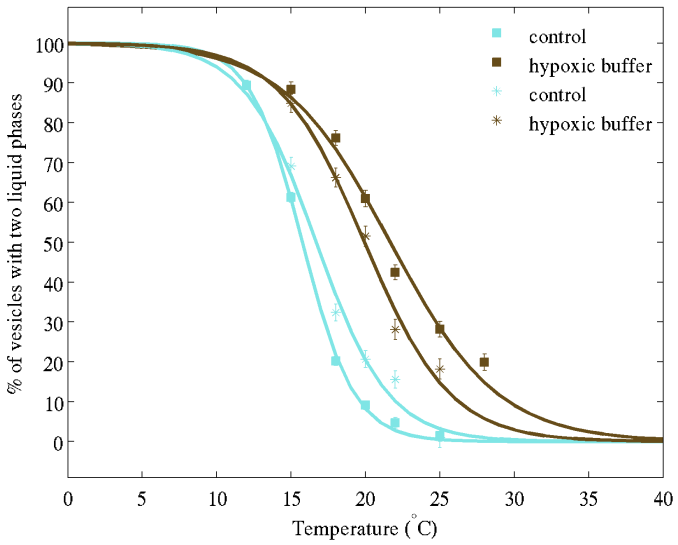


Figure 4-10 Transition temperature of giant plasma membrane vesicles extracted from HeLa cells change after exposing the cells to hypoxic imaging buffer for 30 minutes. The transition temperature is 16.2 ± 0.7°C in the control, and 20.8 ± 1.2°C after 30 minute exposure. Errors are standard deviations. Jing Wu.

In an effort to quantify the degree to which the membrane is different under hypoxic and HEPES-buffered normoxic conditions, we generate GPMVs from HeLa cells exposed to normoxic buffer and determine the effect on their transition temperature.

Figure 4-10 shows the phase separation curves from cells exposed to imaging buffer for 0, and 30 minutes. Jing Wu of the Veatch Lab generously executed this experiment. We find that the average transition temperature increases 4.6°C from 16.2 ± 0.7°C to 20.8 ± 1.2°C. This suggests substantial changes occur in the membrane composition under hypoxic conditions, consistent with lipid peroxidation or similar chemical changes to the membrane lipids that occur gradually over time.

## Conclusions

In this chapter we have characterized the differences between lateral diffusion of a panel of membrane probes under normoxic and hypoxic conditions. We find that hypoxia causes a substantially different lateral diffusion profile.

Our primary conclusion from this study is that lateral diffusion in hypoxic conditions is consistent with both lipid peroxidation *and* cytoskeletal dysfunction. The transition temperature experiment shows that isolated plasma membrane undergoes substantial differences in chemical composition when compared to control suggesting lipid peroxidation. However, diffusion heterogeneity and confinement are different between normoxic and hypoxic conditions beyond what lipid peroxidation could cause, and suggest that cytoskeleton plays an important role in defining the phenotypic differences between the two. Clearly, not all interactions between membrane and cytoskeleton are eliminated, or blebs would result. Though cellular imaging typically takes place at 20-21% oxygen, the $PO_2$ *in vivo* is much lower. It would be interesting to test if a third lateral diffusion phenotype were evident under physiological oxygen levels, though this is outside the scope of this study.

Secondly, we found that diffusion profiles of all membrane probes are more complex and confined under normoxic conditions compared to hypoxia. The use of oxygen-scavenging and reducing buffer is designed to reduce the effect of ROS on fluorophores, but ironically induces stresses the live cells in a way that releases ROS from their mitochondria. Consequently, though the morphological consequences of phototoxicity are reduced, hypoxic buffer introduces a phenotype that likely corresponds to oxidative stress, such as occurs in multiple disease states.

Third, though we see evidence of long-range heterogeneity in the cells under normoxic conditions, these do not appear to be correlated with phase association, as phenotypic differences between $L_o$ and $L_d$ probes in our samples were barely detected. In fact, the diffusion profiles are shockingly consistent among different sizes and types of membrane anchoring, with similar fractions of fast, slow and immobile particles.

Fourth, we conclude that phototoxicity occurs during imaging of mEos proteins, regardless of buffer. This limits applications of this useful fluorescent protein. We use a short-term limited light exposure protocol for imaging live cells, and a sensitive camera and TIRF illumination to reduce the need for high laser intensity. Other techniques to further limit exposure to light should be considered when imaging mEos. Future development of a more photo-protective buffer perhaps incorporating antioxidants such as α tocopherol may be useful. Not all cells may be as sensitive as HeLa to phototoxicity, and alternative model cells could be considered. Application of this protein to bulk imaging may be auspicious, but we caution against the use of mEos and other green-excitable proteins for single particle tracking except for limited-light-exposure experiments such as the ones described here.

Finally we find the temperature dependence of diffusion is substantially lower under normoxic conditions, though lateral diffusion still appears thermally activated. This suggests that under hypoxic conditions temperature dependence of membrane physical properties govern the temperature dependence of diffusion, whereas this effect is overridden by other factors in normoxic cells.

Overall many changes happen in cells under hypoxic conditions. Up-regulation of genes such as VEGF, EPO, GLUT1 and regulated by oxygen sensing transcription regulators, and reactive oxygen species chemically modify biomolecules (Ohh et al., 2000). Consequently, detrimental effects are seen in cells including aggression and treatment-resistance of cancers. EGFR in particular is activated by hypoxic conditions. As demonstrated here, dynamics at the membrane surface of cells is highly affected. Conceivably, the fast and unrestricted interactions of various signaling components such as EGFR may exacerbate the biological consequences of hypoxia.

As it relates to our central question of whether palmitoylation changes the rate of lateral diffusion we conclude the following. First, HEPES imaging buffer and low light exposure is a more appropriate approximation for physiological conditions than is photoprotective hypoxic buffer. Second, we find that under normoxic conditions, the same conclusions hold about size and cell-to-cell variability as in photoprotective buffer.

## Work Cited


Bates, M., Huang, B., Dempsey, G.T., and Zhuang, X. (2007). Multicolor super-resolution imaging with photo-switchable fluorescent probes. Science *317*, 1749–1753.

Behn, C., Araneda, O.F., Llanos, A.J., Celedón, G., and González, G. (2007). Hypoxia-related lipid peroxidation: evidences, implications and approaches. Respir. Physiol. Neurobiol. *158*, 143–150.

Carreau, A., Hafny-Rahbi, B.E., Matejuk, A., Grillon, C., and Kieda, C. (2011). Why is the partial oxygen pressure of human tissues a crucial parameter? Small molecules and hypoxia. J. Cell. Mol. Med. *15*, 1239–1253.

Celedón, G., González, G., Sotomayor, C.P., and Behn, C. (1998). Membrane lipid diffusion and band 3 protein changes in human erythrocytes due to acute hypobaric hypoxia. Am. J. Physiol.-Cell Physiol. *275*, C1429–C1431.

Chang, N., and Goodson, W.H. (1983). Direct measurement of wound and tissue oxygen tension in postoperative patients. Ann. Surg. *197*, 470.

Clausen, M.P., and Lagerholm, B.C. (2013). Visualization of plasma membrane compartmentalization by high-speed quantum dot tracking. Nano Lett *13*, 2332–2337.

Dailey, M.E., Focht, D.C., Rieder, C.L., Khodjakov, A., Spring, K.R., Claxton, N., Olenych, S.G., Griffin, J.D., and Davidson, M.W. (2013). Maintaining Live Cells on the Microscope Stage.

Daumas, F., Destainville, N., Millot, C., Lopez, A., Dean, D., and Salome, L. (2003). Confined diffusion without fences of a g-protein-coupled receptor as revealed by single particle tracking. Biophys J *84*, 356–366.

Endesfelder, U., Malkusch, S., Flottmann, B., Mondry, J., Liguzinski, P., Verveer, P.J., and Heilemann, M. (2011). Chemically induced photoswitching of fluorescent probes--a general concept for super-resolution microscopy. Molecules *16*, 3106–3118.

Frigault, M.M., Lacoste, J., Swift, J.L., and Brown, C.M. (2009). Live-cell microscopy – tips and tools. J. Cell Sci. *122*, 753–767.

Giaccia, A.J., Simon, M.C., and Johnson, R. (2004). The biology of hypoxia: the role of oxygen sensing in development, normal function, and disease. Genes Dev. *18*, 2183–2194.

Godley, B.F., Shamsi, F.A., Liang, F.-Q., Jarrett, S.G., Davies, S., and Boulton, M. (2005). Blue Light Induces Mitochondrial DNA Damage and Free Radical Production in Epithelial Cells. J. Biol. Chem. *280*, 21061–21066.

De Groot, H., and Noll, T. (1987). The role of physiological oxygen partial pressures in lipid peroxidation. Theoretical considerations and experimental evidence. Chem. Phys. Lipids *44*, 209–226.

Halliwell, B., and Chirico, S. (1993). Lipid peroxidation: its mechanism, measurement, and significance. Am. J. Clin. Nutr. *57*, 715S–724S.

Halliwell, B., and Cross, C.E. (1994). Oxygen-derived species: their relation to human disease and environmental stress. Environ. Health Perspect. *102*, 5–12.

Heerlein, K., Schulze, A., Hotz, L., Bärtsch, P., and Mairbäurl, H. (2005). Hypoxia Decreases Cellular ATP Demand and Inhibits Mitochondrial Respiration of A549 Cells. Am. J. Respir. Cell Mol. Biol. *32*, 44–51.

Hillman, G.M., and Schlessinger, J. (1982). Lateral diffusion of epidermal growth factor complexed to its surface receptors does not account for the thermal sensitivity of patch formation and endocytosis. Biochemistry (Mosc.) *21*, 1667–1672.

Hoebe, R.A., Van Oven, C.H., Gadella, T.W., Dhonukshe, P.B., Van Noorden, C.J.F., and Manders, E.M.M. (2007). Controlled light-exposure microscopy reduces photobleaching and phototoxicity in fluorescence live-cell imaging. Nat. Biotechnol. *25*, 249–253.

Hoogsteen, I.J., Marres, H.A.M., van den Hoogen, F.J.A., Rijken, P.F.J.W., Lok, J., Bussink, J., and Kaanders, J.H.A.M. (2012). Expression of EGFR under tumor hypoxia: identification of a subpopulation of tumor cells responsible for aggressiveness and treatment resistance. Int. J. Radiat. Oncol. Biol. Phys. *84*, 807–814.

Horvat, R.D., Nelson, S., Clay, C.M., Barisas, B.G., and Roess, D.A. (1999). Intrinsically fluorescent luteinizing hormone receptor demonstrates hormone-driven aggregation. Biochem Biophys Res Commun *255*, 382–385.

Huang, B., Jones, S.A., Brandenburg, B., and Zhuang, X. (2008). Whole-cell 3D STORM reveals interactions between cellular structures with nanometer-scale resolution. Nat. Methods *5*, 1047–1052.

Ivan, M., Kondo, K., Yang, H., Kim, W., Valiando, J., Ohh, M., Salic, A., Asara, J.M., Lane, W.S., and Kaelin Jr, W.G. (2001). HIFα targeted for VHL-mediated destruction by proline hydroxylation: implications for O2 sensing. Science *292*, 464–468.

Johnson, R.D., Schauerte, J.A., Wisser, K.C., Gafni, A., and Steel, D.G. (2011). Direct observation of single amyloid-β (1-40) oligomers on live cells: binding and growth at physiological concentrations. PloS One *6*, e23970.

Kenworthy, A.K., Nichols, B.J., Remmert, C.L., Hendrix, G.M., Kumar, M., Zimmerberg, J., and Lippincott-Schwartz, J. (2004). Dynamics of putative raft-associated proteins at the cell surface. J Cell Biol *165*, 735–746.

Kusumi, A., Nakada, C., Ritchie, K., Murase, K., Suzuki, K., Murakoshi, H., Kasai, R.S., Kondo, J., and Fujiwara, T. (2005). Paradigm shift of the plasma membrane concept from the two-dimensional continuum fluid to the partitioned fluid: high-speed single-molecule tracking of membrane molecules. Annu Rev Biophys Biomol Struct *34*, 351–378.

Kwik, J., Boyle, S., Fooksman, D., Margolis, L., Sheetz, M.P., and Edidin, M. (2003). Membrane cholesterol, lateral mobility, and the phosphatidylinositol 4,5-bisphosphate-dependent organization of cell actin. Proc. Natl. Acad. Sci. *100*, 13964–13969.

Lemasters, J.J., Stemkowski, C.J., Ji, S., and Thurman, R.G. (1983). Cell surface changes and enzyme release during hypoxia and reoxygenation in the isolated, perfused rat liver. J. Cell Biol. *97*, 778–786.

Lepe-Zuniga, J.L., Zigler Jr, J.S., and Gery, I. (1987). Toxicity of light-exposed Hepes media. J. Immunol. Methods *103*, 145.

Lommerse, P.H., Vastenhoud, K., Pirinen, N.J., Magee, A.I., Spaink, H.P., and Schmidt, T. (2006). Single-molecule diffusion reveals similar mobility for the Lck, H-ras, and K-ras membrane anchors. Biophys J *91*, 1090–1097.

Manley, S., Gillette, J.M., Patterson, G.H., Shroff, H., Hess, H.F., Betzig, E., and Lippincott-Schwartz, J. (2008). High-density mapping of single-molecule trajectories with photoactivated localization microscopy. Nat. Methods *5*, 155–157.

Miller, E.W., Albers, A.E., Pralle, A., Isacoff, E.Y., and Chang, C.J. (2005). Boronate-Based Fluorescent Probes for Imaging Cellular Hydrogen Peroxide. J. Am. Chem. Soc. *127*, 16652–16659.

Nelson, S., Horvat, R.D., Malvey, J., Roess, D.A., Barisas, B.G., and Clay, C.M. (1999). Characterization of an intrinsically fluorescent gonadotropin-releasing hormone receptor and effects of ligand binding on receptor lateral diffusion. Endocrinology *140*, 950–957.

Nishigaki, T., Wood, C., Shiba, K., Baba, S., and Darszon, A. (2006). Stroboscopic illumination using light-emitting diodes reduces phototoxicity in fluorescence cell imaging. BioTechniques *41*, 191–197.

Nishimura, S.Y., Vrljic, M., Klein, L.O., McConnell, H.M., and Moerner, W.E. (2006). Cholesterol depletion induces solid-like regions in the plasma membrane. Biophys J *90*, 927–938.

Niv, H., Gutman, O., Kloog, Y., and Henis, Y.I. (2002). Activated K-Ras and H-Ras display different interactions with saturable nonraft sites at the surface of live cells. J. Cell Biol. *157*, 865–872.

Ohh, M., Park, C.W., Ivan, M., Hoffman, M.A., Kim, T.-Y., Huang, L.E., Pavletich, N., Chau, V., and Kaelin, W.G. (2000). Ubiquitination of hypoxia-inducible factor requires direct binding to the &bgr;-domain of the von Hippel–Lindau protein. Nat. Cell Biol. *2*, 423–427.

Paller, M.S. (1993). Lateral diffusion of lipids in renal cells: effects of hypoxia and reoxygenation and role of cytoskeleton. Am. J. Physiol. *264*, C201–208.

Di Rienzo, C., Gratton, E., Beltram, F., and Cardarelli, F. (2013). Fast spatiotemporal correlation spectroscopy to determine protein lateral diffusion laws in live cell membranes. Proc. Natl. Acad. Sci. *110*, 12307–12312.

Rust, M.J., Bates, M., and Zhuang, X. (2006). Sub-diffraction-limit imaging by stochastic optical reconstruction microscopy (STORM). Nat Methods *3*, 793–795.

Sauliere-Nzeh Ndong, A., Millot, C., Corbani, M., Mazeres, S., Lopez, A., and Salome, L. (2010). Agonist-selective dynamic compartmentalization of human Mu opioid receptor as revealed by resolutive FRAP analysis. J Biol Chem *285*, 14514–14520.

Saxton, M.J. (1994). Anomalous diffusion due to obstacles: a Monte Carlo study. Biophys. J. *66*, 394–401.

Schutz, G.J., Kada, G., Pastushenko, V.P., and Schindler, H. (2000). Properties of lipid microdomains in a muscle cell membrane visualized by single molecule microscopy. EMBO J *19*, 892–901.

Shi, X., Lim, J., and Ha, T. (2010). Acidification of the Oxygen Scavenging System in Single-Molecule Fluorescence Studies: In Situ Sensing with a Ratiometric Dual-Emission Probe. Anal. Chem. *82*, 6132–6138.

Shvartsman, D.E., Kotler, M., Tall, R.D., Roth, M.G., and Henis, Y.I. (2003). Differently anchored influenza hemagglutinin mutants display distinct interaction dynamics with mutual rafts. J Cell Biol *163*, 879–888.

Suzuki, K., Ritchie, K., Kajikawa, E., Fujiwara, T., and Kusumi, A. (2005). Rapid hop diffusion of a G-protein-coupled receptor in the plasma membrane as revealed by single-molecule techniques. Biophys J *88*, 3659–3680.

Umemura, Y.M., Vrljic, M., Nishimura, S.Y., Fujiwara, T.K., Suzuki, K.G., and Kusumi, A. (2008). Both MHC class II and its GPI-anchored form undergo hop diffusion as observed by single-molecule tracking. Biophys J *95*, 435–450.

Wang, X., and Schneider, A. (2010). HIF-2 -mediated activation of the epidermal growth factor receptor potentiates head and neck cancer cell migration in response to hypoxia. Carcinogenesis *31*, 1202–1210.

Wieser, S., Moertelmaier, M., Fuertbauer, E., Stockinger, H., and Schutz, G.J. (2007). (Un)confined diffusion of CD59 in the plasma membrane determined by high-resolution single molecule microscopy. Biophys J *92*, 3719–3728.

Young, S.H., Walsh, J.H., Rozengurt, E., and Slice, L.W. (2001). Agonist-dependent immobilization of chimeric bombesin/GRP receptors: dependence on c-Src activity and dissociation from internalization. Exp Cell Res *267*, 37–44.

# Chapter 5

# The effect of palmitoylation on lateral diffusion

## Introduction

Palmitoylation is the only lipid post-translational lipid modification of proteins that is reversible (Resh, 1999). Palmitoylation occurs in over a hundred proteins including G-proteins and their signaling partners (G Protein-Coupled Receptors (GPCRs), some G Protein-Coupled Receptor Kinases (GRKs), and Regulator of G Protein Signaling (RGS)), immune signaling proteins (Src-family kinases, co-receptors and Linker of Activated T-cells (LAT)), Ras proteins and secreted signaling ligands (Resh, 2006). Removing palmitate e.g. by point mutation, disrupts the function of these proteins (O'Dowd et al., 1989). Furthermore, because palmitoylation is dynamically and enzymatically regulated, it is proposed to play a regulatory role in function and signaling (Levental et al., 2010a; Milligan et al., 1995). For example, several GPCRs exhibit turnover in palmitoylation upon activation (Loisel et al., 1999; Mouillac et al., 1992; Resh, 2006) suggesting an active role of palmitoylation in signaling.

Palmitoylation of proteins confers resistance to detergent solubilization, suggesting that this post-translational modification targets proteins to 'lipid rafts' (Levental et al., 2010a). For example in GPCRs lipid raft targeting has been termed

compartmentalization and proposed to influence selectivity of signaling partners by increasing or decreasing interaction probability through confinement to domains (Neubig, 1994; Levitt et al., 2009, 2010). Liquid ordered ($L_o$) or 'raft' targeting of palmitoylated proteins has been confirmed in giant plasma membrane vesicles (GPMVs) (Levental et al., 2010a). Together, this has further fuelled the hypothesis that 'rafts' organize signaling components (Levental et al., 2010b; Lingwood et al., 2009).

In this chapter, we characterize the lateral diffusion of a $\beta_2$AR and two model membrane transmembrane proteins. $\beta_2$AR is has been shown to belong to sphingolipid and cholesterol rich domains, though it is not certain whether their association is the same in each cell type (Allen et al., 2005; Ostrom and Insel, 2004; Ostrom et al., 2001; Rybin et al., 2000). Activation with agonist has been shown to both increase palmitate turnover (Loisel et al., 1999; Mouillac et al., 1992) and decreases receptor association with the raft-phase (Xiang et al., 2002). The second transmembrane protein investigated is a minimal transmembrane domain derived from LAT. T-Cell activation is a raft-dependent process (Simons and Gerl, 2010) and LAT is a doubly palmitoylated protein targeted to the raft phase (Meder et al., 2006). Our construct is composed of the transmembrane domain and the fraction of the C-terminal tail that bears the palmitoylation sites. The third protein is composed of the transmembrane domain of hemagglutinin (B-TMpalm) and its de-palmitoylated variant (B-TM). Hemagglutinin is a raft-dependent protein important to the budding and fusion processes of the influenza virus. B-TMpalm is a truncated form of the hemagglutinin protein and has three palmitoylation sites. It forms a stable dimer (Scolari et al., 2009) for a total of six potential palmitoyl groups per diffuser. This protein was shown to incorporate [$^3$H]-palmitate when expressed in CHO cells and

associates with detergent resistant membranes (Scolari et al., 2009). Furthermore, B-TM was shown to associate with the $L_d$ phase of GUVs and CHO cell GPMVs (Nikolaus et al., 2010).

We hypothesize that palmitoylation alters the diffusion dynamics of transmembrane proteins and propose that this could be a means to modulate protein function. A single point mutation of the acylated cysteine eliminates acylation of the protein, thus yielding otherwise highly similar probes with differential phase associations. Other reasons why palmitoylation could be expected to affect lateral diffusion include the alteration in size, either due increased anchor size of a palmitoylated protein, or because of palmitate-stabilized dimerization (Zheng et al., 2012). Consequently, we investigate probes encompassing a range of sizes from single transmembrane domain to a seven transmembrane receptor. Furthermore, specific interactions with signaling partners may be altered by palmitoylation and could result in altered lateral diffusion (Charollais and Van Der Goot, 2009). To ascertain the general effect of palmitoylation on lateral diffusion we include two minimal model membrane probes that are not expected to interact significantly with protein partners. In the previous chapters we characterized the lateral diffusion of model membrane proteins representing different sizes, modes of anchoring and phase-associations. We found very little evidence of phase-associated differences in the lateral diffusion of these proteins. For example, the confinement of the mobile trajectories showed characteristics that appeared more dependent on the mode of membrane anchoring ($\alpha = 0.5$ for all transmembrane proteins) than putative phase association. However, these probes represent a panel of different characteristics. In this chapter we apply the methods developed in previous chapters to the pairwise comparison

of transmembrane proteins and their non-palmitoylatable point mutants, thus assessing the effect of this important posttranslational modification on the mobility of transmembrane proteins.

## Results and Discussion

### A-TM is not slowed by palmitoylation

Lateral diffusion is quantified as discussed in previous chapters and Materials and Methods. In brief, cells expressing model mEos3.2 labeled proteins were recorded in HEPES imaging buffer. Trajectories of at least 12 steps long were analyzed for single molecule diffusion coefficients ($D_{SM}$). Single molecule α values ($\alpha_{SM}$) were also determined as a measure of anomalous subdiffusion. As in Chapter 4, exposure of cells to laser light are limited to 5000 frames of recording using 561 nm laser, and low TIR illumination of 405 nm light. Selection of cells using 495 nm LED light is similarly limited in duration. Student's t-test is performed, to determine if the diffusion coefficients in the first 1500 frames and last 1500 frames of an experiment are the same.

In Figure 5-1 we present the single molecule diffusion co-efficient ($D_{SM}$) histograms and the single molecule α ($\alpha_{SM}$) histograms of the doubly palmitoylatable single transmembrane domain anchored A-TMpalm mEos3.2 superimposed on its non-palmitoylatable point mutant A-TM mEos3.2. Pooled histograms of $D_{SM}$ retain a similar shape regardless of palmitoylation state. As in Chapter 4, the distribution of $D_{SM}$ values is consistent with two mobile and an immobile population. However, the non-palmitoylated protein appears shifted leftward toward faster values. Previously, we determined that cell-to-cell variability governs the uncertainty in our system. Therefore, we present a

representative diffusion value averaged over multiple cells in place of the pooled histograms. The fastest of the diffusion values is represented in bar chart form. A two-variable student's T-test is used to determine the statistical significance of the differences in the diffusion and confinement values. The difference between A-TM and A-TMpalm are not statistically significant ($p = 0.51$). We can say with higher confidence ($p = 0.91$) that confinement is unaffected by palmitoylation state.

It is striking that the palmitoylated transmembrane protein is not slowed compared to the non-palmitoylated counterpart. This is at odds with our hypothesis that palmitoylation would alter the lateral diffusion of transmembrane proteins. We might have anticipated that lateral diffusion might be slowed due to the effectively larger size of the double palmitoylated anchor compared to the single transmembrane domain, but this is not the case. We cannot rule out that more than one opposing effects are acting on A-TM, for example that the size of the palmitoylated protein may slow diffusion but that membrane heterogeneity facilitates faster movement in a compensatory fashion.

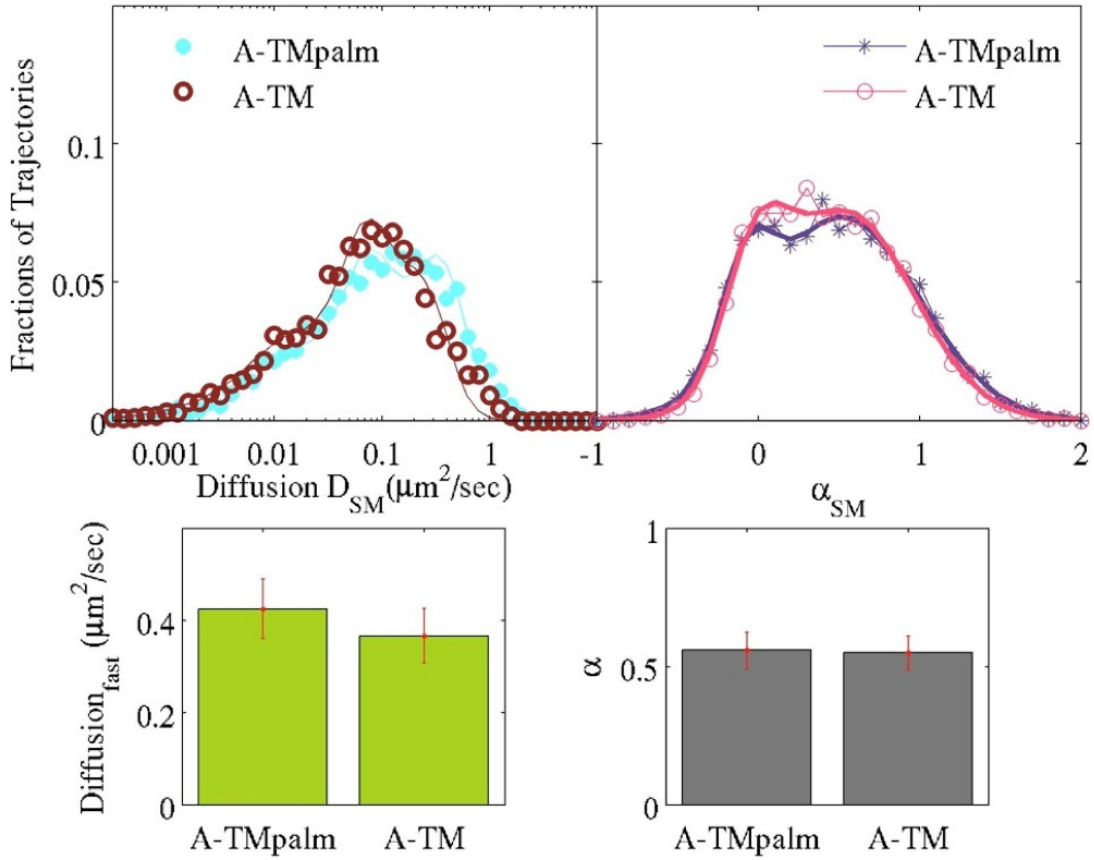


Figure 5-1 Point mutation of palmitoylation sites results in minimal change in lateral diffusion. The shape of histograms of $D_{SM}$ (upper left) and $\alpha_{SM}$ (upper right) are similar whether the wild type or palmitoyl-null version of this transmembrane construct is expressed. The fit diffusion values (fast and slow) are 0.42 ± 0.06 and 0.10 ± 0.02 $\mu m^2$/sec for A-TMpalm, 0.16 ± 0.06 and 0.09 ± 0.01 $\mu m^2$/sec for A-TM, $\alpha$ = 0.56 ± 0.07 for A-TMpalm, $\alpha$ = 0.54 ± 0.06 for A-TM. Only the faster of the mobile fits (lower left) and the mobile $\alpha$ peaks (lower right) are presented in the bar charts. P values are 0.51 for diffusion and 0.91 for $\alpha$. Error bars represent standard error of the mean and values are averaged over 3-5 cells

**Non-palmitoylated $\beta_2$AR is more confined than $\beta_2$AR**

Next we compare the diffusion of the full-length $\beta_2$AR mEos 3.2 with a palmitoylatable cysteine in position 341 and its non-palmitoylated mutant ($\beta_2$AR mut). Similar to A-TM, lateral diffusion of $\beta_2$AR is not slowed by palmitoylation (p = 0.84). The protein belongs to the size regime where diffusion depends weakly on size of the embedded anchor. Previous chapters in this work indicate that even in the event of

dimerization, lateral diffusion should not be substantially affected. Intriguingly, confinement as measured by α appears to be greater for the non-palmitoylated case (p = 0.19). This may be due to changes in interaction between other proteins in the cells such as interacting partners or cytoskeleton.

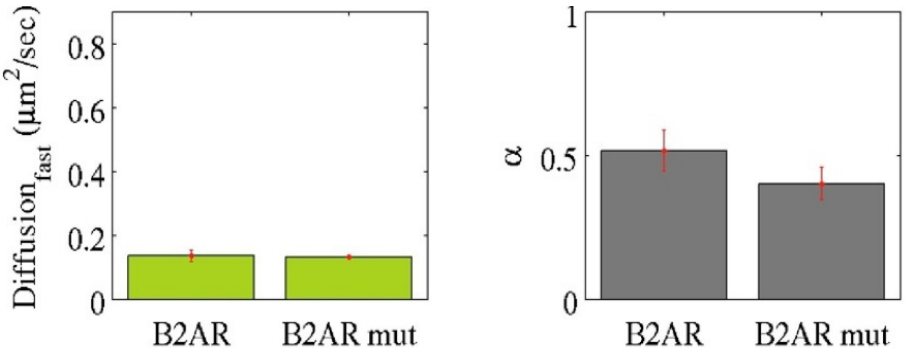


Figure 5-2 Point mutation of palmitoylation sites results in increased confinement of $\beta_2$AR. The fit diffusion values (fast) are 0.14 ± 0.02 $\mu m^2$/sec for $\beta_2$AR, 0.133 ± 0.004 $\mu m^2$/sec for $\beta_2$AR mut, α = 0.52 ± 0.07 for $\beta_2$AR, α = 0.40 ± 0.06 for $\beta_2$AR mut. Each is presented in the bar chart with p value 0.84 for diffusion (left) and 0.19 for α (right). Error bars represent standard error of the mean and values are averaged over 3-5 cells

The capacity to be palmitoylated does not mean that all of the proteins are 100% palmitoylated at all times. This may in part explain the subtlety and cell-to-cell variability that we observe in these experiments. $\beta_2$AR changes palmitoylation state in response to ligand and/or experiences greater turnover in palmitoylation (Loisel et al., 1999; Mouillac et al., 1992), suggesting that in the basal state there are likely both modified and unmodified receptors present. The B-TM construct was derived from a study in which a [$^3$H]-palmitate assay was used to confirm palmitoylation of the protein, though this was also not 100% (Scolari et al., 2009). Furthermore, detergent resistance was conferred for the palmitoylated but not the non-palmitoylated protein. However, the study was conducted in CHO cells, and it is uncertain whether the protein is palmitoylated to the same extent in HeLa cells or would have the same detergent resistance. Studies with

palmitoylated proteins have been successfully conducted in HeLa cells, however, and no evidence of impaired palmitoylation has been found (Galluzzo et al., 2007; Laude and Prior, 2008; Percherancier et al., 2001).

Ostensibly, even with only a fraction of proteins palmitoylated, SPT should enable separate analysis of the proteins. As demonstrated in Chapter 3, SPT accounts well for population heterogeneity. However, in the normoxic experiments, where the distributions are even broader, consistent with three populations of diffusers, and similar cell-to-cell variability, it becomes more challenging to identify small differences between populations of diffusers.

**Difference between B-TM and B-TM palm is insignificant**

B-TM is the variant that has the greatest degree of palmitoylation, with a total of six potential palmitoylation sites per diffuser. As such, it is the anchor with the largest difference in size between palmitoylated and non-palmitoylated variants. In this case the non-palmitoylated variant tends toward being both faster and less confined than the palmitoylated variant, though not with high statistical confidence.

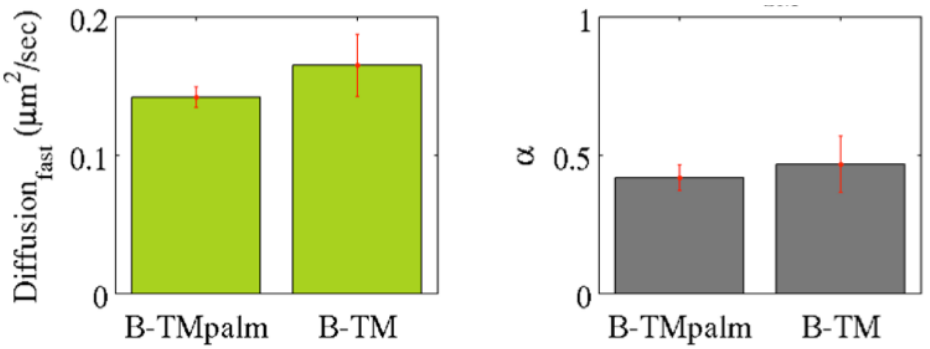


Figure 5-3 - Point mutation of palmitoylation sites results in minimal change in lateral diffusion for B-TM. The fit diffusion values (fast) are 0.142 ± 0.008 μm$^2$/sec for B-TMpalm, 0.16 ± 0.02 μm$^2$/sec for B-TM, α = 0.42 ± 0.05 for B-TMpalm, α = 0.5 ± 0.1 for B-TM. Each is presented in the bar chart with p value 0.26 for diffusion (left) and 0.61 for α (right). Error bars represent standard error of the mean and values are averaged over 4-5 cells.

A previous investigation of full-length hemagglutinin finds a comparable diffusion constant but important structural differences with this study. Hess *et al.* found an ensemble average diffusion constant of 0.09 μm$^2$/sec, which falls between the diffusion constants of the two mobile populations in our data. One of the striking things about their study is that they employed multiple techniques to assess lateral distribution over a range of size scales. They found that hemagglutinin is clustered in fluid structures at a range of sizes from 40 nm to several micrometers. Because of the frame time and the short tracks we can only sample a subset of these structures. Conceivably, B-TM and B-TMpalm might distinguish themselves on a different size scale than what we can access.

Overall, it cannot be said that palmitoylation changes lateral diffusion substantially. In a pairwise comparison, the effect of palmitoylation on lateral diffusion of each construct is subtle and due to the cell-to-cell variability explored in Chapters 3 and 4, requires further iterations to confirm with higher statistical confidence. Furthermore, the trends that are emerging from these three constructs are not consistent. For both A-TM and B-TM it could not be said with statistical confidence that palmitoylation had no

effect on lateral diffusion, but for A-TM the average value for palmitoylated probe was higher and for B-TM it was lower. Confinement is similarly inconclusive. For neither B-TM nor $\beta_2$AR could the confinement be said with statistical confidence to the be the same between palmitoylation states, but for B-TM the average α value for palmitoylated probe is more confined but less confined for $\beta_2$AR. Apparently the effect of palmitoylation on lateral diffusion, therefore, is very subtle.

We have tested the hypothesis that palmitoylation alters diffusion of transmembrane protein. Lateral diffusion is not substantially affected by this modification under these experimental conditions. The second part of the hypothesis, that palmitoylation modulates function of transmembrane proteins through its effect on lateral diffusion is unlikely in light of this data.

It is relatively unexpected that lateral diffusion of transmembrane proteins is so minimally affected by lateral diffusion. As discussed in the introduction, there are multiple reasons to anticipate that the rate of diffusion may change. Among them the change in size to probes either through possible dimerization or directly though change in anchor size, the change in interaction partners (especially for the biologically active $\beta_2$AR) and the change in phase partitioning. It is possible that these may interact in a manner that is too complex to discern from these three examples. Regardless of the reason, palmitoylation does not appear to modulate its effect on transmembrane proteins through changing rates of diffusion under physiological conditions.

**Lateral diffusion at lower temperatures suggest involvement of phases**

Meder *et al*. identified membrane heterogeneity in polarized epithelial cells, but only upon reducing temperature from 37°C to room temperature. According to the critical

model of membrane heterogeneity, lateral lipid structure is expected to be strongly dependent on proximity to the critical point (e.g. temperature). Therefore, reducing the temperature would be hypothesized to increase the size of critical fluctuations, and if the temperature is reduced enough, go to the two-phase coexistence regime. Macroscopic phase-separation does not occur in cells where the cytoskeleton is intact, but we would expect that in the two-phase region any structures such as 'channels' and 'puddles' would be further stabilized and any consequence of phase affinity more pronounced. Therefore we repeated the experiment at a reduced temperature of 23°C and present $D_{SM}$ and $\alpha_{SM}$ bar charts in Figure 5-4.

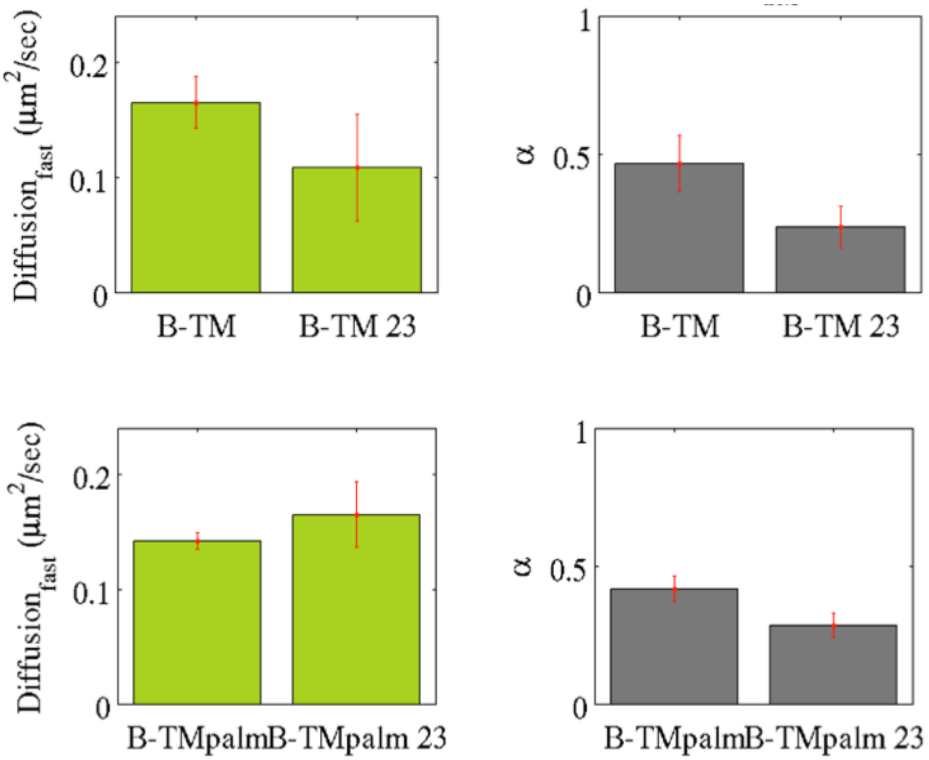


Figure 5-4 Lateral diffusion of B-TM and B-TMpalm responds differently to temperature decrease. Single molecule diffusion D $_{\text{fast population}}$ values for B-TM (upper left: 0.16 ± 0.02 μm$^2$/sec at 37°C and 0.11 ± 0.05 μm$^2$/sec 23°C, p value 0.13) and $\alpha_{\text{mobile population}}$ bar chart for B-TM (upper right) α = 0.5 ± 0.1 at 37°C and α = 0.24 ± 0.07 23°C, p value 0.10). For B-TM palm the same values are presented in for diffusion (lower left: 0.16 ± 0.03 μm$^2$/sec at 23°C and 0.142 ± 0.008 μm$^2$/sec 37°C, p value 0.36) and α (lower right: 0.42 ± 0.05μm$^2$/sec at 37°C and 0.29 ± 0.04 μm$^2$/sec 23°C, p value 0.06). Error bars represent standard error of the mean; values are pooled from 4-5 cells.

Comparing the diffusion of B-TM and B-TMpalm at room temperature, the statistical confidence between their D values increases (p = 0.26 at 37°C and p = 0.16 at 23°C) as well as their alpha values (p = 0.61 at 37°C and p = 0.32 at 23°C). Intriguingly, however, the effect of temperature is reversed between the palmitoylated and non-palmitoylated constructs. In other words, whereas the average value is lower at 23°C than 37°C for B-TM (p = 0.13), this is not the case for B-TMpalm. Diffusion for B-TMpalm is either not changing or increasing at lower temperature (p = 0.36). Diffusion on the micro scale, of course, cannot increase with decreasing temperature. However, the membrane

heterogeneity may be altered by the change in temperature in a way that facilitates diffusion on the time scale for which we measure it (60 to 120 ms).

The temperature decrease also causes diffusion to be more confined for both B-TM and B-TMpalm. Confinement at 37°C is about $\alpha = 0.5$ and about $\alpha = 0.25$ at 23°C for both constructs. The confinement could be due to specific or non-specific interactions with proteins, or possibly affinity with lipid phases. Using comparable probes to ours, Meder *et al.* showed that phase-mediated confinement of non-raft probes as measured by the fraction recovery by fluorescence recovery after photobleaching method (Meder et al., 2006). What implicated phase partitioning in the FRAP study was the complete recovery at 37°C of probes that were completely confined at 23°C, and the fact that this behavior was correlated with phase-association of their probes. Therefore confinement of non-raft probes as measured by this group was total, likely corresponding to the immobile rather than the mobile fraction in the current study. The transmembrane domains in this study do not show a similar response to temperature, with no change in the immobile fraction between the two temperatures. In part the difference may be attributed to polarized epithelial cells having unusual compositions, with much higher concentrations of cholesterol and raft phase in the apical membrane than either the basolateral membrane or the plasma membranes of most cells. The same confinement was not found in fibroblasts in the FRAP study (Meder et al., 2006). Most likely, confinement of the mobile peak is related to interactions with protein through specific affinity or due to diffusion obstacles.

While confinement was different between 37°C and 23°C, the difference between palmitoylated and non-palmitoylated probes were much less pronounced. This is despite

opposing phase-associations in detergent resistant membranes (DRMs) and vesicles is that affinity to raft phase at low temperatures does not necessarily correlate with degree of 'raft' behavior at higher temperatures. Eggeling *et al.* have interpreted lateral diffusion of a number of putative raft and non-raft probes and established that raft proteins exhibited cholesterol dependent 'transient trapping' (10 ms) in their diffusion in regions under 20 nm in size (Eggeling et al., 2009). In a follow-up study they tested transient trapping against the degree of phase association in giant plasma membrane vesicles (GPMVs) and giant unilamellar vesicles (GUVs) and found that degree of phase-association is not a predictor of transient trapping (Sezgin et al., 2012). Furthermore, complexity of the membrane decreases apparent phase-preference. Probes that are clearly phase-separated in synthetic GUV are less clearly phase separated in GPMVs (Nikolaus et al., 2010; Sezgin et al., 2012) and the plasma membrane is more complex still. Thus perhaps association of B-TMpalm with detergent resistant membranes or B-TM with the $L_d$ phase of a vesicle may not translate to similar phase-affinity at 23°C and 37°C in our experiment.

**Membrane composition of HeLa cells may be different from other cells.**

Previous studies have found substantial differences and diffusion constants between cell lines, as high as twofold (Kenworthy et al., 2004). In Figure 5-5 diffusion of $\beta_2$AR in HeLa cells is compared with that of CHO cells, to investigate whether HeLa cells might have a different membrane composition. Overall our data suggest that phase heterogeneity may be present in cells and that palmitoylation changes the way proteins interact with the membrane. However, whatever effect this has on lateral diffusion appears subtle at physiological temperatures. Membrane heterogeneity is sensitive to both

temperature and membrane composition (Veatch, 2004). It is possible that the membrane composition in HeLa cells is different from many other cells, resulting in smaller than average effect on lateral diffusion at physiological temperatures whereas other cells may show more robust effect of palmitoylation. This is a possibility that warrants investigation. As a preliminary indication of whether membrane composition and/or heterogeneity may be different in different cell lines, we compare lateral diffusion of $\beta_2$AR expressed in CHO cells and HeLa cells (Figure 5-5).

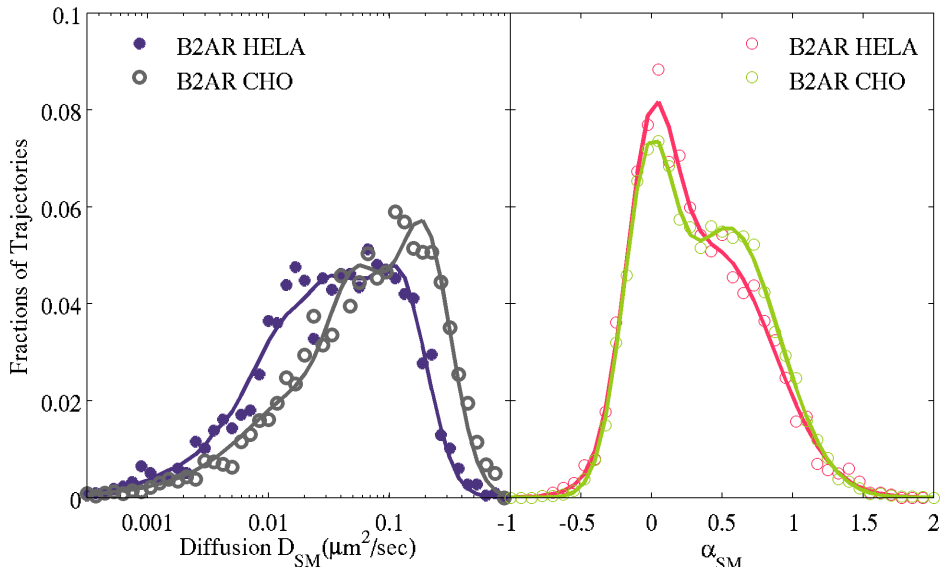


Figure 5-5 Diffusion of $\beta_2$AR in the membranes of HeLa and CHO cells suggest that membrane properties are different. Diffusion constants for $\beta_2$AR in CHO cells is 0.198 ± 0.002 μm$^2$/sec for the fast population, 0.049 ± 0.001 μm$^2$/sec for the slower population, where errorbounds are standard errors of the mean. In contrast, the diffusion values in HeLa cells are 0.14 ± 0.02 μm$^2$/sec for the faster population, and 0.04 ± 0.01 μm$^2$/sec for the slower. $\alpha$ = 0.54 ± 0.03 for CHO and $\alpha$ = 0.52 ± 0.07 for HeLa.

We find substantial differences in the diffusion constants determined in these two cell lines. In HeLa cells the fast population diffuses at 0.14 ± 0.02 μm$^2$/sec, whereas in CHO cells they diffuse at almost 0.2 μm$^2$/sec. However, population $\alpha$ values are similar between the cell lines, indicating that sources of confinement or heterogeneity such as cytoskeleton and protein obstacles are similar between the cells. This suggests that the

membrane composition between these cell lines may be substantially different. Consistent with this, GPMVs extracted from HeLa cells behave differently from those extracted from RBL cells. Using N-Ethylmaleimide as the active blebbing agent (see materials and methods), the transition temperature appears to be lower than RBLs. In fact, phase-separation of HeLa GPMVs could not be reliably achieved (data not shown, experiment by Jing Wu) whereas RBL GPMVs exhibit transition temperatures between 15 and 21°C (e.g. see Figure 4-10). In contrast, phase separated GPMVs from RBL cells have been visualized using the NEM approach (Levental et al., 2010a). This warrants investigation into how palmitoylation can affect lateral diffusion of palmitoylated and non-palmitoylated probes in other cell lines.

Given the apparent involvement of phases in lateral diffusion (at lower temperatures), one challenge in conducting this experiment is the uncertainty in predicting what structure should arise in a heterogeneous membrane. The size of such structure should determine the imaging protocol and the choice of label. A structure mirroring the shape of cytoskeleton has been proposed (Machta et al., 2011), but incorporates the uncertain assumption that cytoskeleton-coupling proteins have a single phase-preference. In the event that, for example, either phase can be coupled to cytoskeleton, lipid heterogeneity could take on a variety of unpredictable forms. Perhaps something like that observed by Hess *et al.* who characterized fluid HA-enriched domains of variable sizes with jagged edges. Their observations are entirely consistent with both phase-preference and stabilized critical fluctuations, and inconsistent with phase separation. The structures they detected ranged from 40 nm to several microns in size. Phase-mediated confinement of membrane probes occurs when a protein preferring

one phase interacts with the non-preferred phase or its boundary and changes its lateral diffusion due to the propensity to retreat to the preferred phase. If the areas covered by a preferred phase are as big as described by Hess *et al*, and are sometimes or coexisting with domains of a much smaller size such as in Machta et al, it is not obvious how a single particle tracking experiment should be designed to best capture the effect of membrane structure on diffusion.

## Conclusion

In this chapter we characterize the diffusion of three transmembrane constructs ($\beta_2$AR, A-TMpalm, and B-TMpalm) and their palmitoyl-null mutants ($\beta_2$AR mut, A-TM, and B-TM). Contrary to our predictions robust differences in lateral diffusion between palmitoylated and non-palmitoylated variants of the transmembrane proteins are not identified, indicating that palmitoylation does not affect the function of proteins by modulating the rate of their lateral diffusion. The temperature is decreased to test the role of phases in the lateral diffusion the B-TM/palm protein pair. The reduced temperature exaggerates the difference between the construct pair. Intriguingly, palmitoylation appears to reverse or reduce the effect of temperature on the lateral diffusion of this construct. While these data suggest the involvement of lipid phases in lateral diffusion, further investigation is required to confirm the statistical significance of these findings and reproducibility across cell lines.

## Works Cited


Allen, J.A., Yu, J.Z., Donati, R.J., and Rasenick, M.M. (2005). β-Adrenergic Receptor Stimulation Promotes Gαs Internalization through Lipid Rafts: A Study in Living Cells. Mol. Pharmacol. *67*, 1493–1504.

Charollais, J., and Van Der Goot, F.G. (2009). Palmitoylation of membrane proteins (Review). Mol Membr Biol *26*, 55–66.

Eggeling, C., Ringemann, C., Medda, R., Schwarzmann, G., Sandhoff, K., Polyakova, S., Belov, V.N., Hein, B., von Middendorff, C., Schonle, A., et al. (2009). Direct observation of the nanoscale dynamics of membrane lipids in a living cell. Nature *457*, 1159–1162.

Galluzzo, P., Caiazza, F., Moreno, S., and Marino, M. (2007). Role of ER palmitoylation in the inhibition of human colon cancer cell proliferation. Endocr. Relat. Cancer *14*, 153–167.

Kenworthy, A.K., Nichols, B.J., Remmert, C.L., Hendrix, G.M., Kumar, M., Zimmerberg, J., and Lippincott-Schwartz, J. (2004). Dynamics of putative raft-associated proteins at the cell surface. J Cell Biol *165*, 735–746.

Laude, A.J., and Prior, I.A. (2008). Palmitoylation and localisation of RAS isoforms are modulated by the hypervariable linker domain. J. Cell Sci. *121*, 421–427.

Levental, I., Lingwood, D., Grzybek, M., Coskun, U., and Simons, K. (2010a). Palmitoylation regulates raft affinity for the majority of integral raft proteins. Proc Natl Acad Sci U A *107*, 22050–22054.

Levental, I., Grzybek, M., and Simons, K. (2010b). Greasing their way: lipid modifications determine protein association with membrane rafts. Biochemistry (Mosc.) *49*, 6305–6316.

Levitt, E.S., Clark, M.J., Jenkins, P.M., Martens, J.R., and Traynor, J.R. (2009). Differential effect of membrane cholesterol removal on mu- and delta-opioid receptors: a parallel comparison of acute and chronic signaling to adenylyl cyclase. J Biol Chem *284*, 22108–22122.

Levitt, E.S., Purington, L.C., and Traynor, J.R. (2010). Gi/o-coupled receptors compete for signaling to adenylyl cyclase in SH-SY5Y cells and reduce opioid-mediated cAMP overshoot. Mol Pharmacol.

Lingwood, D., Kaiser, H.J., Levental, I., and Simons, K. (2009). Lipid rafts as functional heterogeneity in cell membranes. Biochem Soc Trans *37*, 955–960.

Loisel, T.P., Ansanay, H., Adam, L., Marullo, S., Seifert, R., Lagace, M., and Bouvier, M. (1999). Activation of the beta(2)-adrenergic receptor-Galpha(s) complex leads to

rapid depalmitoylation and inhibition of repalmitoylation of both the receptor and Galpha(s). J Biol Chem *274*, 31014–31019.

Machta, B.B., Papanikolaou, S., Sethna, J.P., and Veatch, S.L. (2011). Minimal model of plasma membrane heterogeneity requires coupling cortical actin to criticality. Biophys J *100*, 1668–1677.

Meder, D., Moreno, M.J., Verkade, P., Vaz, W.L.C., and Simons, K. (2006). Phase coexistence and connectivity in the apical membrane of polarized epithelial cells. Proc. Natl. Acad. Sci. U. S. A. *103*, 329–334.

Milligan, G., Parenti, M., and Magee, A.I. (1995). The dynamic role of palmitoylation in signal transduction. Trends Biochem Sci *20*, 181–187.

Mouillac, B., Caron, M., Bonin, H., Dennis, M., and Bouvier, M. (1992). Agonist-modulated palmitoylation of beta 2-adrenergic receptor in Sf9 cells. J Biol Chem *267*, 21733–21737.

Neubig, R.R. (1994). Membrane organization in G-protein mechanisms. FASEB J *8*, 939–946.

Nikolaus, J., Scolari, S., Bayraktarov, E., Jungnick, N., Engel, S., Plazzo, A.P., Stockl, M., Volkmer, R., Veit, M., and Herrmann, A. (2010). Hemagglutinin of Influenza Virus Partitions into the Nonraft Domain of Model Membranes. Biophys. J. *99*, 489–498.

O'Dowd, B.F., Hnatowich, M., Caron, M.G., Lefkowitz, R.J., and Bouvier, M. (1989). Palmitoylation of the human beta 2-adrenergic receptor. Mutation of Cys341 in the carboxyl tail leads to an uncoupled nonpalmitoylated form of the receptor. J Biol Chem *264*, 7564–7569.

Ostrom, R.S., and Insel, P.A. (2004). The evolving role of lipid rafts and caveolae in G protein-coupled receptor signaling: implications for molecular pharmacology. Br. J. Pharmacol. *143*, 235–245.

Ostrom, R.S., Gregorian, C., Drenan, R.M., Xiang, Y., Regan, J.W., and Insel, P.A. (2001). Receptor Number and Caveolar Co-localization Determine Receptor Coupling Efficiency to Adenylyl Cyclase. J. Biol. Chem. *276*, 42063–42069.

Percherancier, Y., Planchenault, T., Valenzuela-Fernandez, A., Virelizier, J.-L., Arenzana-Seisdedos, F., and Bachelerie, F. (2001). Palmitoylation-dependent Control of Degradation, Life Span, and Membrane Expression of the CCR5 Receptor. J. Biol. Chem. *276*, 31936–31944.

Resh, M.D. (1999). Fatty acylation of proteins: new insights into membrane targeting of myristoylated and palmitoylated proteins. Biochim. Biophys. Acta BBA - Mol. Cell Res. *1451*, 1–16.

Resh, M.D. (2006). Palmitoylation of ligands, receptors, and intracellular signaling molecules. Sci. Signal. *2006*, re14.

Rybin, V.O., Xu, X., Lisanti, M.P., and Steinberg, S.F. (2000). Differential targeting of beta -adrenergic receptor subtypes and adenylyl cyclase to cardiomyocyte caveolae. A mechanism to functionally regulate the cAMP signaling pathway. J. Biol. Chem. *275*, 41447–41457.

Scolari, S., Engel, S., Krebs, N., Plazzo, A.P., De Almeida, R.F., Prieto, M., Veit, M., and Herrmann, A. (2009). Lateral distribution of the transmembrane domain of influenza virus hemagglutinin revealed by time-resolved fluorescence imaging. J Biol Chem *284*, 15708–15716.

Sezgin, E., Levental, I., Grzybek, M., Schwarzmann, G., Mueller, V., Honigmann, A., Belov, V.N., Eggeling, C., Coskun, U., Simons, K., et al. (2012). Partitioning, diffusion, and ligand binding of raft lipid analogs in model and cellular plasma membranes. Biochim Biophys Acta *1818*, 1777–1784.

Simons, K., and Gerl, M.J. (2010). Revitalizing membrane rafts: new tools and insights. Nat Rev Mol Cell Biol *11*, 688–699.

Veatch, S. (2004). Liquid Immiscibility in Model Bilayer Lipid Membrane. University of Washington.

Xiang, Y., Rybin, V.O., Steinberg, S.F., and Kobilka, B. (2002). Caveolar localization dictates physiologic signaling of beta 2-adrenoceptors in neonatal cardiac myocytes. J Biol Chem *277*, 34280–34286.

Zheng, H., Pearsall, E.A., Hurst, D.P., Zhang, Y.H., Chu, J., Zhou, Y.L., Reggio, P.H., Loh, H.H., and Law, P.Y. (2012). Palmitoylation and membrane cholesterol stabilize mu-opioid receptor homodimerization and G protein coupling. Bmc Cell Biol. *13*.

# Chapter 6

# Future directions and conclusions

## Summary of conclusions

The motivation for this work was to determine the effect of palmitoylation on the lateral diffusion of transmembrane proteins. We hypothesized that palmitoylation affects the diffusion dynamics of transmembrane proteins and propose that this could be a means to modulate protein function. We developed a method to compare simulated Brownian diffusion to experimentally determined trajectories in order to fit diffusion parameters and identify population heterogeneity from short trajectories. Using this method, we characterized the effect of multiple parameters on lateral diffusion. The main conclusions are summarized below.

In Chapter 3, we determined that size-dependence of diffusion is high for small anchors in hypoxic cells. Therefore, oligomerization slows lateral diffusion of single transmembrane or lipid anchored proteins, but larger proteins much less so, consistent with our experimental findings. The temperature-dependence of diffusion was high. Inherent cell-to-cell variability was also demonstrated and was relatively low. We developed a method to determine diffusion constants and identify heterogeneities in diffusion. Lateral diffusion of model membrane proteins was reproducibly Brownian for

all constructs, including β2 adrenergic receptor, with a single population of mobile diffusers for all but one construct.

In Chapter 4, we found that buffer conditions affect lateral diffusion and heterogeneity, which we attribute to hypoxia. Under normoxic conditions we again found that size-dependence of diffusion is high for small probes, but determined that temperature dependence of lateral diffusion was not as high as under hypoxic conditions. We also found that phototoxicity must be carefully considered under the illumination conditions required for mEos imaging. We modified the simulation-coupled analysis method developed in Chapter 3 to account for a more complex diffusion profile, which was consistent with two mobile populations and an immobile population of particles. Normoxic conditions were found to better represent physiological conditions and were used for subsequent experiments.

In Chapter 5, we test the effect of palmitoylation on the lateral diffusion of three transmembrane proteins. At physiological temperatures, differences found had low statistical significance between the palmitoyl-null mutant and its palmitoylatable counterpart. At physiological temperatures in HeLa cells, therefore, palmitoylation is unlikely to modulate function of membrane proteins through lateral diffusion. Decreasing temperature, however, revealed an interesting discrepancy in the response of palmitoylated and non-palmitoylated B-TM to temperature. Perhaps the temperature range over which palmitoylated and non-palmitoylated probes distinguish themselves varies by cell type, and may occur at physiological temperatures in some cells. This warrants further investigation into the effect of palmitoylation in other cell types.

## Strengths of SPT

The foremost strength of SPT is to monitor changes in interactions or other changes in lateral diffusion that exceed ~10%. This encompasses large rearrangements and biological events in particular. This study points to the continued need to investigate the nature of phase heterogeneity. SPT is a powerful tool for the investigation of membrane heterogeneity, but the dynamic and elusive nature of phase structure introduces a handful of specialized challenges to SPT experiments. Some of these are discussed below.

Diffusion and membrane heterogeneity studies point to the role of lipid phases in recruiting protein components to domains of protein- or surface-stabilized structure (Hess et al., 2006; Pinaud et al., 2009; Pyenta et al., 2001, 2003; Shelby et al., 2013; Zhao et al., 2013). Many of these involve proteins that have been clustered by antigens during signaling or by artificial means, and so have a defined and stable structure which in turn stabilize lipid domains (see Figure 6-1 C reprinted from the Introduction.) Once a diffusing probe enters such an area it is slowed down (Pinaud et al., 2009) and consequently confined due to the high density of proteins. The same does not appear to be true in the absence of clustering for the sorts of simple model membrane proteins that were investigated in this study (Kenworthy et al., 2004; Lommerse et al., 2006, Chapter 4), except in special cases such as polarized epithelial cells (Meder et al., 2006). This may suggest that phase-mediated structure is smaller than the detection limit. On the other hand, it may suggest that larger clusters of proteins with phase preference must be clustered in order to stabilize appreciable lipid structure, in the manner of stabilized critical fluctuations. Indeed, looking at smaller and smaller scales has not, as the field

predicted, revealed the elusive raft, but rather has shown smaller heterogeneities that sometimes do and sometimes don't correlate with phase preference (Sezgin et al., 2012). Maybe chasing ever smaller size scales is not the answer, but rather focusing on the large rearrangements and biological events for which criticality has been proposed to be important, and rely on perturbations such as those that are emerging in recent work (Gray et al., 2013).

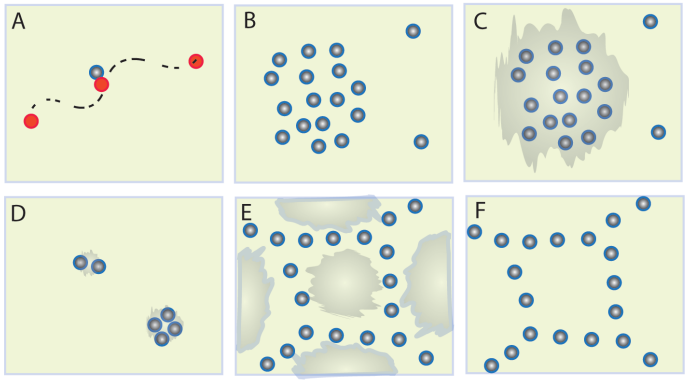


Figure 6-1 Schematic of contemporary descriptions of membrane heterogeneity reprinted from introduction. The circles are proteins, grey represents lipid phases (E.g. $L_o$), and green is the lipid bilayer. Not drawn to scale. (A) Stable or transient nanoclusters of 2-4 proteins whose associations are cholesterol dependent. (B) Protein cluster with an affinity for a lipid phase such as in co-patching studies or T-Cell and B-Cell signaling. This type of structure may vary greatly in size. (C) Clusters of proteins that allow hindered diffusion through them. Alternatively, dense but homogenously distributed immobile proteins can also cause anomalous subdiffusion. (D) Transient trapping in which specific and sometimes cholesterol dependent interactions with proteins occur. Eggeling et al. describe these as 10-20 ms in length and in regions less than 20 nm in size. (E) Associated with the Kusumi group, cytoskeletal corrals are obstacles that result in proposed 'hop-diffusion'. (F) 'Critical model' in which pinning proteins (blue) couple cortical actin to one of two liquid phases in the membrane, resulting in stabilized critical fluctuations possibly organized into entrained channels and puddles and mirroring the cytoskeleton. Depictions of outright phase separation, as observed in Meder et al. and hypothesized cytoskeletal aster structures from the Mayor group have been omitted from this schematic.

Focusing on rearrangements and protein-stabilized domains, furthermore, means being able to confirm the anticipated size of domains by complementary means (like non-super resolution imaging or cross correlation) and test diffusion of phase-preferring probes using SPT. A defined size helps to design and interpret the SPT experiment. The resolution of SPT is high; for our experiments using mEos proteins, it is as high as 30

nm. However, since phases themselves aren't labeled, their structure must be inferred indirectly, which requires the movement of probes. The size of structures that can be detected by such movement is dependent on the diffusion constant of the probe, the frame rate at which it is recorded, and the model against which it is interpreted. As discussed in Chapters 3 and 4, in one frame, even the slowest probes are displaced by approximately 120 nm. In our case, the short-term diffusion constant is determined from frames 2 to 4, and so the diffusion constant is determined from an even bigger displacement. Furthermore, we assign one D and one α value to each single molecule trajectory, so transient changes that occur on a timescale faster than the length of a trajectory, is lost to averaging over all steps in that trajectory. One approach to access information below the step size in our system is to extrapolate mean squared displacement to t = 0. For Brownian motion, at t = 0 the displacement should also be zero, but in an experimental context, the intercept will be larger due to localization error and confinement to structures below our lower detection limit. For data presented in Chapter 3, no confinement above the localization error was detected, but this is an unexplored avenue for the more confined data presented in Chapters 4 and 5. The upper limit of detection is defined by the area explored by the probe before photobleaching, which relates to both the photostability of the label, its rate of diffusion, and its confinement. Effectively, the time / space window over which information is gathered is fairly narrow. To an extent this window can be adjusted, by selecting the frame rate or imaging equipment, the brightness and photostability of the probe, the diffusing speed of the probe, the model to be interpreted etc. However, to get this combination right, either the size of the structure under investigation must be well defined, or perhaps a wide range of these factors tested.

The premise that SPT can reveal phase-mediated membrane heterogeneity in plasma membranes depends on one fundamental assumption: that the affinity of probes to their phases (or the penalty associated with being in the opposing phase) is high enough to detectably affect lateral diffusion. It is not clear that this assumption is justified. In the Monte Carlo simulation, Michael Saxton showed that for corrals to impose demonstrable confinement on a diffusing entity, the escape probability of that entity out of the corral had to be 10% or lower (Saxton, 1995). It is not clear whether the phase preference could impose an escape probability that low. Perhaps only when lipids are clustered together with protein obstacles will confinement result from phase association. The limit of phase-mediated confinement might best be defined in phase separated GUV or GPMV membranes, and represent the future direction. To an extent this has already been done, e.g. by Skaug et al. who used a phase-separated gel-liquid composition to extract an upper limit for α of ~0.6 (Skaug et al., 2011). In cells the opposing phase is expected to be more permeable to probes than gel, or even a phase-separated liquid domain. The exception is outright liquid-liquid phase separation, which does appear to be sufficient to impart total confinement on $L_d$ probes (Meder et al., 2006), perhaps through the additional involvement of cytoskeleton. The $\alpha \sim 0.6$ value from Skaug et al. represents confinement from impermeable and fairly large obstacles in a percolating phase. How does this value change by altering imaging conditions? How does it change with the size of the obstacles and their density? Can an imaging set-up be so well calibrated with respect to these factors that extracting parameters such as diffusion constant and α values from an unknown cellular structure is sufficient to delineate the contribution of multiple different types of obstacles?

For the above state reasons, in this author's opinion the most fruitful application of SPT studies of lipid phases in facilitating membrane events would be to focus on protein-stabilized aggregated lipid domains, whose size can be independently verified.

## Future directions in investigating phase behavior in cells

In our experiments phase heterogeneity did not prove to be a definitive modulator of lateral diffusion of palmitoylated proteins or other constructs at 37°C. This is contrary to some but not all observations made previously (Kenworthy et al., 2004; Lommerse et al., 2006; Meder et al., 2006). One reason for the discrepancy between studies may be different membrane composition among cell lines. In support of cell line differences, we find that lateral diffusion of HeLa cells and CHO cells are different. Furthermore, GPMVs extracted from HeLa cells by the NEM protocol (see Materials and Methods) appear to have lower transition temperatures than RBL GPMVs. Within the context of the hypothesized phase diagram of plasma membranes, perhaps HeLa cells are poised further above the critical point than RBL cells, or not critical. Investigating the lateral diffusion of the subset of the investigated probes in RBL cells and testing critical perturbations on them is a pending future direction.

It is also possible that GPMVs are not representative of membrane behavior in cells. GPMVs have been extremely useful for studying the biophysics of the membrane. They have more complex compositions and are often more appropriate as model membrane systems than GUVs, which often contain only three lipid components (Sezgin et al., 2012). This is evidenced by more distinct phase-association phenotypes in GUVs

than GPMVs (Nikolaus et al., 2010; Sezgin et al., 2012). However, the data presented in Chapter 4, suggests that relatively rapid changes can occur to membrane compositions in response to stress. It is not unlikely that reactive oxygen species might be generated during GPMV formation, and blebs generated during phototoxicity have similarities to GPMVs too. The transition temperatures of GPMVs generated by different protocols can vary, suggesting that the compositions are different. Thus, confirmation of phase behavior in plasma membranes extracted by other methods, such as alternative GPMV protocols or extraction methods might be prudent.

One alternative model membrane might be to employ the footprints of de-roofed cells. These can be generated by culturing cells on poly-D-lysine coated glass and mechanically removing all but their bottom membranes by sonication (Wu et al., 2010) or application of ice-cold water (Bezrukov et al., 2009). I find that for HeLa cells, no poly-D-lysine is necessary and cold buffer is sufficient to de-roof many cells. One advantage of this approach is that the extraction is mechanical and therefore the membrane has very little opportunity to be chemically altered as a result of extraction. Staining the footprints (or cells prior to de-roofing) in the same fashion as GPMVs and subjecting them to the same temperature controls, could in principle show phase separation and give indication of $L_o$ and $L_d$ fractions. Generating these could potentially be a simple way to directly compare phase fractions in different cells, in the absence of cytoskeletal restraints and the complexity of the cell. Alternatively, latrunculin could be applied to induce blebbing and the temperature reduced to observe phase-separation of the emerging blebs.

## Future directions for SPT

Any future effort to perform single particle imaging, must take into account the potential for phototoxicity. Experiments using the mEos label might benefit from identifying cells that are less sensitive to phototoxic damage. Alternatively, replacing mEos with a label excitable at higher wavelengths may circumvent phototoxic damage, as the literature suggests that live cells tolerate redder wavelengths better (Hoebe et al., 2007; Carlton, 2013). Experimenting with incorporating antioxidants into the imaging conditions may extend the experimental time-window even at lower wavelengths by mimicking oxidative protection pathways in the cell. For example, pretreating cells with α tocopherol may counteract some phototoxic damage during imaging, or one of the many other more water-soluble antioxidants.

SPT for inferring membrane heterogeneity has inherent challenges, as explored in the section 'Strengths of SPT'. However, SPT is a very sensitive method to investigate dynamic populations of diffusers. Conceivably, the role of criticality in facilitating biological events may best be studied using functional outputs of signaling molecules. One such system could be epidermal growth factor receptor (EGFR). EGFRs have been associated with lipid rafts, and their raft localization correlated with drug resistance in cancer aggression (Irwin et al., 2011). Additionally, EGFR undergoes a requisite dimerization event during its activation, and is a single transmembrane protein. We know from Chapter 3 and 4 that in normoxic and hypoxic conditions, single transmembrane protein dimerization results in slower diffusion and thus a detectable response to activation. Thus, single particle diffusion may be used as a complementary functional assay to other functional assays. This could be a very interesting target to which to apply

critical perturbations such as hexadecanol and octanol to test the role of criticality specifically in the function of this receptor, because of its important implications in cancer (Hoogsteen et al., 2012; Misra et al., 2012) and previous correlation with lipid rafts (Irwin et al., 2011).

## Future directions in hypoxia

The effect of hypoxia on cells is complicated. Paradoxically, hypoxic damage is related to (re-)oxidative damage, and to phototoxicity. Reactive oxygen species are implicated in all of these. This poses the question whether too much oxygen may be just as consequential to lateral diffusion as hypoxic conditions. As noted in Chapter 4, 160 mmHg under normobaric conditions are no more physiologically accurate than is hypoxia. What might be the effect on lateral diffusion phenotypes should the percentage oxygen in the sample be varied in a controlled fashion? Potentially, this could have important consequences to all manner of cellular studies, which are typically conducted under atmospheric oxygen conditions.

Another question that arises is whether the lateral diffusion phenotype is merely a consequence of hypoxic conditions or also contributes to the cellular damage and the pathologies with which hypoxia is associated. For example does the unrestricted lateral diffusion of EGFR relate to its activation during hypoxia and the aggression, and treatment-resistance of solid tumors? Or is hypoxic upregulation of various HIFα regulated genes the exclusive cause of aggressiveness? In Chapter 4, we showed that membrane composition changes in response to hypoxic buffer, as measured by a GPMV assay, and as mentioned above, activity of EGFR has been correlated with phase-

association. This begs the question; what is the role of lipid in facilitating hypoxic activation? Assays such as boronate based probes for optical detection of hydrogen peroxide and other reactive oxygen species may be a useful methodology to help answer this question, with or without simultaneous SPT, to complement traditional biochemical studies.

Determining what the reason for the hypoxic phenotype is represents another important future pursuit. In part this is because the lateral diffusion phenotype might be important to hypoxic disease states and in part because hypoxic cells may be a useful model membrane system in which most cellular features are intact. Cytoskeletal connections are not all disrupted in the hypoxic imaging buffer, or we would see bleb formation and possibly macroscopic phase separation at the lower temperatures. However, our data and the literature suggest that connections to the cytoskeleton are in some way impaired. In hypoxia of liver tissue, reversible blebbing does occur (Lemasters et al., 1983). Is it the buffer that is causing our cells not to bleb even under hypoxic conditions? Would we see the same effect if hypobaric oxygen were applied to HeLa cells? I hypothesize, that only a subset of connections to cortical actin are disrupted under hypoxic conditions. Imaging using fluorescent labels for the cytoskeleton (such as phalloidin or LifeAct) would show whether actin density is impaired. Complementary imaging of actin and membrane binding proteins such as the ezrin-radixin-moesin (ERM) family would show whether a subset of these are displaced by hypoxic conditions. Ezrin in particular has been implicated in the stabilization of lipid rafts (Gupta et al., 2006) and so would be hypothesized to be affected by changes in lipid composition such as we witnessed in Chapter 4.

Another aspect of the biology of hypoxia is ATP depletion. It would also be interesting to determine whether ATP depletion is involved in the lateral diffusion phenotype that we observed in Chapter 3, and over what time scale ATP depletion occurs. Several groups have implicated ATP-dependent processes as involved in the temperature dependence of diffusion (Di Rienzo et al., 2013; Sunyer et al., 2009; Weber et al., 2012), while others have implicated ATP-dependent cytoskeletal dynamics and clustering of GPI proteins (Chaudhuri et al., 2011). Under hypoxic conditions, we see both a much higher dependence on temperature and a more homogenous lateral diffusion of multiple proteins, including GPI anchor. This warrants ATP-depletion experiments using sodium azide and 2-deoxy glucose, or cyanide to determine if this perturbation reproduces the fast and homogenous phenotype.

## Summary of significance

This project developed a treatment of single trajectory analysis that will be useful in future SPT studies in both simple Brownian contexts and more complex environments. Several important parameters were characterized including size, temperature-dependence, choice of label, and oxygenation in their effect on lateral diffusion. These are important to understanding the effective limits of detection in cells, which have inherent cell-to-cell variability. Furthermore, the strong size-dependence of lateral diffusion for smaller probes suggests that dimerization of single transmembrane and lipid-anchored probes could be a means of modulating diffusion constants *in vivo.* Finally, we show that under physiological conditions in HeLa cells, the ability of proteins to be palmitoylated does not change protein function through modulation of lateral diffusion.

## Works Cited


Bezrukov, L., Blank, P.S., Polozov, I.V., and Zimmerberg, J. (2009). An adhesion-based method for plasma membrane isolation: evaluating cholesterol extraction from cells and their membranes. Anal. Biochem. *394*, 171–176.

Carlton, P.M. (2013). Artifacts of light. Nat. Methods *10*, 1135–1135.

Chaudhuri, A., Bhattacharya, B., Gowrishankar, K., Mayor, S., and Rao, M. (2011). Spatiotemporal regulation of chemical reactions by active cytoskeletal remodeling. Proc. Natl. Acad. Sci. *108*, 14825–14830.

Gray, E., Karslake, J., Machta, B.B., and Veatch, S.L. (2013). Liquid general anesthetics lower critical temperatures in plasma membrane vesicles. Biophys. J. *105*, 2751–2759.

Gupta, N., Wollscheid, B., Watts, J.D., Scheer, B., Aebersold, R., and DeFranco, A.L. (2006). Quantitative proteomic analysis of B cell lipid rafts reveals that ezrin regulates antigen receptor–mediated lipid raft dynamics. Nat. Immunol. *7*, 625–633.

Hess, S.T., Girirajan, T.P., and Mason, M.D. (2006). Ultra-high resolution imaging by fluorescence photoactivation localization microscopy. Biophys J *91*, 4258–4272.

Hoebe, R.A., Van Oven, C.H., Gadella, T.W., Dhonukshe, P.B., Van Noorden, C.J.F., and Manders, E.M.M. (2007). Controlled light-exposure microscopy reduces photobleaching and phototoxicity in fluorescence live-cell imaging. Nat. Biotechnol. *25*, 249–253.

Hoogsteen, I.J., Marres, H.A.M., van den Hoogen, F.J.A., Rijken, P.F.J.W., Lok, J., Bussink, J., and Kaanders, J.H.A.M. (2012). Expression of EGFR under tumor hypoxia: identification of a subpopulation of tumor cells responsible for aggressiveness and treatment resistance. Int. J. Radiat. Oncol. Biol. Phys. *84*, 807–814.

Irwin, M.E., Mueller, K.L., Bohin, N., Ge, Y., and Boerner, J.L. (2011). Lipid raft localization of EGFR alters the response of cancer cells to the EGFR tyrosine kinase inhibitor gefitinib. J. Cell. Physiol. *226*, 2316–2328.

Kenworthy, A.K., Nichols, B.J., Remmert, C.L., Hendrix, G.M., Kumar, M., Zimmerberg, J., and Lippincott-Schwartz, J. (2004). Dynamics of putative raft-associated proteins at the cell surface. J Cell Biol *165*, 735–746.

Lemasters, J.J., Stemkowski, C.J., Ji, S., and Thurman, R.G. (1983). Cell surface changes and enzyme release during hypoxia and reoxygenation in the isolated, perfused rat liver. J. Cell Biol. *97*, 778–786.

Lommerse, P.H., Vastenhoud, K., Pirinen, N.J., Magee, A.I., Spaink, H.P., and Schmidt, T. (2006). Single-molecule diffusion reveals similar mobility for the Lck, H-ras, and K-ras membrane anchors. Biophys J *91*, 1090–1097.

Meder, D., Moreno, M.J., Verkade, P., Vaz, W.L.C., and Simons, K. (2006). Phase coexistence and connectivity in the apical membrane of polarized epithelial cells. Proc. Natl. Acad. Sci. U. S. A. *103*, 329–334.

Misra, A., Pandey, C., Sze, S.K., and Thanabalu, T. (2012). Hypoxia Activated EGFR Signaling Induces Epithelial to Mesenchymal Transition (EMT). PLOS ONE *7*, e49766.

Nikolaus, J., Scolari, S., Bayraktarov, E., Jungnick, N., Engel, S., Plazzo, A.P., Stockl, M., Volkmer, R., Veit, M., and Herrmann, A. (2010). Hemagglutinin of Influenza Virus Partitions into the Nonraft Domain of Model Membranes. Biophys. J. *99*, 489–498.

Pinaud, F., Michalet, X., Iyer, G., Margeat, E., Moore, H.P., and Weiss, S. (2009). Dynamic partitioning of a glycosyl-phosphatidylinositol-anchored protein in glycosphingolipid-rich microdomains imaged by single-quantum dot tracking. Traffic *10*, 691–712.

Pyenta, P.S., Holowka, D., and Baird, B. (2001). Cross-correlation analysis of inner-leaflet-anchored green fluorescent protein co-redistributed with IgE receptors and outer leaflet lipid raft components. Biophys J *80*, 2120–2132.

Pyenta, P.S., Schwille, P., Webb, W.W., Holowka, D., and Baird, B. (2003). Lateral diffusion of membrane lipid-anchored probes before and after aggregation of cell surface IgE-receptors. J. Phys. Chem. A *107*, 8310–8318.

Di Rienzo, C., Gratton, E., Beltram, F., and Cardarelli, F. (2013). Fast spatiotemporal correlation spectroscopy to determine protein lateral diffusion laws in live cell membranes. Proc. Natl. Acad. Sci. *110*, 12307–12312.

Saxton, M.J. (1995). Single-particle tracking: effects of corrals. Biophys J *69*, 389–398.

Sezgin, E., Levental, I., Grzybek, M., Schwarzmann, G., Mueller, V., Honigmann, A., Belov, V.N., Eggeling, C., Coskun, U., Simons, K., et al. (2012). Partitioning, diffusion, and ligand binding of raft lipid analogs in model and cellular plasma membranes. Biochim Biophys Acta *1818*, 1777–1784.

Shelby, S.A., Holowka, D., Baird, B., and Veatch, S.L. (2013). Distinct Stages of Stimulated FcεRI Receptor Clustering and Immobilization Are Identified through Superresolution Imaging. Biophys. J. *105*, 2343–2354.

Skaug, M.J., Faller, R., and Longo, M.L. (2011). Correlating anomalous diffusion with lipid bilayer membrane structure using single molecule tracking and atomic force microscopy. J. Chem. Phys. *134*.

Sunyer, R., Ritort, F., Farré, R., and Navajas, D. (2009). Thermal activation and ATP dependence of the cytoskeleton remodeling dynamics. Phys. Rev. E *79*.

Weber, S.C., Spakowitz, A.J., and Theriot, J.A. (2012). Nonthermal ATP-dependent fluctuations contribute to the in vivo motion of chromosomal loci. Proc Natl Acad Sci U A *109*, 7338–7343.

Wu, M., Huang, B., Graham, M., Raimondi, A., Heuser, J.E., Zhuang, X., and De Camilli, P. (2010). Coupling between clathrin-dependent endocytic budding and F-BAR-dependent tubulation in a cell-free system. Nat Cell Biol *12*, 902–908.

Zhao, J., Wu, J., and Veatch, S.L. (2013). Adhesion Stabilizes Robust Lipid Heterogeneity in Supercritical Membranes at Physiological Temperature. Biophys. J. *104*, 825–834.